Dissertation

submitted to

the Combined Faculties of the Natural Sciences and Mathematics

of the Ruperto-Carola-University of Heidelberg, Germany,

for the degree of Doctor of Natural Sciences

Put forward by

Franz Ludwig Rauch

born in Dachau, Germany

Oral examination on 28 June 2017

From

Final Dark Matter Results and

Background Shape Uncertainties in XENON100

to

First Light in XENON1T

Referees:

PD Dr. Teresa Marrodán Undagoitia

Prof. Dr. Tilman Plehn

Abstract

The quest to directly detect dark matter, in particular weakly interactive massive particles (WIMP), lead to a development of a plethora of detector technologies. Since 2007 dual-phase time-projection chambers exploiting liquid xenon performed superior to all other technologies at WIMP masses above a few GeV/c^2. Among them, the XENON100 experiment shows the longest measurement with a combined live time of 477 days. An analysis to probe spin independent and spin dependent WIMP interactions is presented in this thesis, setting an upper limit on the WIMP-nucleon spin independent cross section at 1.1×10^{-45} cm^2 for a 50 GeV/c^2 WIMP mass. Furthermore, potential improvements are identified in the conventional XENON100 analysis and the outlined solution allows to consider shape uncertainties of non-parametric probability density functions by means of a profile likelihood analysis. The applicability of the method is shown by constraining the WIMP model in an astrophysical independent approach with XENON100 data. Finally, performance tests of the Hamamatsu R11410-21 3" photomultiplier tubes (PMT) are presented which are employed in the next generation experiment XENON1T. First results from the commissioning of the XENON1T detector with respect to the PMT performance are shown with a special focus on the impact of light emitting tubes.

Zusammenfassung

Der Versuch Dunkle Materie, insbesondere schwach wechselwirkende, massive Teilchen (engl. WIMP) direkt nachzuweisen, resultierte in der Entwicklung einer Vielzahl von Detektortechnologien. Seit 2007 liefern Zwei-Phasen Zeitprojektionskammern, die flüssiges Xenon verwenden, überragende Ergebnisse für WIMP-Massen im Bereich einiger GeV/c^2 im Verlgeich zu anderen Technologien. Eines dieser Experimente ist XENON100, welches die längste Messdauer mit 477 Tagen vorweisen kann. Die Auswertung der Daten im Bezug auf spinunabhängige und spinabhängige Wirkungsquerschnitte ist in der vorliegenden Arbeit beschrieben und ergibt, dass ein spinunabhängiger WIMP-Nukleus Wirkungsquerschnitt bis zu 1.1×10^{-45} cm^2 für 50 GeV/c^2 WIMPs ausgeschlossen werden kann. Desweiteren werden mögliche Verbesserungen in der konventionellen XENON100 Methode der Datenanalyse identifiziert und eine mögliche Lösung umrissen, die es erlaubt nicht-parametrische Formunsicherheiten in einer Profile-Likelihood Analyse zu berücksichtigen. Die Anwendbarkeit der Methode wird anhand der Beschränkung der WIMP Theorie durch eine Auswertung der XENON100 Daten mit einem astrophysikalisch unabhängigen Ansatz gezeigt. Abschließend sind Ergebnisse der Leistungstests von den in dem Nachfolgeexperiment XENON1T verwendenten Hamamatsu R11410-21 3" Photoelektronenvervielfachern (engl. PMT) zusammengefasst. Zudem werden erste Ergbisse nach einer einjährigen Inbetriebnahme des Detektors, mit Fokus auf die PMT Leistungsfähigkeit sowie den Einfluss lichtemittierender Sensoren, vorgestellt.

Contents

List of Figures

List of Tables

Chapter 1

Introduction

The standard model of cosmology (ΛCDM) is able to describe numerous observations in the universe to a high precision. However, in its foundation, it is based on the existence of the cosmological constant (Λ) as well as cold dark matter (CDM), two less understood components of the universe adding up to approximately 95 % of the total energy content. While the nature of dark energy remains uncertain, various indications for dark matter already exist from its gravitational interaction with baryonic matter. A direct detection of this, possibly, new particle is to this date absent. In this introduction, the existence of a particle explaining the phenomenon of dark matter is motivated and possibilities for its direct detection are outlined. In section 1.1 dark matter indications by its gravitational interactions are summarized and possible dark matter candidates are presented in section 1.2. General dark matter detection strategies are given in section 1.3 and, in case of direct detection experiments, the expected event rates are derived in section 1.4. Aspects of the nuclear physics involved in the scattering process are explained in section 1.5, and are used to constrain dark matter models as shown in section 1.6. Statistical methods used to constrain dark matter models, in particular the profile likelihood method, are explained in section 1.7 and, finally, the current status of dark matter experiments is summarized in section 1.8. A more detailed discussion can be found in a review of dark matter direct detection experiments [1], which was co-written by the author of this thesis. The content and structure of this chapter follows this review.

1.1 Dark matter indications

Cosmological observations indicate unambiguously a yet unknown source of gravitational potential (dark matter) which contributes to approximately a quarter of the energy density of the Universe according to the standard model of cosmology [2]. One of the best described measurements in cosmology and strongest indications for dark matter is a fit of temperature anisotropies in the cosmic microwave background (CMB) measured by e.g. WMAP [3] and Planck [4] satellites. The ΛCDM model correctly describes temperature anisotropies created by oscillations of the baryon-photon fluid and dark matter. From a fit of these baryonic acoustic oscillations the dark matter component of the universe is estimated to account for 26.8 % [5] of the energy content of the

universe.

Furthermore, it is generally assumed that dark matter is non-relativistic and has a small free streaming length [2]. To this class of dark matter candidates it is referred to as cold dark matter (CDM). In this case, CDM serves also as a seed for the formation of baryonic matter distributions (e.g. galaxies) as shown in N-body simulations of dark matter particles [6][7][8]. These simulations result in a characteristic cosmic web with structures as small as $\mathcal{O}(10\,\mathrm{kp})$ which simultaneously match measurements of galaxy surveys [9][10][11]. However, at small scales 'dark-matter-only' simulations fail to accurately predict the small number of observed dwarf galaxies in the local group [12]. Recently, a baryonic component has been added to the simulations, indicating a significant influence on the dark matter distribution which could reconcile the the so-called *missing satellite problem* [13].

On small scales, the gravitational interaction of dark matter is observed by gravitational lensing [14] [15]. In analogy to optical lenses, light is deflected by massive objects, resulting in various typologies such as object deformations, multiple images and in rare cases, Einstein rings [16]. The required gravitational potential can be reconstructed from these observations, proving that luminous matter alone does not account for the enclosed mass potential. It turns out that weak lensing is a unique probe of dark matter to map its density distribution within galaxy clusters. For instance, by observing the relics of galaxy-cluster collisions, the reconstructed gravitational centers of dark matter are clearly displaced from the center of luminous matter as shown in [17][18][19] and in an extensive study of 72 cluster collisions [20]. The displacement of the gravitational centers is explained by collisions of baryonic matter and a very small or non-existent self-interaction cross-section of dark matter [21].

Historically, the first indications for non-luminous matter, *dark matter*, was observed in astronomy in order to explain the dynamics of nebulae in the Coma cluster [22]. By assuming a viralised cluster, the measured velocities were unexpectedly high which were explained by a non-visible dark matter component. The existence of dark matter within galaxies was later observed due to approximately constant rotation velocities of stars at larger radii [23], contradicting the Newtonian prediction of $v \propto 1/\sqrt{r}$. A uniformly-distributed halo of dark matter exceeding the extend of luminous matter explains both, the high velocities in clusters and rotation curves in galaxies (e.g. [24]).

1.2 Particle dark matter

The previously mentioned observations of the gravitational potential of dark matter might be explained by a new particle, but other theories exist trying to explain the missing mass. The theory of modified Newtonian dynamics (MOND [25]) or its relativistic extension TeVeS [26] try to alter Newtons law. These models successfully describe individual observations of the dark matter phenomenon, e.g. the rotation curves, but fail to explain the universe to the level of the ΛCDM model [27][28]. If dark matter consists of particles, the standard model of particle physics must be extended, since none of the known particles show the necessary requirements. To account for all

present observation, the particle must be neutral, stable on time scales of the age of the universe, its free streaming length must be small, it should account for the estimated gravitational potentials and should at most feature weak or no self-interactions

From the standard model of particles, the neutrino would be, in general, a good dark matter candidate if its free streaming length would be lower [29] and its mass larger [30]. Sterile neutrinos are motivated to explain the small neutrino mass [31] and are able to account for dark matter if their masses are in the range from 1 keV to tens of keV [32].

Axions or axion-like particles (ALP) are particles initially proposed to solve the strong CP-problem [33] and are also, in part of their parameter space, dark matter candidates. While the original axion models are ruled out [34] or strongly constrained by experiments [33], a yet unconstrained parameter space of ALPs is able to account for the correct dark matter abundance [35]. In addition, they feature the correct free streaming length for structure formation if produced via e.g. the vacuum realignment mechanism [36][37].

Other models predict the existence of dark matter particles such as Superwimps, Light Gravitinos or Hidden Dark Matter [38]. Among the large number of theories trying to predict a new particle accounting for dark matter, the most prominent features a weakly interacting and massive particle (WIMP). It naturally accounts for the present dark matter abundance if it features weak interactions and masses ranging from a couple GeV/c^2 to several TeV/c^2. The WIMP is produced thermally [39], in analogy to the standard model particles. More details and dark matter candidates are summarized in [1][38].

1.3 Detection principles

Three main strategies are exploited to search for dark matter: a production at particle accelerators, indirectly trying to detect signals from annihilation or decay products, or a direct detection of interactions with standard model particles. A sketch illustrating possible dark matter interactions with standard model particles is shown in figure 1.1.

A production of dark matter particles with a particle accelerator (upward direction in figure 1.1) might be achieved by e.g. proton-proton collisions at the LHC [40] [41]. The produced dark matter particle itself would not be observable but the missing transverse momentum within the event reconstruction would indicate such a particle. To this date, no evidence of a dark matter production at the LHC has been reported [42][43].

Self annihilation of dark matter or a decay could produce standard model particles (downward direction in figure 1.1) which might be observable as a measurable flux of cosmic particles (γ-rays, e^+, e^-, p^+, p^-,...) [44]. Of special interest for an indirect detection of dark matter are astronomical objects where the dark matter fraction is exceptional high [45], for example, present in the galactic center or in dwarf spheroidal galaxies. Several measurements of a particle flux above expectation have been observed in the past [46][47][48][49], but none of them can be attributed to dark matter without dispute. A further detection method, which essentially probes a dark matter scattering

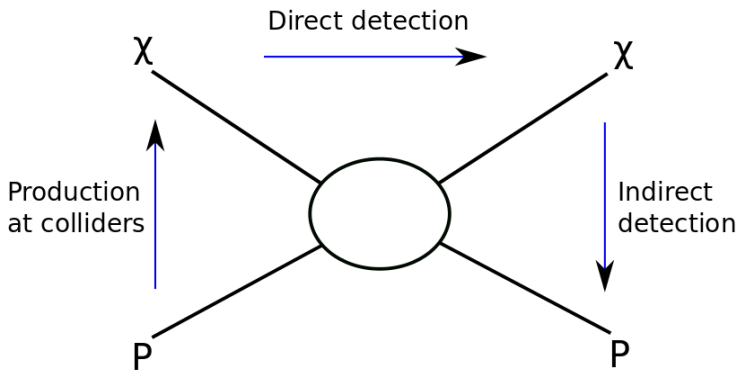

Figure 1.1: Illustration of possible dark matter interactions with standard model particles. Figure published in [1].

process with standard model particles, is possible by a detection of neutrinos originating from the Sun. Due to the gravitational capture of dark matter particles inside the Sun, the dark matter density, and accordingly the self-annihilation rate, is locally enhanced. If neutrinos are emitted in this process, it might be possible to detect dark matter annihilation with neutrino telescopes [50].

An unambiguous evidence for a new particle would arise from a detection of a dark matter particle directly scattering off a target nucleus (left to right in figure 1.1). A number of experiments exploiting different target materials and technologies trying to detect dark matter are explained in detail in [1]. The principles of direct detection and expected recoil rates are summarized below.

1.4 Expected recoil rates for direct detection

For direct detection experiments it is essential to know the expected dark matter scattering rate with the target nuclei, the recoil energy spectrum and direction of the dark matter particles. In the model of WIMP dark matter, it is expected that the Earth moves through a halo of dark matter with a mass of m_χ and a local density ρ_0. In first order, the dark matter halo is homogeneously distributed with a number density $n_\chi = \frac{\rho_0}{m_\chi}$. Given the observed density distribution, it can be shown that the kinematics of dark matter particles follow the same velocity distribution $f(v)$ as a self-gravitating isothermal gas sphere which is described by a Maxwell-Boltzmann distribution. It follows, that the maximal velocity of a dark matter particle does not exceed the escape velocity v_{esc} of the Milky Way as those particles would not be gravitational bound. Finally, a non zero cross-section σ is assumed for interactions between dark matter particles and the target nucleus m_A. The expected event rate $\frac{dN}{dt}$ for dark matter particles scattering off the target nuclei N_T is then given by the product of the cross-section

and WIMP particle flux integrated over the velocity distribution,

$$\frac{\mathrm{d}N}{\mathrm{d}t} = \int \mathrm{d}v \left(\sigma \cdot N_T \cdot n_\chi \cdot v \cdot f(\mathbf{v}, \mathbf{t})\right). \tag{1.1}$$

This theoretical interaction rate is adapted if applied to direct detection experiments as detectors are, in general, able to measure the recoil energies. Hence, it is suitable to write the event rate $\frac{1}{M_T}\frac{dN}{dt} =: R$ with respect to the energy deposition E caused by dark matter scattering off the target nucleus E_{nr} [51]

$$\frac{1}{M_T}\frac{\mathrm{d}^2 N}{\mathrm{d}t\mathrm{d}E_{nr}} = \frac{\mathrm{d}R}{\mathrm{d}E_{nr}}(E_{nr}, t) = \frac{1}{M_T}\frac{\mathrm{d}}{\mathrm{d}E_{nr}}\int \mathrm{d}v \left(\sigma(E_{nr}) \cdot N_T \cdot n_\chi \cdot v \cdot f(\mathbf{v}, \mathbf{t})\right). \tag{1.2}$$

It is common to normalize equation 1.2 to the detector target mass $M_T = N_T \cdot m_A$ with the target atom mass m_A to define the rate in units of $\mathrm{kg}^{-1}\mathrm{day}^{-1}\mathrm{keV}^{-1}$. The energy threshold E_{thr} of the detector is explicitly introduced by the lower integral boundary and the rate equation $\frac{dR}{dE}$ becomes [52]

$$\frac{\mathrm{d}R}{\mathrm{d}E_{nr}}(E_{nr}, t) = \frac{\rho_0}{m_\chi \cdot m_A} \cdot \int_{v_{min}}^{v_{esc}} v \cdot f(\mathbf{v}, t) \cdot \frac{d\sigma}{dE_{nr}}(E_{nr}, v)\ \mathrm{d}v, \tag{1.3}$$

with the minimal dark matter velocity v_{min} detectable by the experiment defined as,

$$v_{min} = \sqrt{\frac{m_A E_{thr}}{2\mu_A^2}}. \tag{1.4}$$

The parameter μ defines the reduced mass of the WIMP-nucleus system. Finally, equation 1.3 contains the two parameters of interest m_χ and σ for direct detection experiments. All other parameters are either given by astrophysics or can be measured by dedicated experiments. The explicit time dependence of the velocity distribution is caused by the revolution of the Earth around the Sun. Based on equation 1.3 three different signatures of dark matter interactions can be derived and are exploited by numerous experiments [1].

The time dependence of equation 1.3 comes, in first order, from an annual modulation of the event rate caused by changes of the dark matter velocity in summer and winter relative to the detector rest frame. Given a fixed energy threshold, and a maximum relative velocity on June 2nd, the measured dark matter event rate is larger in June than in December [53]. Following [54], the annual modulation of the event rate is given by ($E \equiv E_{nr}$)

$$\frac{dR}{dE}(E, t) \approx S_0(E) + S_m(E) \cdot \cos\left(\frac{2\pi(t - t_0)}{T}\right), \tag{1.5}$$

with an expected phase of $t_0 = 150\,\mathrm{d}$, a period of $T = 1\,\mathrm{yr}$ and the time-averaged event rate S_0. The amplitude of the modulation is given by S_m.

Other experiments try to exploit the characteristic directionality of nuclear recoils resulting from WIMP interactions [55]. The angular dependence, as defined by the

angle,γ, between the direction of the nuclear recoil and the mean direction of the solar motion, is explicitly shown if equation 1.3 is rewritten in terms of γ,

$$\frac{dR}{dE\ d\cos\gamma} \propto \exp\left[\frac{-[(v_E + v_\odot)\cos\gamma - v_{min}]^2}{v_c^2}\right]. \tag{1.6}$$

Here v_E denotes the Earth's motion, $v_\odot$ the Sun's velocity around the galactic center and the halo circular velocity $v_c = \sqrt{3/2}v_\odot$. As a result, experiments can expect that the integrated event rate in forward direction will exceed the rate of backwards scattered events by an order of magnitude [55].

Most experiments use the signature of the energy spectrum of dark matter interactions. Following [52], equation 1.3 can be approximated by

$$\frac{dR}{dE}(E) \approx \left(\frac{dR}{dE}\right)_0 F^2(E) \exp\left(-\frac{E}{E_c}\right), \tag{1.7}$$

with the event rate $\left(\frac{dR}{dE}\right)_0$ at zero momentum transfer and a constant E_c expressing the detector specific energy scale for nuclear recoils [52]. The form factor $F^2(E)$ corrects for the assumption of point-like interactions in the cross-section and is discussed in section 1.5. The spectral shape of the expected WIMP spectrum is governed by the exponential function and, hence, the event rate is strongly rising for small energy depositions as seen in the left panel of figure 1.2. Furthermore, heavier target nuclei (e.g. tungsten, xenon) show an enhanced rate at lower recoil energies than lighter elements (argon, sodium). In addition, the right panel shows event rates for a light WIMP of 25 GeV/c^2 (dashed line) as well as for a 100 GeV/c^2 WIMP (solid line) scattering off argon (blue) and tungsten (green).

1.5 Cross-sections and nuclear-physics corrections

The derivation of equation 1.3 starts from astrophysical assumptions and summarizes all astrophysical aspects in the differential event rate $\frac{d\sigma}{dE}$. However, to constrain the dark matter mass and its cross-section further assumptions on the specific particle model and nuclear-physics processes are necessary.

It is common to separate the different assumptions of the microscopic processes by expressing the differential cross-section as the sum of the spin-dependent (SD) and spin-independent (SI) interactions

$$\frac{d\sigma}{dE} = \frac{m_A}{2\mu_p^2 v^2} \cdot (\sigma_p^{\mathrm{SI}} \cdot F_{\mathrm{SI}}^2(E) + \sigma_0^{\mathrm{SD}} \cdot F_{\mathrm{SD}}^2(E)). \tag{1.8}$$

Here the differential cross-section is written in terms of the cross-section at zero momentum transfer σ_0 and the form factor F such as: $\sigma \propto \sigma_0 \cdot F^2$. The form factor accounts for the coherence loss when the momentum transfer is high and the wavelength of the particle is no longer large compared to the nuclear radius. This effect impacts the event rate as illustrated in the right panel of figure 1.2. Calculated event rates when neglecting the form factor result in the dotted lines by assuming scattering

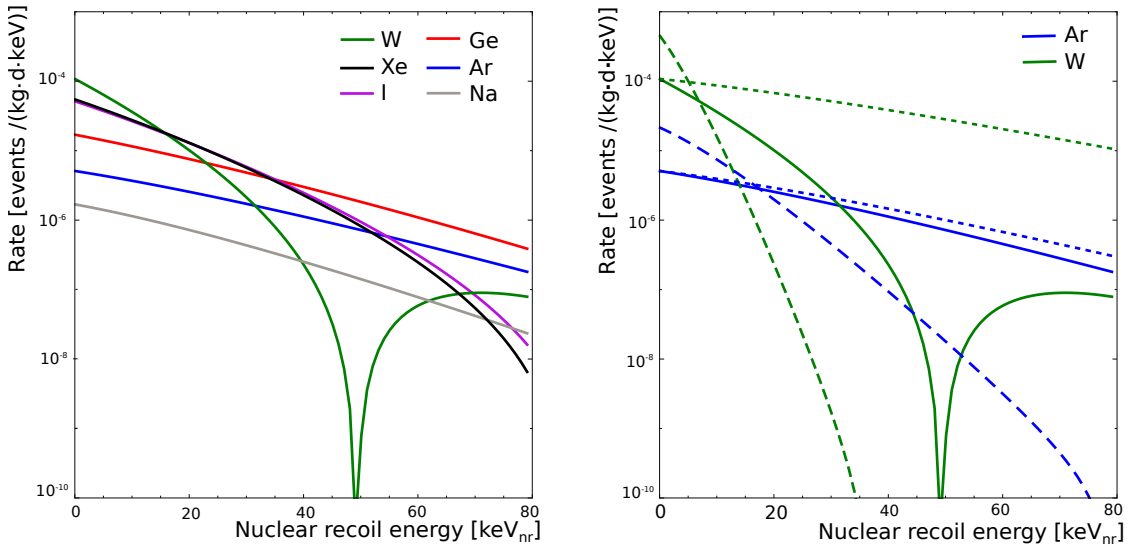

Figure 1.2: (Left) The colored lines indicate expected differential event rates for dark matter experiments, assuming a $100\,\mathrm{GeV}/c^2$ WIMP and a cross-section of $10^{-45}\,\mathrm{cm}^2$. The different colors represent tungsten (green), xenon (black), iodine (magenta), germanium (red), argon (blue) and sodium (gray) as target materials. (Right) The figure shows changes of event rates by lowering the WIMP mass to $25\,\mathrm{GeV}/c^2$ (dashed line) and neglecting the form factor (dotted line). The solid lines are equal to the ones in the left panel. The rates are computed for the light argon (heavy tungsten) nucleus and shown in blue (green). Figures published in [1].

off argon (blue) and tungsten (green) nuclei. It is also visible that the form factor shows a stronger impact at lower recoil energies for heavy than for light target elements.

The SI component can be written in terms of individual dark matter coupling constants of protons f_p and neutrons f_n

$$\sigma_0^{\mathrm{SI}} = \sigma_p \cdot \frac{\mu_A^2}{\mu_p^2} \cdot [Z \cdot f_p + (A - Z) \cdot f_n]^2, \tag{1.9}$$

with the proton-WIMP reduced mass μ_p, the mass number A and the atomic number Z. Generally, only isospin conserving interactions ($f_n = f_p = 1$) are considered simplifying the SI cross-section to,

$$\sigma_0^{\mathrm{SI}} = \sigma_p \cdot \frac{\mu_A^2}{\mu_p^2} A^2. \tag{1.10}$$

The form factor F_{SI} is calculated by assuming that the distribution of scattering centers is similar to the charge distribution measured by electron scattering experiments [52]. A common parameterisation used in direct detection experiments is derived by Helm [56]. A recent reanalysis using shell-model calculations [57] verified these calculations. Of special importance is the scaling $\sigma_0^{\mathrm{SI}} \sim A^2$, which results in a strong enhancement of the recoil rates for heavier targets as shown in figure 1.2.

The SD cross-section can be written in terms of a spin structure function based on a chiral effective field theory considering two body currents [58][59],

$$\sigma_0^{SD} = \frac{32}{\pi}\mu_A^2 \cdot G_F^2[a_p\langle S^p\rangle + a_n\langle S^n\rangle]^2 \cdot \frac{J+1}{J}. \tag{1.11}$$

where G_F^2 is the Fermi coupling constant, J the total nuclear spin and a_p (a_n) the effective proton (neutron) couplings to WIMPs. The expectation value of the effective nuclear spin content of protons and neutrons is expressed by $\langle S^{p,n}\rangle$.

1.6 Displaying results of a direct detection experiment

The result of a dark matter experiment is generally expressed in terms of the dark matter mass m_χ and the cross-section σ_0 as introduced in equation 1.3. Without loss of generality, a spin-independent and isospin-conserving interactions are assumed by combining equations 1.3, 1.8 and 1.10 to,

$$\frac{dR}{dE}(E,t) = \frac{\rho_0}{2\mu_A^2 \cdot m_\chi} \cdot \sigma_0 \cdot A^2 \cdot F^2 \int_{v_{min}}^{v_{esc}} \frac{f(\mathbf{v},t)}{v}\, \mathrm{d}v, \tag{1.12}$$

The left plot in figure 1.3 illustrates a generic reference limit (open black curve) in terms of the dark matter cross section and the dark matter mass. The colored lines describe qualitatively changes to the reference curve by varying important detector parameters. At low WIMP masses and due to the exponential shape of the WIMP spectrum given by equation 1.7, most energy depositions are of the same order as the energy threshold of the detector. Consequently, the sensitivity of the experiment is strongly reduced at low WIMP masses. This is attributed to a steeper decrease of the event rate of light WIMP masses at higher recoil energies as shown in the right panel of figure 1.2 by a $25\,\mathrm{GeV}/c^2$ (dashed line) and $100\,\mathrm{GeV}/c^2$ WIMP (solid line). Accordingly, the sensitivity is strongly improved by lowering the energy threshold (blue line in figure 1.3). The minimum of the limit is governed by the kinematics of the scattering process, in particular, the mass differences between the WIMP and target element (red line). At higher WIMP masses, not only the event rate is suppressed by $1/m_\chi$, but the coherence loss of the scattering process at high momentum transfers also weakens the limit due to lower expected event rates (see figure 1.2). The overall sensitivity can be improved by an increase of the exposure defined as the product of the duration of the experiment and target mass, as long as the background of the experiment is sufficiently low (green line). Due to the degeneracy of m_χ and σ in equation 1.3 a signal would be displayed as a rotated contour line (closed black line).

In the right panel of figure 1.3, the sensitivity to the cross-section as a function of the exposure is shown (black line). Again, an increase of exposure enhances the sensitivity. A larger target mass strongly enhances the sensitivity, in particular for small exposures (blue line). However, if the background is large, the sensitivity does not further improve with increasing exposures (red line). To improve the sensitivity

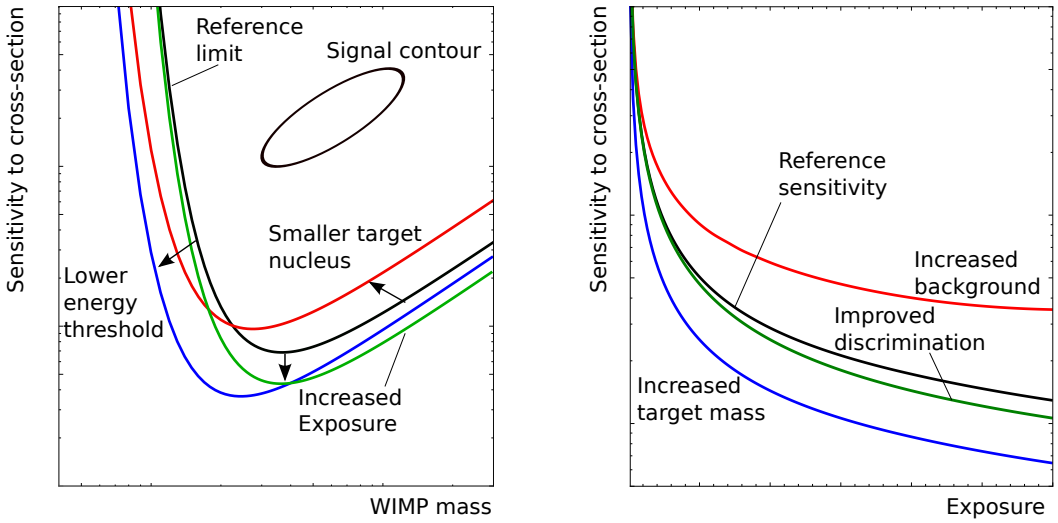

Figure 1.3: (Left) The black line shows a generic result of a direct detection experiment displayed as a function of the dark matter mass and cross-section. The various colored line indicate the effect of changing either the energy threshold (blue), exposure (green) or target element (red). (Right) The plot shows the evolution of the sensitivity as a function of the exposure achieved by longer measurement times. A reference evolution is shown in black while the impact of a larger target mass (blue), improved discrimination (green) or increased background (red) is also illustrated. For more information see text. Figures published in [1].

of the detector for long exposures, dedicated background rejection techniques, e.g. enhanced discrimination (green line), become equally important.

A comparison of limits or detected signals between various dark matter experiments is essential to reduce systematic uncertainties in individual results. However, by interpreting experimental data in terms of the cross-section and dark matter mass, it is necessary to assume various astrophysical parameters. In particular, the relative velocity of the dark matter particle in the rest frame of the detector is essential, as it governs the deposited energy in the detector. This velocity dependence impedes the comparison among experiments, especially at velocities producing recoil energies close to the energy threshold. In strong cases, two experiments are not comparable as they probe different dark-matter velocity intervals [60]. A solution to this problem is proposed in [61][62], which suggests to calculate results in an alternative parameter space which is independent of astrophysical assumptions and, therefore, common to all target elements. A parameter η, which comprises all astrophysical assumptions and the halo integral of equation 1.12, can be defined as

$$\eta = \frac{\rho_0 \cdot \sigma_p}{m_\chi} \cdot \int_{v_{min}} \frac{f(\mathbf{v}, t)}{v} \mathrm{d}v. \tag{1.13}$$

By exploiting the monotonicity of the velocity integral [61], η can be approximated

to be independent of the detector response (see section 4.5). If equation 1.12 is evaluated in terms of η and the minimum speed v_{min}, η becomes a common parameter to all targets, regardless of the detector technology. An example for possible results expressed in the v_{min} parameter space is shown in figure 1.4. The red line indicates

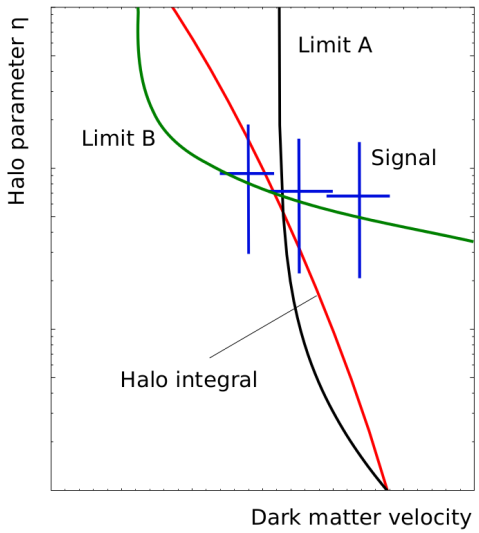

Figure 1.4: The figure illustrates an astrophysical independent parameter space to reduce systematic uncertainties in the comparison of results from dark matter experiments. The parameter η is common to all experiments if the recoil energies are mapped to the minimal velocity (see text). A signal is indicated by the blue markers and limits are illustrated by the black and green lines. The red line displays values of η for a fixed set of halo parameters. Figure is published in [1].

the allowed parameter space for η, assuming common parameters of the dark matter halo. If two experiments would show results as illustrated by the green and black line, the detectors would essentially probe incompatible velocity intervals of η, and a comparison of results depends on the assumed astrophysical dark matter halo model. Furthermore, a detection of dark matter (blue markers) can only be excluded or confirmed by other experiments in compatible velocity intervals. Published results of dark matter experiments in this parameter space are shown for instance in [63][64][65][66] and as an example for XENON100 science run II data in section 4.5.

1.7 Statistical analysis of data

The main difficulty of a dark matter data analysis, which is prevalent to all direct detection experiments, stems from the low number of expected signal events and the presence of background. Commonly, three different statistical methods are used to either derive upper limits on the WIMP-nucleus cross-section or state the significance of a dark matter signal. A method without the need of strong assumptions on either

the signal or the background distribution is developed by Feldman and Cousins [67], which reflects a Poisson counting experiment in presence of background. However it fails to include uncertainties in the background prediction nor is it possible to consider information about the shape of distributions [68].

A second commonly used method is the so-called maximum gap method derived by Yellin [69] which utilizes the signal model shape but is independent of a background model. By assuming that all events are attributed to the signal, this method derives conservative limits on the cross-section but is not able, by construction, to derive a signal, if present.

If the information of both, the signal and background model is available, the maximum likelihood or profile likelihood (PL) method derives the strongest results as it exploits the full knowledge of both distributions. However, results calculated by this method might be less robust if model uncertainties are not considered appropriately. A more detailed description of methods can be found in [1][68] and references therein.

In the following, the PL method is explained as it is especially well suited to search for new physics phenomena given the reasons above [70]. It is assumed that the signal, f_s, and background, f_b, probability density functions (pdf) are given as a function of the measured quantity x. Without loss of generality, x is assumed to be one-dimensional. The pdfs are parameterized by the variables θ_k and θ_l $(k, l \in \mathcal{N})$ for the signal and background model, respectively. The extended likelihood function is then given by

$$\mathcal{L} = \text{Poiss}(N|N_s + N_b) \prod_{i=1}^{N} \frac{N_s f_s(x_i, \theta_k) + N_b f_b(x_i, \theta_l)}{N_s + N_b} \prod_{k,l} \mathcal{L}(\theta_{k,l}). \tag{1.14}$$

The first term describes the Poisson nature of the counting experiment of N observed events where N_s are attributed to the signal and N_b to the background. The second term considers the shape of the two pdfs evaluated at N measured positions x_i, whereas the third term constrains the uncertainties of the parameters θ_k and θ_l. This likelihood function is used to estimate N_s and, hence, the dark matter cross-section σ from a given data sample by maximizing the likelihood. If only N_s is of interest, the other parameters N_b, θ_k and θ_l can be treated as nuisance parameters and $\mathcal{L}$ can be profiled in N_s [70].

Furthermore the level of agreement of a dataset with respect to a tested hypothesis can be quantified by the test statistic q_μ defined by [70]

$$q_\mu = -2\log\left(\frac{\mathcal{L}(N_s, \hat{\hat{\theta}}_n)}{\mathcal{L}(\hat{N}_s, \hat{\theta}_n)}\right), \tag{1.15}$$

where $\mathcal{L}$ is given by equation 1.14. The $n = 1, 2, ...$ conditional maximum likelihood estimators (MLE) are expressed by $\hat{\hat{\theta}}_n$ which maximize $\mathcal{L}$ given a fixed value of N_s. In case of the example given in equation 1.14, the n conditional MLEs are N_b, θ_k and θ_l. The parameters $\hat{N}_s$ and $\hat{\theta}_n$ are the MLEs of $\mathcal{L}$. By computing $q_{N_s,obs}$ of a dataset for a specific N_s, the level of disagreement between the tested N_s and the data is given by the p-value (or equivalently the significance Z),

$$p_{N_s} = \int_{q_{N_s,obs}}^{\infty} f(q_{N_s}|N_s) dq_{N_s}, \qquad Z = \Phi^{-1}(1 - p_{N_s}). \tag{1.16}$$

Here $f(q_{N_s}|N_s)$ describes the distribution of the test statistic q_{N_s} given the tested N_s. The quantile of the standard Gaussian is denoted by Φ^{-1}. Of special importance is a theorem derived by Wilks [71] stating that, if $\hat{N}_s$ is normal distributed around its true value, then, in general, the distribution $f(q_{N_s}|N_s)$ asymptotically approaches a χ^2 distribution with one degree of freedom.

The test statistic q_0 for a discovery is computed by the background only ($N_s = 0$) hypothesis which is defined, following [70], as

$$q_0 = \begin{cases} -2\log\left(\frac{\mathcal{L}(0,\hat{\hat{\theta}})}{\mathcal{L}(\hat{N}_s,\hat{\theta})}\right), & \hat{N}_s \geq 0 \\ 0, & \hat{N}_s < 0. \end{cases} \tag{1.17}$$

In this case the distribution $f(q_0|0)$ asymptotically approaches a half-χ^2 distribution and a delta function around zero [70]. In contrary, by computing a one-sided confidence interval, or limit, the signal hypothesis N_s is rejected (see equation 1.18) and for cases where $\hat{N}_s > N_s$, q_{N_s} is set to zero [70]

$$q_{N_s} = \begin{cases} -2\log\left(\frac{\mathcal{L}(N_s,\hat{\hat{\theta}})}{\mathcal{L}(\hat{N}_s,\hat{\theta})}\right), & \hat{N}_s \leq N_s \\ 0, & \hat{N}_s > N_s. \end{cases} \tag{1.18}$$

1.8 Current status of dark matter searches

In the past decade, direct detection experiments improved their sensitivity at a tremendous speed and results for spin-independent and dependent interactions are shown in figures 3.12 and 3.13, respectively. A yet unsolved tension still remains due to an annual modulation of the event rate for over 14 annual cycles measured by the DAMA/Libra collaboration [72]. By fitting the expected period and phase as defined in section 1.4, the signal corresponds to a $9.3\,\sigma$ detection of dark matter (red contour line). Other experiments, which are several orders of magnitude more sensitive, published exclusion limits on the cross-section, the currently most constraining being published by the LUX collaboration [73] at high WIMP masses (right panel of figure 3.12). At low WIMP masses (left panel of figure 3.12), LUX is most constraining for WIMP masses above $4\,\mathrm{GeV/c^2}$ [73], and at very low WIMP masses experiments with an exceptional low energy threshold such as CDMSlite [74] and CRESST [75] show best results. These results are, among others, in direct contradiction to the DAMA/Libra result. The experimental data can also be interpreted in the context of spin-dependent interactions, individually computed for neutron coupling and proton coupling as shown in the left and right of figure 3.13. For neutron coupling, the most sensitive results are published by the PandaX collaboration [76]. For couplings to protons, the PICO collaboration shows the most sensitive results, despite the smaller exposure, by exploiting a target containing fluorine [77] which features the strongest coupling strength to protons of the used target elements. Details of liquid xenon detectors will be given in chapter 2, other technologies are summarized in [1].

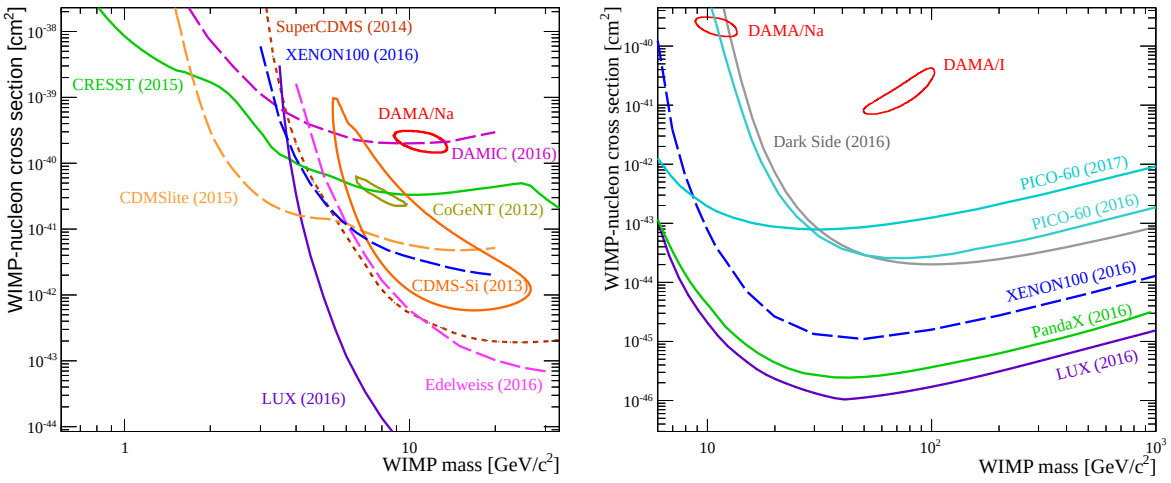

Figure 1.5: Limits on the spin-independent cross-section for subset of experimental limits (90 % CL) and detection claims (2σ) for WIMP masses below 12 GeV/c^2 (left) and above (right). Figures and references are published in [1].

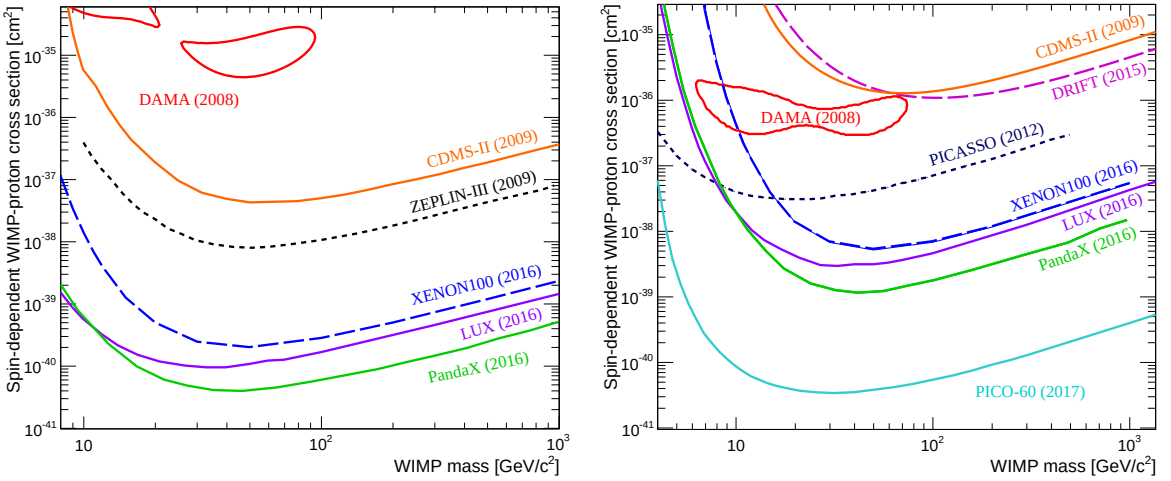

Figure 1.6: In the left (right) plot limits are shown on the spin-dependent proton (neutron) cross-section for subset of experimental limits (90 % CL) and detection claims (2σ). Figures and references are published in [1].

Chapter 2

XENON detectors

In the quest to directly detect dark matter, a plethora of different detector technologies are in use. Among the best performing are liquid noble gas time projection chambers (TPCs), due to their large target masses and efficient background suppression. In this chapter, the working principle of a TPC is introduced in section 2.1 and the mechanisms leading to the signal generation are discussed in section 2.2. Details of liquid xenon TPCs, in particular the XENON detectors, are summarized in section 2.3.

2.1 Dual phase time projection chamber

The general detector concept is sketched in figure 2.1 and aims to simultaneously detect scintillation and ionization signals induced by particle interactions with the nuclei of the target. The primary signal (S1) is generated by scintillation of the target nuclei itself, using liquid noble gases such as argon or xenon. In addition, interacting particles can either ionize the target medium directly (e.g. β-radiation) or by a recoil of the nucleus and subsequent xenon-xenon collisions. An applied electric field (drift field) between the cathode and grounded gate grid drifts created electrons from the interaction point to the liquid gas interface. An extraction field generated by the anode, extracts the electrons out of the liquid xenon. A gaseous layer at the top of the liquid is used for secondary scintillation (S2) by an acceleration of the extracted electrons towards the anode. Finally, the S2 signal is produced by photons created due to proportional scintillation [78]. More information about the microscopic processes is given in section 2.2. Both processes, direct scintillation (S1) and proportional scintillation (S2) in the gas phase, generate photons which are detected by two photomultiplier tube (PMT) arrays at the top and bottom of the TPC. The walls of the TPC are covered by highly reflective Teflon panels to increase the overall photon detection probability.

The time delay between the S1 and S2 allows to compute the interaction depth and defines the vertical position (Z) of the vertex as indicated in the right of figure 2.1. Through the hit pattern in the top PMT array, the horizontal position (XY-coordinates) of the vertex is reconstructed. Therefore, a TPC enables a full three dimensional vertex resolution. This allows to define an inner fiducial volume with reduced background from natural radioactivity contained in surrounding materials. With this method, xenon is not only used as a WIMP target but its high stopping power is

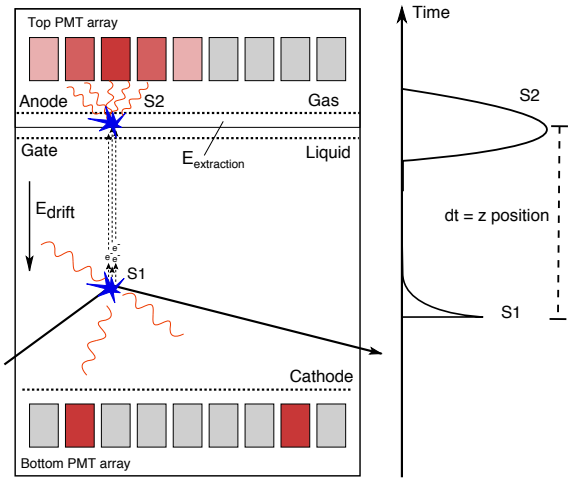

Figure 2.1: The illustration shows the detector concept of a dual-phase time projection chamber. The scintillation signal (S1) is created at the interaction vertex, whereas the amplified charge signal (S2) is produced in the gaseous phase on the top of the liquid xenon, and delayed by the drift time of the electrons. For more information see text. Figure published in [1].

also exploited to suppress external radiation.

The external background of liquid xenon detectors originates in parts from environmental gamma-ray radiation due to decays in the natural ^{238}U and ^{232}Th chains as well as from isotopes such as ^{40}K, ^{60}Co and ^{137}Cs contained in surrounding materials. These background sources can be reduced by a careful material selection and an appropriate shield of the fiducial volume with lead, copper and polyethylene or large water tanks. The second external source stems from cosmogenic and radiogenic neutron radiation. The former can be reduced by operating the experiment in deep underground locations, the latter is reduced by similar methods to reduce environmental gamma-ray radiations. The main intrinsic background of xenon TPCs consists, in general, of anthropogenic ^{85}Kr and radon emanation (mainly ^{222}Rn) from detector materials. More information can be found in [1].

Finally, it is expected that WIMP interactions deposit energies of several keV in the medium, which typically involve two observed signals in the PMTs, generated by the S1 and S2 signal. At these recoil energies, the first S1 peak features a small size, quantified in units of measured photoelectrons (PE) ranging from (1-100) PE and a short peak width of several ns. The due to the electron drift delayed and amplified S2 peak features sizes of several hundreds to thousands of PEs, a peak width at the order of μs and is typically used to trigger an so-called event (see vertical axis in figure 2.1). The length of an event is at the order of the drift time of electrons from the bottom to the top of the TPC. For each event several parameters are computed such as the XYZ-position of the vertex, number of additional S1 and S2 peaks and light distribution among the PMTs which are later used in the analysis of the data.

2.2 Particle interactions in xenon

Dual phase TPCs exploit the scintillation and ionization properties of liquid noble gases which allow to detect interactions of particles with the medium. Commonly argon and xenon are in use which show, in general, a similar behavior. In this section, however, a summary of the microscopic processes of the signal generation and energy scales is given for xenon.

2.2.1 Signal generation

The interactions of particles in the liquid xenon (LXe) target with typical energies of the order of a few keV result in scintillation (emission of a photon), an ionization of the medium, and in heat/phonons. In case of interactions in liquid noble gases, scintillation is observable due to the production and subsequent decay of excited xenon dimers (excimers) which are formed by the recoiling xenon nuclei. In particular, the wavelength of the emitted vacuum ultraviolet (VUV) photons, created by the dissociation of excimers, is centered at 178 nm [79]. At this wavelength, liquid xenon is transparent and the scintillation signal (S1) can be directly observed by photomultiplier tubes optimized for a VUV wavelength (see chapter 5). The de-excitation is on timescales from a few to tens of ns [80]. In addition to the formed excitons, the xenon atom can also be ionized by either ionizing radiation or by xenon-xenon collisions. In both cases free electrons are created. Part of the electrons will recombine with the surrounding ions, producing recombination photons which additionally contribute to the S1 signals. However, part of the electrons can be extracted from the locally ionized medium by an applied electric field and drifted to the liquid-gas interface. Due to a strong extraction field, the electrons can be moved through the liquid surface potential and their signal is amplified by collisions with the gaseous xenon. Electroluminescence processes [78] of the electron showers produce a second amplified scintillation signal (S2). A remaining part of the initially deposited energy is converted into heat which can not be observed with the explained detector design.

Of particular importance is the fraction of recombining electrons in the locally ionized medium. The recombination probability not only depends on the density and total number of created ions, but also on the track length of the recoils [81][82][83]. The parameters which govern the microscopic processes depend on the recoil energy and on the recoiling particle (neutron, electron). In particular, it depends on the interacting particle scattering off either the xenon nucleus (nuclear recoil or NR) or the xenon electron-shell (electronic recoil or ER). As a result, the ratio of recombination and charge extraction is different for ER and NR interactions. This difference can be exploited by using the ratio of S1 over S2 signal sizes to discriminate between NR and ER interactions (see also section 2.3). As an example figure 2.2 shows the discrimination parameter defined by the logarithm of the ratio of the peak sizes of S2 over S1 as a function of S1 for ER (blue markers) and NR (red markers) calibration data in XENON100. In case of ER calibration ^{232}Th and ^{60}Co sources are used, and for NR data an AmBe neutron source is placed inside the XENON100 shield [84]. The separation of the two distributions illustrates the discrimination power of a dual phase

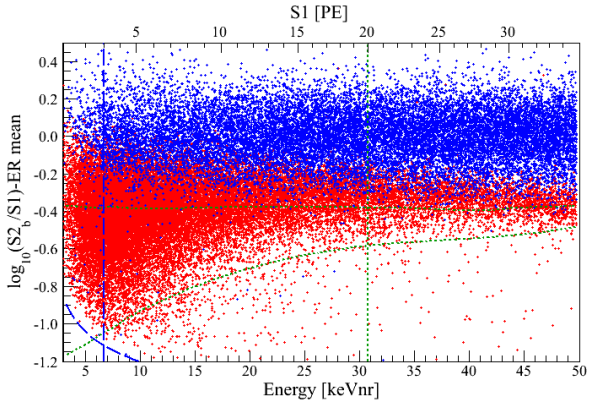

Figure 2.2: Illustration of the discrimination power of a LXe TPC. Here a nuclear (blue) and electronic recoil (red) calibration source from XENON100 is shown. The separation of the two populations is visible. Figure from the XENON100 collaboration.

TPC which allows to define the signal region of interest (ROI). As an example, in XENON100 the ROI (see figure 2.2) is given by the 99.75 % ER rejection line (upper horizontal green dashed line) and the $3\,\sigma$ contour of the NR data (lower green dashed line). The energy thresholds are illustrated by the > 3 PE S1 condition (left vertical blue dashed line) and > 150 PE S2 requirement (lower blue dashed lines). The maximal considered energies for the WIMP search correspond to 30 PE in cS1 (vertical green dashed line) [85]. More information on the XENON100 WIMP analysis is given in chapter 3.

2.2.2 Signal corrections

Both observed signals, S1s and S2s, are, in general, proportional to the deposited energy. Therefore, a dual phase TPC can be used as a calorimeter if all losses of the signal quanta during the measurement process are accounted for. In case of the S1 signal, the probability that a primary scintillation photon hits the photocathode of a PMT depends on the position of the interaction. This light collection efficiency (LCE) can be determined by sampling the detector volume with a monoenergetic and homogeneously distributed calibration source [84]. The correction of observed S1 signal is denoted by cS1.

In addition, various corrections to the S2 signals are applied to account for electron and photon losses within the TPC. First of all, the loss of electrons during the drift from the interaction site to the liquid surface is caused by electronegative impurities in the LXe and is quantified by an electron lifetime. Furthermore, the electron lifetime is under normal detector conditions continuously increased due to a permanent cleaning of the LXe, and, hence, time dependent. A second correction, depending on the XY-position, is applied to correct for varying probabilities to detect secondary scintillation photons. Close to the wall the signal detection efficiency is reduced mainly due to a smaller light collection efficiency at large radii, resulting in a systematic reduction of the observed S2 signal size. The corrections are defined by requiring a homogeneous

S2 response to monoenergetic calibration sources [86]. Again the corrected S2 signal is denoted by cS2. A more detailed description can be found in [84].

2.2.3 Energy scales

Typically, the cS1 and cS2 signals are quantified by the number of created photoelectrons (PE) measured by the PMTs. After corrections, these two signals provide information on the deposited energy of interacting particles. For the detection of WIMPs, the energy scale for nuclear recoils is of relevance and is introduced below.

The cS1 signal can be translated to the corresponding nuclear recoil energy E_{nr} by [87]

$$E_{nr} = \frac{\text{cS1}}{L_y} \frac{1}{\mathcal{L}_{eff}(E_{nr})} \frac{S_{ee}}{S_{nr}}, \tag{2.1}$$

where $\mathcal{L}_{eff}$ is the LXe relative scintillation efficiency to 122 keV γ-interactions at zero drift field. Several external (colored markers) measurements of $\mathcal{L}_{eff}$ as a function of the recoil energy are shown in the left panel of figure 2.3. In addition, various parameterisations of the functional form are indicated by lines which are derived by matching Monte Carlo generated data to measurements. The parameters $S_{ee} = 0.58$ and $S_{nr} = 0.95$ describe the scintillation quenching due to the electric field [88]. The functional form of $\mathcal{L}_{eff}$ including the parameterisation of uncertainties stems from direct and external measurements [89]. The detector-dependent light yield at 122 keV$_{ee}$ (keV electron-equivalent energy) is denoted by L_y. A measurement to even lower recoil energies of $\mathcal{L}_{eff}$ can be found in [90].

Following the notation of [91] the energy scale for the S2 signal is given by

$$E_{nr} = \frac{\text{cS2}}{Y} \frac{1}{Q_y(E_{nr})}, \tag{2.2}$$

where Y quantifies the secondary amplification, generally determined by the detector response to individual amplified electrons, also called single electron signals [92]. The parameterisation of $Q_y(E_{nr})$ is taken from [91] (see right panel of figure 2.3). The

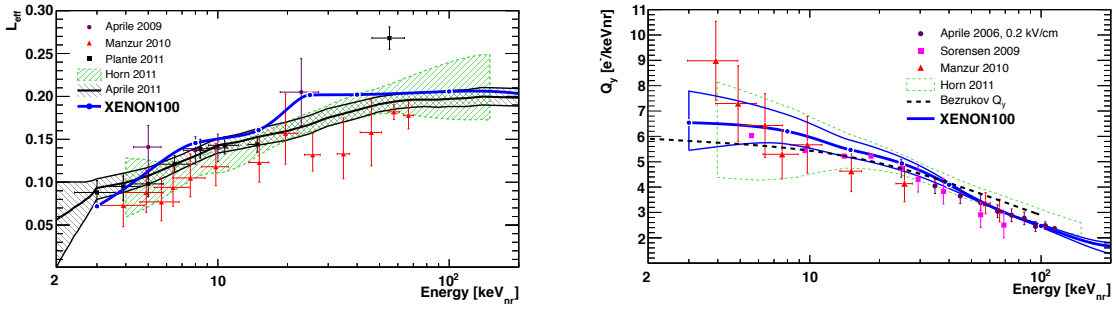

Figure 2.3: (Left) Energy scale for the scintillation signal (S1). (Right) Energy scale of the charge signal (S2). Figures from [91] and references therein.

functional form is determined by a few external measurements as well as an absolute Monte Carlo match to AmBe calibration data of XENON100 [91].

2.3 The XENON detectors

The design of a detector aims to optimize several parameters in order to increase the sensitivity to dark matter interactions. First of all, the size of the target and the measurement duration increases the overall sensitivity to dark matter interactions. Secondly, a lower energy threshold enhances the sensitivity, especially to detect recoils of low WIMP masses. Finally, a low background increases the signal significance. In light of those parameters, the XENON detectors are summarized in detail below. The most sensitive LXe dual phase TPCs since 2010 as well as a projection up to 2022 are shown in section 2.4.

2.3.1 XENON100

The XENON100 detector is installed at the Laboratori Nazionali del Gran Sasso (LNGS) of INFN in Italy at an average depth of 3600 m water equivalent. This results in a muon flux reduction factor of $\sim 10^6$ with respect to sea level [93][94]. Careful material selection [95] and detector design [84] minimizes the total electronic recoil (ER) background of XENON100.

The detector consists of a cylindrical TPC with a height of 30.5 cm and a radius of 15.3 cm. The LXe target mass of XENON100 is 62 kg, surrounded by an optically separated, active veto with an additional amount of 99 kg of LXe. In total 178 R8520-AL 1 inch PMTs are operated in the top and bottom array as well as 62 tubes in the active veto to reduce external backgrounds. The detector is contained in a cylindrical, low-radioactivity, stainless steel vessel and is shielded from environmental and residual cosmogenic radiation by successive layers of oxygen free high conductivity copper, polyethylene, lead, and water/polyethylene. The inner walls of the TPC are covered with highly reflective PTFE panels to increase the light collection efficiency. To further reduce the background from ambient radon contained in air, the inner part of the shield is continuously flushed with boil-off nitrogen. The cooling of LXe is provided by a pulse tube refrigerator operated outside the shield that allows a constant operating temperature of $\sim$182 K inside the TPC over time scales of more than one year. In order to minimize the probability for ionization electrons to be captured by electronegative impurities along their path towards the anode, the xenon must be kept on a continuous purification cycle.

The XENON100 detector achieves an ultra low ER background rate of $(5.3 \pm 0.6) \times 10^{-3}$ events/(keV$_{ee}$ $\times$ day $\times$ kg) in the inner 34 kg of the active target [96]. The background during the XENON100 science run II consists in parts of natural radioactivity from materials (38 %) and intrinsic background sources originating from ^{85}Kr (55 %) and ^{222}Rn (7 %). The subdominant neutron background ($\sim$10 %) stems from cosmogenic induced neutrons (70 %) and radiogenic sources (30 %) [97]. Details of the background model in XENON100 are given in section 3.4. The lowest achieved energy

threshold of XENON100 is 6.6 keV$_{nr}$ [85].

2.3.2 XENON1T and XENONnT

The general detector design of XENON1T is similar to the one of XENON100 and is also operated at LNGS. The cylindrical TPC shows an increased height of 96.7 cm and a radius of 96.0 cm. The stainless steel cryostat contains, in total, a mass of 3200 kg LXe, with an active target of 2000 kg. The top and bottom PMT arrays are equipped with 248 Hamamatsu R11410-21 3 inch PMTs. A detailed description of the PMT arrays can be found in section 5. Similarly to XENON100, the walls are covered by Teflon to increase the light yield. The drift and extraction fields are as in XENON100 generated by a cathode, gate grid and anode. In addition, screening meshes are mounted in front of the PMT arrays and are operated at the same HV potential to reduce the field in front of the arrays.

The cryostat is placed inside a water tank of 10 m in height to further shield it from external neutrons and γ-rays [98]. In addition, the water tank is instrumented with 84 Hamamatsu R5912ASSY 8 inch PMTs and operated as an active muon-Cherenkov veto [99]. Hence, muons and muon-induced background can be tagged and their contribution to the background is negligible [98]. It is expected that the ER background of XENON1T will be $(1.8 \pm 0.15) \times 10^{-4}$ events/(keV$_{ee}$·day ·kg) for a 1 ton fiducial volume [98]. The larger xenon mass reduces the contribution of natural radioactivity from materials down to a total contribution of 5 %. The main ER background stems from ^{222}Rn with a relative contribution of 85 % [98]. The contribution of the NR background is 22 %. All improvements result in a sensitivity of 1.6×10^{-47} cm^2 at 50 GeV/c^2 [98].

The XENON1T cryostat and infrastructure is designed to host up to $\sim$ 7 t of LXe. An upgrade of the TPC enables, with a moderate effort, a second phase of the experiment, XENONnT [98]. The number of PMTs will increase from 248 to $\sim$450 of the same model as used for XENON1T and still functioning PMTs could be reused. New technologies have to be employed to decrease the main background caused by ^{222}Rn. It is shown in [100][101] that a ^{222}Rn contamination can be reduced by a continuous xenon distillation. Hence, with a reduction factor of 10 in radon and an increase of the target volume a sensitivity of 1.6×10^{-48} cm^2 at 50 GeV/c^2 is predicted [98].

2.4 Sensitivity evolution

To conclude this introduction to the LXe TPC technology, the sensitivity evolution to spin independent interactions of various present (XENON100, LUX, PandaX, XENON1T) and future experiments (XENONnT, LZ) is shown in figure 2.4. For the following sensitivity estimations a reference WIMP mass of 50 GeV/c^2 is chosen. Among all direct detection detectors, dual phase LXe TPCs outperform other technologies in a WIMP mass range of 8 GeV/c^2 to several TeV since 2010 [1].

The sensitivities are calculated with the method developed by Feldman and Cousins [67]. It is assumed that on average in two calendar days, one live day of dark matter data is recorded. Details of the three XENON100 results, based on science runs taken between

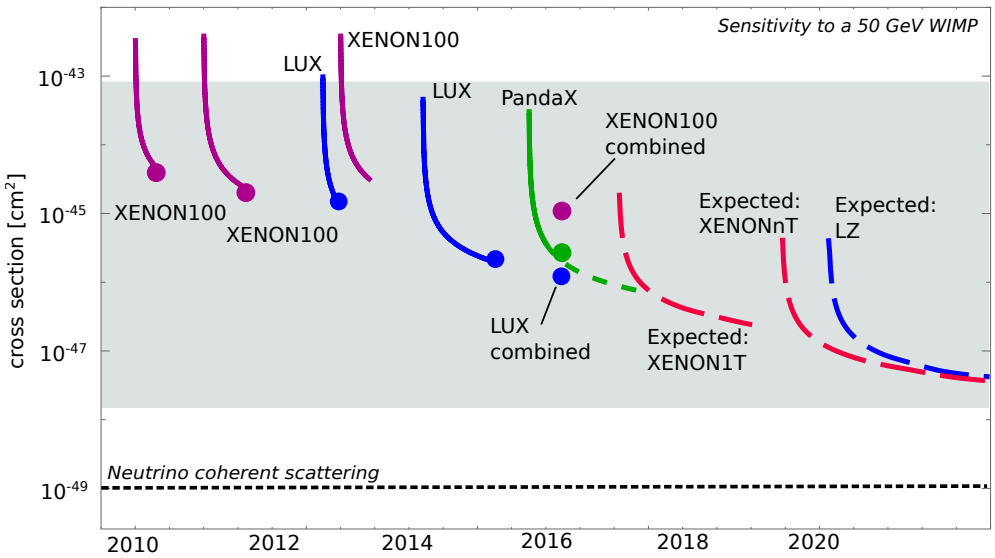

Figure 2.4: Sensitivity evolution of present (XENON100, LUX, PandaX) and future (XENON1T, XENONnT, LZ) LXe TPCs assuming a 50 GeV/c^2 WIMP mass, indicated by solid and dashed lines, respectively. Solid round markers indicate published results [105, 85, 102, 73, 106, 104]. The gray shaded area represents approximately the naturalness of a 50 GeV neutralino in the minimal super-symmetric standard model (MSSM) [107].

2010 and 2014, are presented in chapter 3.

The LUX experiment surpassed the XENON100 results in 2013 with a total of 85 live days and a 118 kg fiducial volume [102]. A combined analysis in 2016 with a final exposure of 3.35×10^4 kg·day and a reduction of the energy threshold to 1.1 keV$_{nr}$ results in the current strongest limit of 1.1×10^{-46} cm^2 at 50 GeV/c^2 [73]. This result is achieved with an ER background of 3.6×10^{-3} events/(keV·kg·day) [103].

A third collaboration operates the PandaX-II LXe TPC in the Jin-Ping underground laboratory in China. Its fiducial volume contains ~300 kg of LXe and the total exposure acquired so far is 3.3×10^4 kg·day [104], a similar exposure as obtained by the combined LUX result. At 50 GeV/c^2, the calculated limit on the WIMP cross-section is 2.5×10^{-46} cm^2 for an energy threshold of 4.6 keV$_{nr}$. The ER background rate, dominated by ^{85}Kr, is 1.95×10^{-3} events/(keV·kg·day) [104]. In contrary to the LUX experiment, PandaX is at the time of writing still operational and even further improvements to the sensitivity are expected.

For the next generation experiment XENON1T, a background rate of 0.6 events per year is assumed based on a Monte Carlo simulation [98]. For XENONnT [98] and LZ [108] only 1.8 events in 1000 days inside a 5.6 t Xe fiducial volume are expected, assuming new methods to reduce intrinsic background sources and a negligible contribution of external sources. Figure 2.4 illustrates the increase of sensitivity to dark matter interactions from LXe TPCs up to ~2022. The gray shaded area indicates the favored parameter space of the neutralino [107] based on a specific super-symmetric standard model. More details to current and future detectors can be found in [1].

Chapter 3

XENON100 final dark matter results

The XENON100 experiment was, between 2010 and 2013, for WIMP masses above a few GeV/c^2, the most sensitive dark matter detector in the world. Three major science runs led to publications which constrained a significant parameter space of the WIMP model. In this section, a combined dataset of a total of 477 live days and featuring a total exposure of 1.75×10^4 kg$\cdot$ day is used to calculate exclusion limits on the spin-independent and spin-dependent WIMP interactions. At the beginning of this chapter the properties of each science dataset are introduced (section 3.1) and the dark matter event selection is outlined in section 3.2. The derivation of the dark matter signal model is explained in section 3.3 and the construction of the background model in section 3.4, which are used to perform a profile likelihood analysis (section 3.5). The chapter concludes with the science results in section 3.6 and a discussion about further improvements of the analysis (section 3.7). The content and outline of this chapter follows the publication [106] where the author of this thesis has contributed significantly to the analysis and is a corresponding author.

3.1 Science data

In this chapter, the three XENON100 science runs are combined which were acquired between the years 2010 and 2014. Maintaining stable detector parameters for 5 years of operation is demanding but essential to be able to combine the data. During these 1446 days of operation, 477 days of dark matter data was acquired while 392 days were dedicated to the calibration of the detector.

The first science run I contains 100.9 live days of dark matter data and results are published in [89]. Similarly, science run II is individually published [85] comprising 225 live days. A third science run of 153 live days is only published in combination with a reanalysis of the first two datasets [106]. Both, the combined reanalysis as well as the new science run III are discussed in this chapter. Each run contains data with small differences in detector settings and background levels which must be considered individually to reduce systematic uncertainties. During a run itself, however, these

		Run I	Run II	Run III
Science Campaign	Live days [d]	100.9	223.1	153.0
	Period	2010	2011-2012	2013-2014
Detector condition	Average electron lifetime [μs]	290 ± 40	520 ± 60	720 ±110
	L_y [PE/keV]	2.20 ± 0.09	2.28 ± 0.04	2.25 ± 0.03
	S2 amplification [PE/e$^-$]	19 ± 7	20 ± 7	17 ± 7
	Extraction field in gas [kV/cm]	11.89 ± 0.02	10.30 ± 0.01	11.50 ± 0.02
	Average liquid level [mm]	7.49 ± 0.01	6.47 ± 0.01	7.39 ± 0.01
	Drift field [V/cm]	533	533	500
Calibration	^{60}Co, ^{232}Th ER events in S1 range	4116	15337	10469
	^{241}AmBe NR events in S1 range	55423	25315	92226
Analysis	Low S1 threshold [PE]	3	3	3
	High cS1 threshold [PE]	30	30	30
	Low S2 threshold [PE]	300	150	150
	Fiducial mass [kg]	48	34	34
	Total Selected Events	929	402	346
	Expected background in benchmark ROI	3.9 ± 0.5	1.7 ± 0.3	1.0 ± 0.2
	Candidate events in benchmark ROI	3	1	1

Table 3.1: Detector and analysis parameters estimated for each run.

parameters are required to be constant. All relevant corrections on measured quantities in each run need to be accounted for in the analysis and are explained below and summarized in table 3.1.

The applied corrections (see section 2.2.2) to the S1 and S2 signals (see section 2.2), differ between the runs due to various small changes of detector parameters. The measured S2 signal size of each interaction is corrected for the corresponding electron lifetime as a function of the drift length (see section 2.2.2). The average lifetime during the first science run is $(294 \pm 37)\,\mu$s, and increases in run II and III to $(519 \pm 64)\,\mu$s and $(720 \pm 110)\,\mu$s, respectively, explained by an improved xenon purity due to a continuous cleaning of the xenon gas over the years. The optical properties of the TPC did not degrade during the four years of operation, as only 5 PMTs were removed from the analysis between run I and run III (see L_y values in table 3.1). Hence, the S1 corrections are common in all runs but are applied in higher spatial resolution, due to an improved analysis, in run II and III than for run I. The PMT-gain values used to determine the signal size in terms of photoelectrons (PE) are calibrated on a weekly basis. Average gain values for each PMT are used in the analysis which are stable within a few percent on time scales of several months. Significant changes of the average gain value are accounted for, if necessary, multiple times in a run.

The energy scales in units of keV are derived from the corrected S1 and S2 values but depend on parameters which differ between the three runs. In case of the scintillation signal, the light yield L_y at 122 keV$_{ee}$, as introduced in equation 2.1, did not change significantly among the runs, again due to the stable optical properties of the TPC during the detector operation. The S2 amplification Y (see equation 2.2), depends on the lengths of the gas gap as measured by the liquid level as well as on the strength of the extraction field in the gas [92]. Changes of the extraction field at the order of a few $\pm$100 V/cm (see table 3.1) are mainly caused by a varying liquid level of maximal 1 mm (see table 3.1) and results in different values for Y. During a run the S2 amplification

can be assumed to be constant [92] and, hence, are accounted for by a single number for each run (see table 3.1).

A major difference between the three science runs is caused by a larger ^{85}Kr concentration in run I. Due to a dedicated Kr distillation campaign of the xenon inventory, the initial ^{85}Kr concentration in run I of (360 ± 70) ppt [89] is reduced to $(19 \pm 4\,\text{ppt})$ [85] in run II and $(6 \pm 1\,\text{ppt})$ in run III. The ^{85}Kr concentration is measured, ex-situ, from the detector extracted gaseous xenon (GXe) samples which are analyzed by an ultra-sensitive rare gas mass spectrometer [109]. A second method uses an in-situ analysis technique tagging events by delayed coincidence signature of ^{85}Kr decays [110]. The analysis confirms the external measurements and indicates that the background in run I is dominated by internal ^{85}Kr. In run II and III, however, the concentration is significantly reduced and remaining radioactivity in surrounding material contributes most (see section 3.4).

The response of the detector is calibrated for both NR and ER interactions (see section 2.2). The former is characterized by an ^{241}AmBe (α, n) source, the latter by ^{137}Cs, ^{60}Co, ^{232}Th sources [84]. To calibrate the background of the detector, events from low energy Compton scattering by high-energy γ sources, ^{60}Co and ^{232}Th are used. The ^{137}Cs data is only used to estimate the electron lifetime and not for the background calibration of the experiment. This avoids correlated uncertainties between the S2 correction and background model. With NR data the signal acceptance of the event selection can be estimated. The total number of events in the signal energy range are listed in table 3.1 and shows an increase of calibration data to reduce the statistical uncertainty of the background model and acceptance calculation in run II and III in comparison to run I.

3.2 Data selection

Details of the analysis and event selection are published for run I and II [111] and separately for each run in [85][89]. Only minor changes are applied in this reanalysis compared to the published data selection procedure in run I and II. The event selection for run III is adapted from the procedure which was developed for run II. In this section, the general XENON100 data selection is briefly summarized and only changes to the previous method are explained in detail. These selection criteria are defined on calibration data alone, to ensure an unbiased optimization of the cut parameters. During the analysis the signal region of the science data is blinded. It is clearly stated if further requirements are applied to the data after unblinding the signal region.

3.2.1 General event selection

The analysis of the data, aiming to search for WIMP interactions, focuses on the identification of energy depositions from particles scattering off the target nuclei inside a fiducial volume. Various data selection requirements (cuts) are applied targeting to remove background events such as noise or non-WIMP event signatures.

First of all, basic data quality conditions are applied to remove electronic noise

which is sometimes identified by the data processor as a valid signal. These events can be, for example, reduced by requiring a large signal-to-noise ratio within a waveform or a characteristic peak width of the S1. In addition an at least two-fold coincidence of the PMTs for a valid S1 is required within a time window of 20 ns, including a general threshold of 0.35 PE per PMT. A requirement of the S2 width avoids events caused by interactions with the gas.

WIMP interactions, if existent, are very rare and, hence, the probability of observing multiple interactions of the same particle can be neglected. To select single scatter events, criteria on the number of S1 and S2 signals within a waveform are applied. For the number of S1 peaks a simple requirement for one S1-peak is sufficient whereas for S2, a threshold conditions of the second largest S2 peak as a function of the largest S2 is necessary due to the common presence of amplified *single electrons* inside the TPC creating a large number of small S2s in a waveform [92].

A large amount of background events can be removed by exploiting the information about the interaction position. By using liquid xenon with its high density the majority of particles emitted by the natural radioactivity in the materials are stopped after a few mm of propagation in LXe. The spatial vertex reconstruction of the TPC allows to define an inner volume (fiducial volume) featuring a reduced background. Furthermore, the fiducial volume can be optimized with respect to the dominant background source. In case of the large intrinsic ^{85}Kr concentration during run I, fiducialisation does not remove the main source of background and a larger fiducial volume of 48 kg is more beneficial due to the increased exposure. In run II and III, however, external sources dominate the background (see section 2.3.1) and these events are significantly reduced by selecting the inner 34 kg. In addition, background events can be reduced if those events in the fiducial volume are rejected which show a coincident signal in the surrounding veto (see section 2.3.1).

Finally, threshold conditions on the integral size of the S1 and S2 signals are used to ensure the optimal performance of the detector, data processor and trigger. For small energy depositions the amplified proportional scintillation signal triggers an event. In order to maintain 100 % trigger efficiency, an S2 threshold of 300 PE in run I and a lower threshold of 150 PE in run II and III is applied due to a optimization of the hardware trigger [111]. This condition is defined on the observed S2, prior to electron lifetime and position dependent corrections to the signal (see section 2.2.2). The S1 threshold in run I is in this combined analysis lowered from 4 PE [89] to 3 PE, now common to all three runs. In addition, the minimal size of the scintillation signal is also applied prior to the light collection dependent signal corrections (see section 2.2.2), instead to the corrected signals (cS1) as in [85][89]. This modification ensures that the lowest measured signals have a constant number of detected scintillation photons, independent of the varying light collection efficiency of the TPC. A threshold condition applied after signal corrections would ensure a minimal energy deposition. As a result of this change, the energy threshold expressed in units of $\mathrm{keV_{nr}}$ changes within the fiducial volume as shown in the left of figure 3.1 by the color coded scale. Black markers show the event positions as a function of the radius, R, and depth, Z, for run III data inside the fiducial volume (red line). Energy depositions of only 3 $\mathrm{keV_{nr}}$ can be measured in vicinity of the bottom PMT array due to the higher light collection efficiency. For reference, a lower

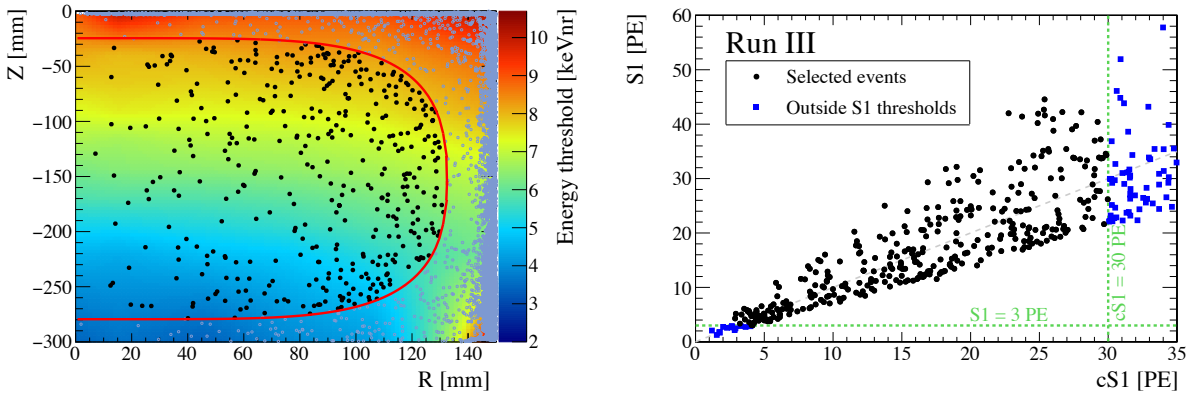

Figure 3.1: (Left) Illustration of detected events in run III (black markers) in den fiducial volume (red line) with respect to the radius R and depth Z of the TPC. The color coded scale displays the energy threshold in keV_{nr} corresponding to the requirement S1> 3 PE. (Right) Run III events (markers) which are inside the S1 range (black dots) and excluded by the S1 threshold conditions (blue squares). The horizontal line (green dashed) displays the lower S1 = 3 PE condition, whereas the vertical line the upper threshold at 30 PE applied to after signal corrections (cS1). Figures published in [106].

energy threshold of 6.6 keV_{nr} was used in the former publication of science run II [89]. In contrary, events at the top of the TPC must deposit at least 8.5 keV_{nr} to exceed the S1 threshold. Reflections of photons at the LXe-GXe surface causes a reduced light collection efficiency. The upper S1 threshold at 30 PE is applied on the corrected signal since the signal strength above 40 keV_{nr} is strongly reduced (see section 3.3). The right plot in figure 3.1 indicates events measured in run III which are rejected (blue squares) and selected (black) by the upper and lower S1/cS1 requirements.

3.2.2 Novel cuts

In this combined analysis two novel cuts are applied to all runs, improving the data selection. The two cuts are defined non-blind to run I and II but were developed and optimized on the blinded run III. The first new cut is enabled by using the new data processor [112] of the XENON1T experiment [98]. An improved S1 and S2 classification algorithm improves, in particular, the identification of single electron S2 peaks [92] as shown in the left of figure 3.2. The XENON100 data processor identifies the peak as a S1 between the red dashed lines as it neglects several small signals arriving after the first peak. As a consequence, the width of the reconstructed peak is artificially reduced and identified as a S1, despite the clear origin from single electrons which show typically a size of 20 PE and a width of 1 μs [92]. This misidentified S1 can be paired with a random S2 and mimic a nuclear recoil interaction in the region of interest. The XENON1T data processor, however, identifies correctly single electrons as an S2 which allows to reject these events from the analysis. The cut is applied post-unblinded to run II and

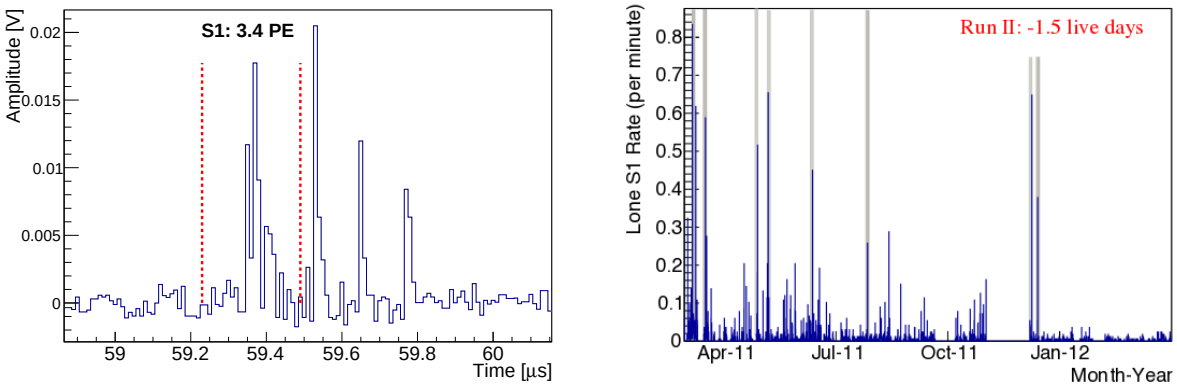

Figure 3.2: (Left) Illustration of a single electron S2 which is misidentified by the peak finding algorithm as an S1 indicated by the red dashed lines. The new XENON1T data processor is used to efficiently find these misidentified S1 peaks. (Right) Rate of lone S1 peaks found in waveforms during run II. Periods with a significant increase are marked in gray and removed from the analysis.

blinded to run III. A reduction of the non-Gaussian background (see section 3.4) by $\sim 60\%$ is achieved in run II while the signal acceptance of $> 98\%$ remains high.

The second novel cut aims to remove time intervals of the science data when an exceptional large amount of lone S1 peaks are present in the recorded waveforms. These lone S1 events are randomly measured without any correlated S2 and originate, therefore, not from physical interactions in the target. The origin of these peaks is unknown but could stem from sudden changing noise conditions. A large lone S1 rate increases the probability of accidental coincidences as the lone S1 can be paired with a random S2, increasing the background of the experiment. The cut is optimized post-unblinding on a lone S1 sample of the dark matter data during run II. Time intervals are removed where 3 or more lone S1s are present in a 500 s window as indicated by gray bands in the right of figure 3.2. The cut is applied post-unblinding to all runs and removes 0 d, 1.5 d and 0.6 d in run I, II and III, respectively. As a result, one of the two events in the region of interest in run II is removed with respect to the analysis of [85]. The final dark matter event selection for the reanalysis of run I, II as well as for the recently unblinded run III (black dots) is shown in figure 3.3 including events which are removed by the S1 threshold (blue squares). The data is analyzed in terms of the total measured S1 size and by the observed S2 light in the bottom PMT array only ($cS2_b$) which features smaller and better estimated size corrections than the top array [84]. Events which are removed by the novel cuts are indicated by green stars. In addition, events inside the ROI (defined in section 2.2) are shown by red crosses. Information about the total number of selected events individually listed for ER and NR calibration data as well as for the science run is shown in table 3.1.

Prior to unblinding the signal region in run III, side bands in S1 intervals of (2-3) PE and (30-100) PE were unblinded to confirm the background prediction based on the scaled number of ER calibration events and expected NR events (see section 3.4).

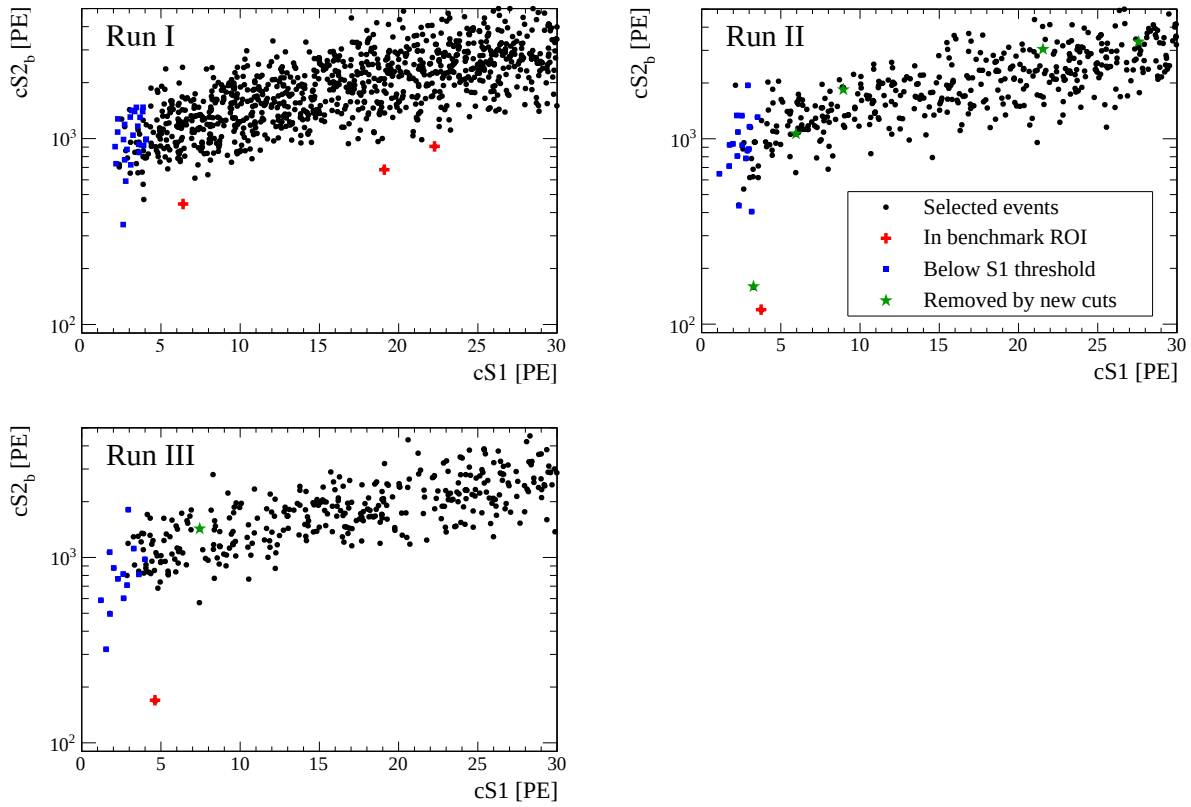

Figure 3.3: Science data after all applied cuts (black dots) and rejected by the S1 threshold condition (blue squares) with respect to cS1 and cS2$_b$: top left run I, top right run II and and bottom left, run III. Events in the ROI are indicated by red crosses. Rejected events by novel cuts are indicated by green stars. Figures published in [106].

No significant deviations were observed and the result by unblinding the signal region resulted in 1 event with an expectation of 1.0±0.2. The striking prediction confirms the data selection and applicability of the calibration data for the background estimation.

3.2.3 Signal acceptance

The signal acceptance for the event selection introduced above is estimated by the same technique as in [111] and is summarized below. By defining a control sample from calibration data, the acceptance of a cut is calculated by applying all cuts to the data but the one under study. For most cuts NR calibration data is used. Only for the acceptance of the S1 coincidence requirement and electronic noise cuts ER data is used. In contrast to a single dedicated NR calibration campaign per run, ER calibration is taken weekly throughout the science run II and III and represent, therefore, a better control sample for a possible time variation of e.g. noise. In case of run I, ER calibration data only before the science campaign is available.

In previous analyses, the cut acceptances were calculated as a function of cS1 [111]. In this combined analysis, the cut acceptance is now evaluated as a function of the

primary observable used in the cut. This reduces, in general, the uncertainty of the cut acceptance as it was found that, for example, the acceptance of the S1 coincidence requirement as a function of cS1 varies up to 15 % depending on the applied signal corrections. Hence, the cut acceptance estimation is more robust if it is evaluated in its natural parameter space in terms of cS1, S1, cS2 and S2.

A further modification in this analysis accounts for a limitation of the data processor to correctly identify the main S1 peak in a waveform. The data processor pairs the largest S2 with an S1, which features the highest coincidence level among the PMTs. However, due to correlated noise, the coincidence level might be biased and the processor selects the wrong primary S1, causing a rejection of the event from the control sample and resulting in an underestimation of the acceptance. This acceptance loss is calculated by the probability that a good S2 is accompanied by a signal induced by noise which is misidentified as the primary S1 due to the artificially enhanced coincidence level. The computed acceptance as a function of S1, combined with the S1 coincidence cut acceptance is shown in the top right plot of figure 3.4. All cut accep-

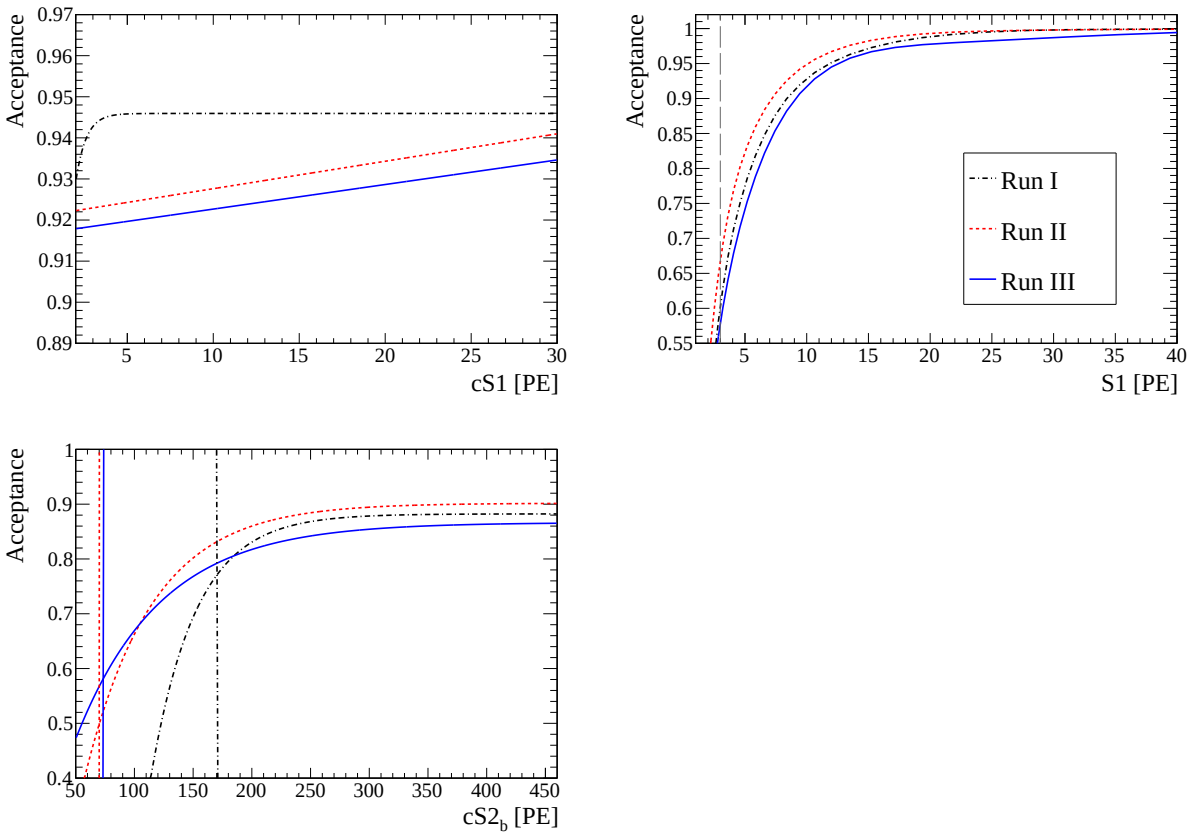

Figure 3.4: Combined cut acceptances for each run evaluated in their natural parameter space as function of cS1 (top left), S1 (top right) and cS2$_b$ (bottom left). Vertical lines indicate the energy thresholds of the detector. The cS2$_b$ cut acceptance remains constant above 450 PE. Figures from [106].

tances are re-evaluated for run I and II as well as in the same manner derived for run III. The cumulative acceptances for each run in terms of cS1, S1 and $cS2_b$ are shown in figure 3.4 in the top left, top right and bottom left panel, respectively. Differences in the acceptances among runs originate from varying detector parameters and cut optimizations. In particular, differences between run I and runs II, III in terms of $cS2_b$ are caused by a modified hardware trigger for the S2 signal. In case of cS1 an estimation of the total uncertainty of the acceptances shows an error of less than 20 %, based on differences in ER and NR data as well as in the selection of the control sample. With respect to the larger uncertainties in the signal and background models (see below), the uncertainty of the cut acceptance is negligible. Due to an extended calculation of the signal model for both observables (see below), the S1, cS1 and S2 thresholds are accounted for in the signal model and do not need to be considered by an acceptance loss [111].

3.3 WIMP signal model

A major improvement of this combined analysis is the extension of the computed signal model to the use of the charge signal (S2). For previous results [89][85], only the cS1 parameter was used as the energy scale $\mathcal{L}_{eff}$ was better constrained by external measurements (see left panel of figure 2.3). The absolute matching between a Monte Carlo simulation of the cS1 and $cS2_b$ distribution of the AmBe source and NR calibration data constrains the energy scale Q_y (see section 2.2.3) for cS2s sufficiently well, enabling the extension of the signal model to the cS2 parameter [91]. By using both observables all cut acceptances and applied energy thresholds can be accounted for in their natural parameter space without further assumptions.

The equations for the signal model are derived in section 1.6 but are stated here again for clarity. The rate equation is given by equation 1.12,

$$\frac{dR(m_\chi, \sigma)}{dE} = \frac{\rho_0}{m_\chi \cdot m_A} \cdot \int v \cdot f(v) \cdot \frac{d\sigma}{dE}(E, v)\, dv, \tag{3.1}$$

with $E := E_{nr}$ and using a value for the local dark matter density of $\rho_0 = 0.3\ \mathrm{GeV/cm^3}$ [113]. An isothermal WIMP halo is assumed for the velocity distribution f with an escape velocity of $v_{esc} = 544$ km/s [114] and a local circular velocity of $v_0 = 220$ km/s. The differential cross-section $\frac{d\sigma}{dE}$ is given by equation 1.8. The signal model is individually computed for SI and SD interactions, defined by equation 1.10 and 1.11, respectively.

According to [85] the differential event rate can be expressed explicitly by the detector observables, leading to

$$\frac{d^2R(m_\chi, \sigma; \mathcal{L}_{eff}, \mathrm{LCE}, Q_y)}{d(\mathrm{cS1})d(\mathrm{cS2_b})} \approx \epsilon(\mathrm{S1})\epsilon(\mathrm{cS1})\epsilon(\mathrm{cS2_b}) \cdot \int \frac{dR}{dE} \cdot p(\mathrm{cS1}|E, \mathcal{L}_{eff}, \mathrm{LCE}) \cdot p(\mathrm{cS2_b}|E, Q_y) dE, \tag{3.2}$$

where $\epsilon(\mathrm{S1})$, $\epsilon(\mathrm{cS1})$, and $\epsilon(\mathrm{cS2_b})$ account for the signal acceptances shown in figure 3.4. The probability density functions (PDFs), p, for cS1 and $cS2_b$ are computed according

to the procedure in [85]. Equation 3.2 is simplified by $p(\mathrm{cS1}, \mathrm{cS2}) \approx \mathrm{p(cS1)} \cdot \mathrm{p(cS2)}$, assuming a negligible anti-correlation between S1 and S2 signals for NRs [91]. The pdfs for the cS1 and cS2 signals are computed by a Poisson convolution of a monoenergetic energy deposition to account for a small number of detected signal quanta. A subsequent Gaussian convolution reflects the PMT resolution [85] of 50 %. The scintillation signal as measured by generated photoelectrons n is given by

$$p(cS1|E_{nr}) = \sum_n \mathrm{Gauss}(cS1|n, \sqrt{n}\sigma_{PMT})\mathrm{Poi}(n|\nu(E(cS1))), \tag{3.3}$$

with the expectation value for the recoil energy $\nu(E(cS1)) = \mathcal{L}_{eff}(E_{nr}) \cdot E_{nr} \cdot L_y \cdot \frac{S_{nr}}{S_{ee}}$ defined by equation 2.1. Accordingly, for the proportional scintillation signal

$$p(cS2|E_{nr}) = \sum_n \mathrm{Gauss}(cS2|n, \sqrt{n}\sigma^{cS2}_{PMT})\mathrm{Poi}(n|\nu(E(cS2))), \tag{3.4}$$

with the expectation value $\nu(E(cS2)) = Q_y(E) \cdot E_{nr} \cdot Y$ defined by equation 2.2 and

$$\sigma^{cS2}_{PMT} = \sqrt{(\sigma_Y \cdot \sqrt{cS2})^2 + \sigma^2_{\mathrm{scaling}}}. \tag{3.5}$$

Here σ_Y is defined by the uncertainty on Y and $\sigma_{\mathrm{scaling}}$ is the uncertainty induced by scaling cS2 to $\mathrm{cS2_b}$. The uncertainty of the former are at the level of ~ 35 %, the latter at 5 %. The scaling is necessary as only cS2 values are calculated which are then scaled to $\mathrm{cS2_b}$ by a constant factor. An example for the signal smearing procedure is shown in figure 3.5. The calculation starts from a monoenergetic SI interaction of 10 $\mathrm{keV_{nr}}$ recoils (green dashed line) assuming a 50 GeV/c^2 WIMP and derives the cS1 (left) and cS2 (right) distributions of reach run. The distributions are computed without

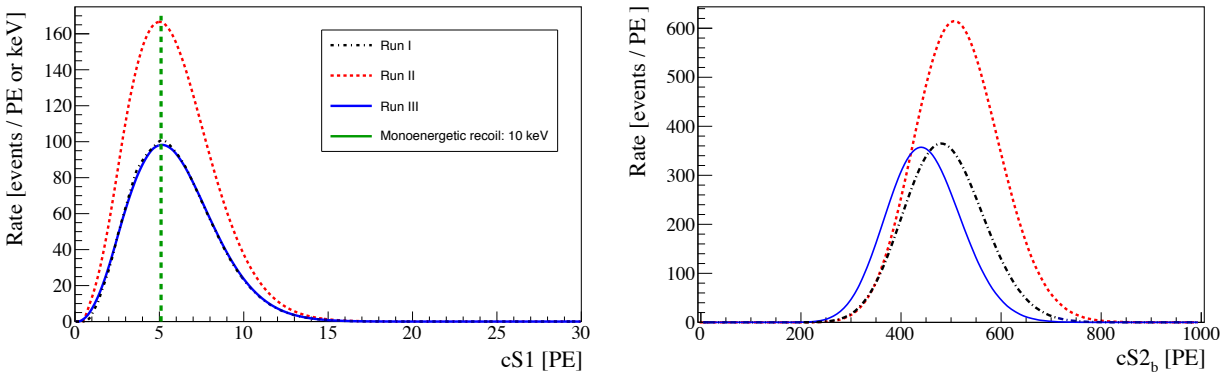

Figure 3.5: Calculated detector response for a 10 $\mathrm{keV_{nr}}$ recoil assuming a 50 GeV/c^2 WIMP interaction (green dashed line) in S1 (left) and S2 (right) for the three runs without consideration of energy thresholds.

the corresponding acceptances and consideration of the energy thresholds. The similar S1 distribution of run I and III is explained by a comparable exposure of the two runs

as the shorter run I compensates the exposure with a larger fiducial volume. Science run II features the largest exposure. The horizontal shift of the S2 distributions stem from different S2 amplifications factors, Y, as shown in table 3.1.

The total number of expected events of a specific WIMP energy spectrum is computed by the integral of equation 3.2 under consideration of the S1 and S2 thresholds

$$N_s(m_\chi, \sigma, \mathcal{L}_{eff}, LCE, Q_y) = \int_{\mathrm{S1}=3}^{30} \int_{\mathrm{cS2_b}=63;124}^{\mathrm{cS2_b^{up}}} \frac{d^2R}{d(\mathrm{cS1})d(\mathrm{cS2_b})} d(\mathrm{cS1})d(\mathrm{cS2_b}), \tag{3.6}$$

where $\mathrm{cS2_b^{up}}$ is chosen large enough to include the whole ER band. Normalizing equation 3.2 results in the signal pdf,

$$f_s(\mathrm{cS1}, \mathrm{cS2_b}; m_\chi, \mathcal{L}_{eff}, \mathrm{LCE}, Q_y) = \frac{\frac{d^2R}{d(\mathrm{cS1})d(\mathrm{cS2_b})}}{\int_{\mathrm{cS1}=0}^{30} \int_{\mathrm{cS2_b}=0}^{\mathrm{cS2_b^{up}}} \frac{d^2R}{d(\mathrm{cS1})d(\mathrm{cS2_b})} d(\mathrm{cS1})d(\mathrm{cS2_b})}. \tag{3.7}$$

The final signal models including the energy thresholds and acceptances are shown in figure 3.6. The green line in the left panel shows the initial energy spectrum of $8\,\mathrm{GeV}/c^2$ WIMP SI interactions calculated by equation 3.2 and 1.10. A small WIMP mass is chosen to illustrate the importance of the smearing procedure at recoil energies close to the energy threshold of the detector. The resulting signal spectra projected

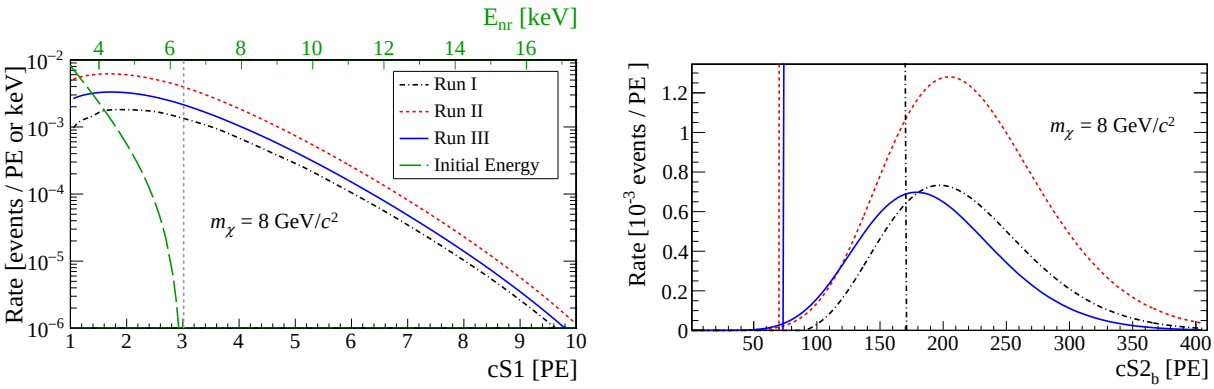

Figure 3.6: (Left) Computed SI signal model for an $8\,\mathrm{GeV}/c^2$ WIMP mass projected in cS1 for each science run. The energy spectrum of the WIMP is shown by the green dashed line in units of $\mathrm{keV_{nr}}$. A LCE value of 1 is assumed, resulting in an energy threshold of S1 = cS1 = 3 PE (vertical dashed line). (Right) Signal model projected in $\mathrm{cS2_b}$ with vertical dashed lines indicating the corresponding S2 energy threshold in each run. Differences in the cS1 and cS2 spectra among the runs are caused by changes in the exposure, S2 threshold and acceptances. Figures published in [106].

in cS1 and $\mathrm{cS2_b}$ are shown for each run in the left and right panel, respectively. As an example, but representative for all LCE values, a value of 1 is used such that the energy threshold is cS1 = S1 = 3 PE $\approx 6.6\,\mathrm{keV_{nr}}$. The figure shows that the end point energy of the $8\,\mathrm{GeV}/c^2$ WIMP spectrum is lower than the S1 threshold of 3 PE. Hence,

XENON100 is only sensitive to low mass WIMPs due to fluctuations of the observed signals above the energy threshold.

This significant impact of the fluctuations to the expected signal has been qualitatively tested with a YBe neutron source featuring an endpoint energy of 4.5 $\mathrm{keV_{nr}}$ below the average energy threshold of 3 PE (6.6 $\mathrm{keV_{nr}}$) if applied to the corrected S1. By applying similar cuts [115] as in the dark matter analysis, the measured NR events are shown in figure 3.7. The vertical red lines indicate the energy thresholds applied

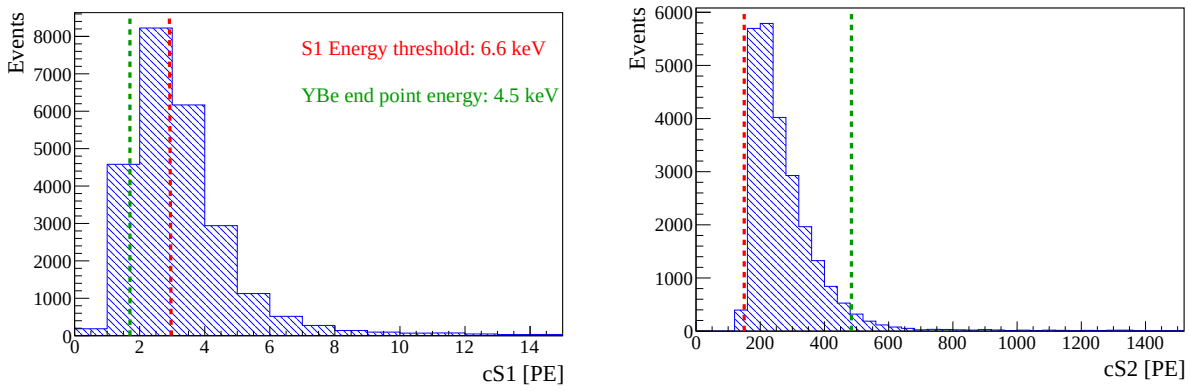

Figure 3.7: YBe NR calibration data [115] projected in cS1 (left) and cS2 (right). The vertical red lines indicate the energy threshold of 3 PE (6.6 $\mathrm{keV_{nr}}$) in cS1 and 150 PE (1.7 $\mathrm{keV_{nr}}$) in cS2. The end point energy of the YBe spectrum at 4.5 $\mathrm{keV_{nr}}$ in terms of cS1 and cS2 is shown by the green dashed lines.

to the S1 and S2 size. In case of the scintillation signal (left) the energy threshold of 3 PE (6.6 $\mathrm{keV_{nr}}$) is higher than the endpoint energy of YBe at 4.5 $\mathrm{keV_{nr}}$ (vertical green line). The Poisson distribution of the photon detection causes fluctuations above the threshold. The S2 energy threshold of 150 PE (1.7 $\mathrm{keV_{nr}}$), however, is below the YBe endpoint energy and signal fluctuations have a smaller impact close to the energy threshold.

In addition, the result of this analytically computed signal model is tested against a detailed Monte Carlo simulation of nuclear recoils in the TPC [91]. The Monte Carlo simulation is, in general, more precise as it considers all known spatial dependent effects of interactions inside the TPC. However, the simulation is more time consuming compared to the analytically calculated models. Differences among the two approaches are of the order of a few percent and show a sufficiently good agreement for all tested WIMP masses.

Following the method of [116] each signal model is divided into 8 bands with respect to cS1 and $\mathrm{cS2_b}$ where each band contains an equal number of expected signal events. Previously these bands were defined by AmBe neutron data [85], neglecting the differences of the energy spectrum of WIMPs and the calibration source. Due to the extended signal model the bands can now be defined by the signal pdfs alone as indicated in figure 3.8. The figure shows run III data (black dots) and the contribution of background in blue. The change of shape of the bands due to a different WIMP

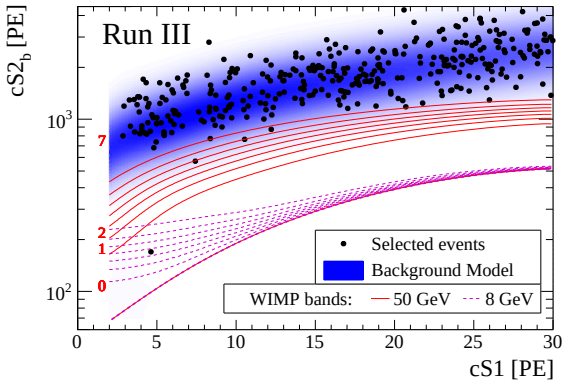

Figure 3.8: The change of the signal shape is shown by bands derived from 8 GeV/c^2 (magenta dashed lines) and 50 GeV/c^2 (red solid lines). The red numbers label the 50 GeV/c^2 bands. As a reference science run III data (black dots) is displayed including the position of the main background (blue filled region). Figure published in [106].

mass is indicated by the magenta and red lines calculated by the signal models defined by 8 GeV/c^2 and 50 GeV/c^2 WIMP interactions, respectively. The WIMP mass dependent banding, defined by the area between two lines (see red numbers on the left), exploits the precise knowledge of the signal shape and enables an improved statistical interpretation in regions with a high signal to background ratio. In particular, the bands are defined with respect to each run, WIMP mass and LCE value and nominal values of $\mathcal{L}_{eff}$ and Q_y. Due to the significantly changing signal shape between low and high WIMP masses the total number of considered dark matter events in the signal region could change. To keep the total number of analyzed events constant, a lower bound of the signal model is defined by the 99.7% acceptance line of the 20 GeV/c^2 WIMP signal model. This lower bound of the band definition is not only applied to the data but also accounted for in the signal and background model. A similar approach is used in [85], however the lower boundary is defined on AmBe NR calibration data which neglects the shape differences to a WIMP spectrum. For a 8 GeV/c^2 WIMP mass this caused an over-estimation of the acceptance of up to 10 % which is avoided by this improved method.

3.4 Background model

The background model of XENON100 constitutes of an ER and NR component. While the NR background is derived similar to [85], the estimation of the ER background is modified to improve the quantification of accidental coincidences.

The NR background pdf, f^{NR}, is estimated by a detailed Monte Carlo simulation of radiogenic, f^{NR}_{RG}, and cosmogenic, f^{NR}_{CG}, induced neutron events in the XENON100 target [97]. The former stems from ambient materials in vicinity of the fiducial volume, the latter originates from remaining cosmic radiation and their secondary processes. The

computed energy spectra are mapped in the cS1 and $cS2_b$ parameter space, following the same procedure as introduced in section 3.3 and under consideration of the varying exposures. The total NR contribution is given by the sum of the two components

$$f^{NR} = f^{NR}_{RG} + f^{NR}_{CG}, \tag{3.8}$$

and shown in the bottom left panel of figure 3.9. The expected background rate is indicated by the color coded scale.

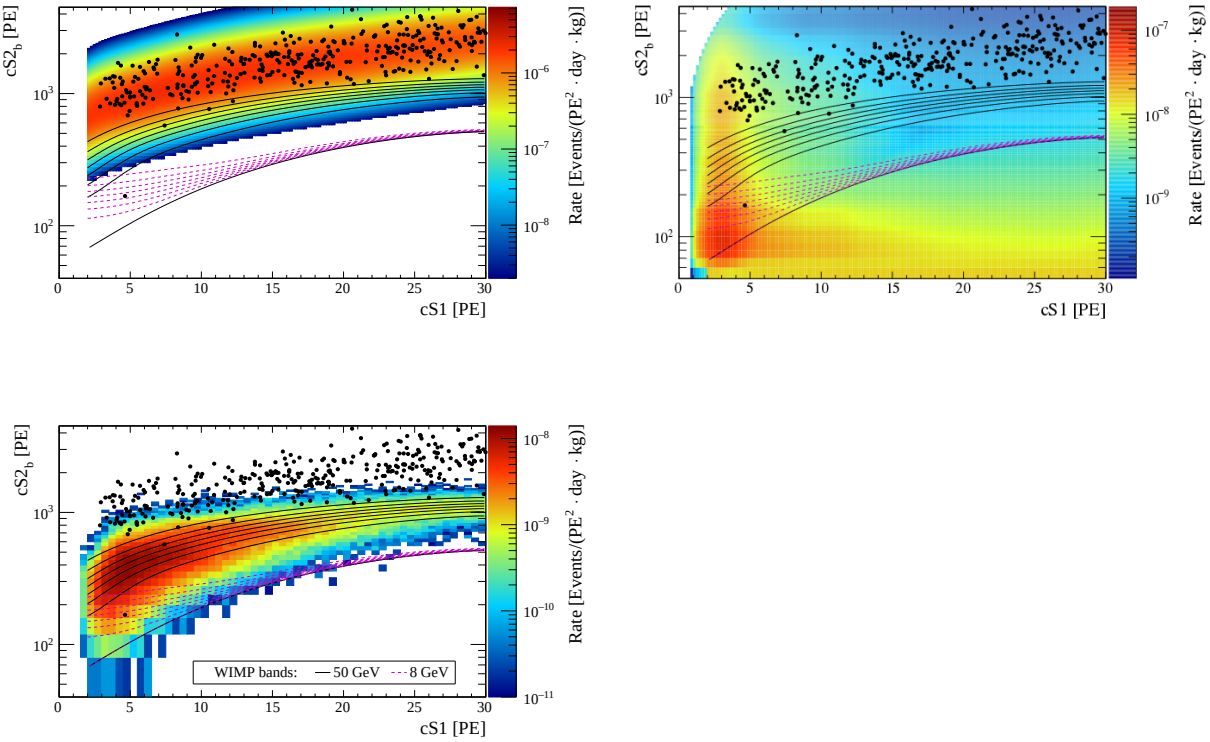

Figure 3.9: The total background component constitutes from contributions of a ER Gaussian (top left), non-Gaussian (top right) and a NR (bottom (left) part. The color coded scales indicate the expected background rate in the $cS2_b$-cS1 parameter space. The background models and data (black dots) are shown for run III but are representative for the other runs. For reference, bands from the 8 GeV/c^2 (magenta) and 50 GeV/c^2 (black) signal models are overlaid. Figures from [106].

The ER background, in contrast to the NR background, is determined entirely by calibration data. This approach relies, in general, on fewer assumptions but suffers from insufficient statistics from rare processes. The main contribution can be calibrated with high statistics and is modeled by a Gaussian distribution as shown in the top left panel of figure 3.9. These events mainly stem from Compton scattering of particles produced by the decay of the radioactive elements in the detector materials. This Gaussian shape, f^{ER}_G, estimated from calibration data [85] is then scaled to the dark matter science run based on the events above the signal region.

	Run I	Run II	Run III
Gaussian	64 ± 6	55 ± 8	72 ± 7
Non-Gaussian	33 ± 5	35 ± 7	19 ± 4
NR	3 ± 2	10 ± 7	9 ± 7
Measured events in ROI	3	1	1
Expected events in ROI	3.9 ± 0.5	1.7 ± 0.3	1.0 ± 0.2

Table 3.2: Contribution in [%] of each component of the background model in the ROI including the total number of expected and measured events.

In addition, a non-Gaussian or anomalous ER component, f_{AN}^{ER}, has been observed [85] which is not correctly modeled by f_{G}^{ER}. The origin of these events is unknown, but they might be caused by events with incomplete charge collection or accidental coincidences (AC) of randomly paired lone S1s and S2s. While the former can be calibrated (with low statistics) and scaled to the dark matter data, the latter must be estimated from the lone S1 and S2 distributions as present during the dark matter run. A higher event rate during the ER calibration of the detector or time varying lone S1 rates as shown in figure 3.2 could bias the AC estimation. Hence, the AC background is in one part estimated by a non-Gaussian contribution of events as found in ER calibration data [85], f_{AN}^{ER}, and in the other part by an AC rate as present in dark matter data, f_{AC}^{DM} [106]. To avoid a bias from AC events in ER data, f_{AC}^{ER}, its contribution is subtracted from f_{AN}^{ER}. Combining the various components results in the non-Gaussian ER background model,

$$f_{NG}^{ER} = f_{AC}^{DM} + \max\left((f_{AN}^{ER} - f_{AC}^{ER}), 0\right), \tag{3.9}$$

and is displayed in the top right panel of figure 3.9. The relative contribution of each component is listed in table 3.2. For comparison, also the total measured and expected events are shown. The dominant background in run I is caused by a large ^{85}Kr concentration resulting in a large Gaussian component and a smaller relative contribution of NR background with respect to run II and III. The non-Gaussian component is reduced in run III, compared to run II due to a smaller predicted AC contribution, which could stem from improved cut optimizations in run III. In comparison to the first publication of run I [89] and run II [85] with a background prediction of 1.8 ± 0.6 and 1.0 ± 0.2, respectively, the new background model predicts a larger background in the ROI due to the AC contribution.

The combined background pdf f_b of the NR, ER and AC component is then given by

$$f_b = f^{NR} + f_{G}^{ER} + f_{NG}^{ER}. \tag{3.10}$$

Figure 3.10 illustrates the different contributions of various background sources with respect to the signal model. The two-dimensional models ($cS2_b$ vs. cS1) are projected to the cS1 parameter for band 0 (left) and 2 (right). The band numbers refer to the red numbers in figure 3.8. The dominant change of the Gaussian background component between the two panels reflects the optimized signal to background ratio in the lower bands by considering the signal shape in the band definition.

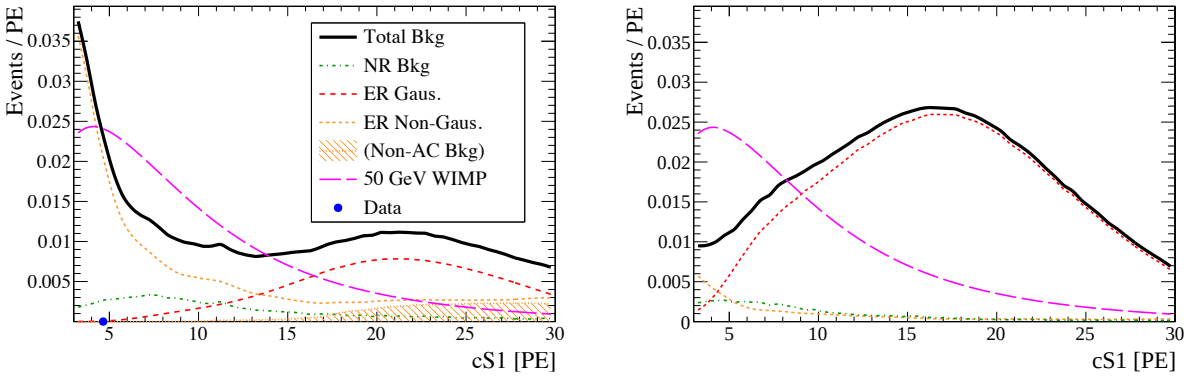

Figure 3.10: As an example, but representative for all bands, the left and right panel indicate band 0 and 2, respectively, defined by the 50 GeV/c^2 WIMP SI model (see red numbers in figure 3.8 for the band labels). The signal shape for a WIMP cross-section of $\sigma_{SI} = 10^{-45}$ cm^2 is represented by the long-dashed magenta line and the total background is indicated by the black line. The various contributions to the background model which are mentioned in the text are illustrated by the colored lines. The blue dots display the cS1 position of events in the ROI of run III. Figure from [106].

The concept of dividing the signal model into bands originates from the previous PL analysis [116], to be able to define a statistical uncertainty of the background model. In particular, and explained in detail in section 3.5, the total number of ER calibration events, calculated for each band, model effectively the uncertainty by a Poisson distribution (black dashed line in figure 3.11). The systematic error is cross-checked by an estimation of uncertainties from the various background components as well as the uncertainty of NR backgrounds induced by the Monte Carlo simulation [97]. The individual (colored lines) as well as the total combined uncertainty (gray line) is shown in figure 3.11. Due to the limited statistics of the anomalous leakage component in the calibration sample, the statistical uncertainty is significantly larger than systematic uncertainties arising from the background modeling. In the following, this systematic shape uncertainty of the background pdf will be neglected and is subject of chapter 4.

3.5 The likelihood function

The statistical interpretation of the data is performed by a profiled likelihood ratio test as introduced in section 1.7 and follows, in general, the procedure of [116]. The likelihood function for the run combination is expressed by the product of all relevant run-specific likelihoods and their constraining terms

$$\mathcal{L} = \mathcal{L}^{I} \times \mathcal{L}^{II} \times \mathcal{L}^{III} \times \mathcal{L}_3(t_{\mathcal{L}_{eff}}) \times \mathcal{L}_4(t_{Q_y}). \tag{3.11}$$

The likelihood contains the science runs $\mathcal{L}^{I}, \mathcal{L}^{II}, \mathcal{L}^{III}$ in one part and the other part is given by constraint terms for global nuisance parameters governed by external light

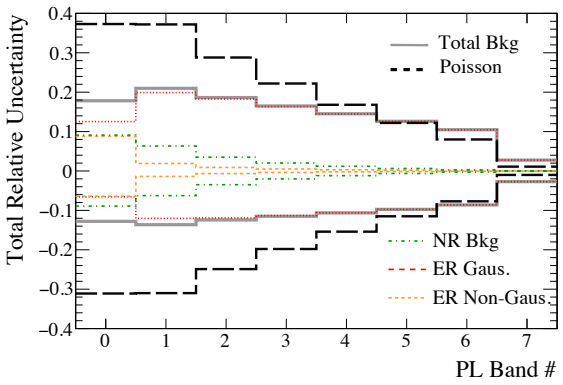

Figure 3.11: Modeled uncertainties of the ER Gaussian (red), ER non-Gaussian (orange) and NR (green) background components for each band. The total systematic uncertainty is shown in black. The pure statistical uncertainty for each band defined by the ER calibration data is shown in gray. The positive and negative lines indicate asymmetric errors. Figure from [106].

and charge yield measurements (section 2.2.3) $\mathcal{L}_3, \mathcal{L}_4$. The likelihood function for each run, i, is given by

$$\mathcal{L}^i = \mathcal{L}_1^i(m_\chi; \sigma, N_b^i, \epsilon_b^i, t_{\mathcal{L}_{eff}}, t_{Q_y}) \times \mathcal{L}_2^i(\epsilon_b^i). \tag{3.12}$$

where ϵ_b^i denotes a vector of nuisance parameters for the background model in each band j. Furthermore, each science run contains the extended likelihood function

$$\mathcal{L}_1^i = \prod_j^{K^i(m_\chi)} \text{Poiss}\left(n^{i,j} | \epsilon_s^{i,j} N_s^i(\sigma) + \epsilon_b^{i,j} N_b^i\right) \times \prod_{k=1}^{n^{i,j,k}} \frac{\epsilon_s^{i,j} N_s^i(\sigma) f_s^{i,j}(\text{cS1}^k) + \epsilon_b^{i,j} N_b^i f_b^{i,j}(\text{cS1}^k)}{\epsilon_s^{i,j} N_s^i(\sigma) + \epsilon_b^{i,j} N_b^i}, \tag{3.13}$$

with the Poisson distribution of the observed events $n^{i,j}$ (for each run i and band j) and the maximum likelihood estimators (MLEs) N_s^i and N_b^i of the total number of signal and background events, respectively. The number of estimated signal events N_s later constrains the WIMP cross-section σ. The likelihood is computed in each of the 8 bands $K^i(m_\chi)$ while considering varying band shapes for different WIMP masses m_χ. The parameters ϵ_s^i and ϵ_b^j describe the fraction of the expected signal and background in each band, respectively, derived from the corresponding models. While the scaling parameter ϵ_s is fixed, ϵ_b is a nuisance parameter in the likelihood. The second part of equation 3.13 is a product of the probability for each event, k, considering the signal and background shape in cS1. In equation 3.13, the explicit dependencies of N_s^i, $\epsilon_s^{i,j}$, and f_s^i on $t_{\mathcal{L}_{eff}}$, t_{Q_y}, and LCE are not indicated to maintain a readable equation.

Uncertainties of the background pdf are modeled by the statistical uncertainty in each band, as shown in figure 3.11 by the black dashed line, and are profiled out using

the nuisance parameter ϵ_b^i constrained by a Poisson distribution,

$$\mathcal{L}_2^i = \prod_j^{K^i(m_\chi)} \text{Poiss}(m_b^{i,j} | \epsilon_b^{i,j} M_b^i). \tag{3.14}$$

The equation contains the total number of ER calibration events, M_b^i, per run and the number of ER events, $m_b^{i,j}$, in each band.

The global nuisance parameters $t_{\mathcal{L}_{eff}}$ and t_{Q_y} model uncertainties in the energy scales as shown in [89] and are constrained by a Gaussian distribution,

$$\mathcal{L}_{3,4}(t_{\mathcal{L}_{eff},Q_y}) = exp(-(t_{\mathcal{L}_{eff},Q_y})^2/2). \tag{3.15}$$

Finally, by maximizing the full likelihood for all three science runs for a given $N_s^i(\sigma)$, the cross-section, σ, is computed by equation 3.6.

3.6 WIMP search results

The results of the combination of the three runs are independently shown for SI and SD interactions. The former is shown in figure 3.12, the latter in figure 3.13, while both figures include various other results of dark matter experiments as a reference. The statistical interpretation of the data by means of the PL method results in a 90 % confidence level (CL) limit using the CL_s prescription of [117]. In addition, the sensitivity bands, estimated from the distribution of upper limits for the background only hypothesis are indicated by green (1σ) and yellow (2σ) bands. As a benchmark value, the upper limit on the WIMP-nucleon SI cross-section of the combined result is $1.1 \times 10^{-45}\,\text{cm}^2$ for a $50\,\text{GeV}/c^2$ WIMP mass (figure 3.12), improving the previous limit from [85] by a factor of 1.8. In case of SD interactions, again for a $50\,\text{GeV}/c^2$ WIMP mass, the benchmark cross-section for proton coupling is $5.2\times10^{-39}\,\text{cm}^2$ and for neutron coupling $2.0\times10^{-40}\,\text{cm}^2$ (figure 3.13), improving the result of [121]. The combined XENON100 result confirms the absence of WIMP dark matter in terms of SI and SD interactions as measured previously in XENON100 [85] and by other detectors as shown in figures 3.12 and 3.13.

3.7 Discussion

In this chapter a combined analysis of the three major dark matter science runs of XENON100 is presented. The combined data includes 477 live days measured between 2010 and 2014 resulting in an exposure of $1.75\times10^4\,\text{kg}\cdot\text{day}$, reflecting the longest dark matter search campaign by a dual phase LXe TPC to this date. This dataset consists of two previously published science runs and a new third run. Various improvements in the data selection are outlined and are applied to all runs which improve the purity of the dark matter event selection. In addition, the lower energy thresholds are now applied directly on the observed S1 and S2 signals prior to any size corrections. This modification of the analysis results in a variable energy threshold exploiting the high

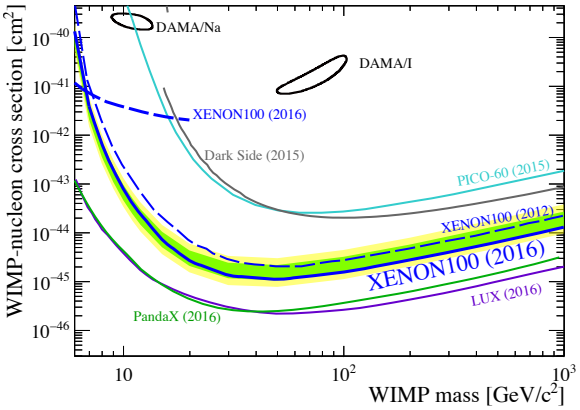

Figure 3.12: Combined SI result of XENON100 (blue line) including the $1\,\sigma$ (green band) and $2\,\sigma$ (yellow band) expected sensitivity at 90% CL. Current results from other experiments are shown as a reference [72, 85, 118, 119, 104, 73, 120]. Figure published in [106].

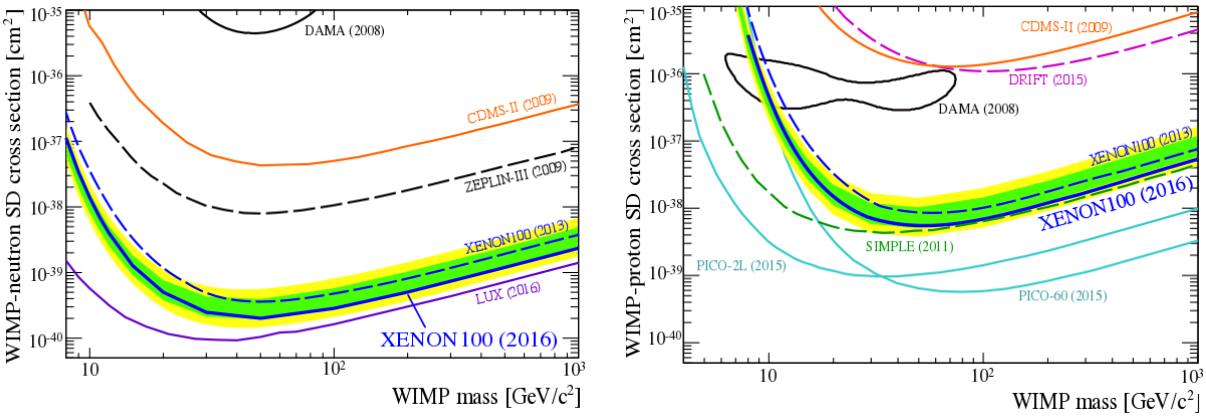

Figure 3.13: Combined SD result of XENON100 (blue line) including the $1\,\sigma$ (green band) and $2\,\sigma$ (yellow band) expected sensitivity at 90% C, individually computed for neutron (left) and proton (right) coupling. Current results from other experiments are shown as a reference [122, 118, 77, 123, 121, 124, 125, 126, 127]. Figures published in [106].

light collection efficiency of the TPC close to the bottom PMT array. The improved threshold condition also features a more robust analysis in regions with reduced light collection, generally present for interactions in vicinity to the liquid-gas surface. Furthermore, major improvements of the signal as well as in the background model are outlined. An analytic computation of the signal model is now extended to both observables, cS1 and $\mathrm{cS2_b}$, enabling a more robust and improved analysis. By defining bands according to the two dimensional signal shape in the cS1 and $\mathrm{cS2_b}$ parameter space, the signal to background ratio of the PL analysis is optimized. The extended signal

model allows the consideration of all cut acceptances in terms of their primary parameter reducing systematic uncertainties. The background model is modified to estimate the shape of accidental coincidences which improves the modeling of the non-Gaussian ER component. The profile likelihood analysis is modified to account not only for run specific detector conditions but considers correlated nuisance parameters among the runs. As a result, the statistical interpretation of the data by means of the PL method confirms the absence of events induced by WIMPs scattering off the target nucleus and improves the limits by a factor of 1.8 for SI and SD interactions. The maximal sensitivity is achieved for $50\,\mathrm{GeV/c^2}$ WIMPs with a SI limit of $1.1\times10^{-45}\,\mathrm{cm^2}$ and a SD neutron (proton) limit of $2.0\times10^{-40}\,\mathrm{cm^2}$ ($5.2\times10^{-39}\,\mathrm{cm^2}$).

Despite the various mentioned changes of this analysis with respect to previous XENON100 publications (e.g. [85]) further improvements are possible. Due to the artificial binning of the data into WIMP mass dependent bands information within a band about the S2 signal shape is lost. An unbinned PL analysis would, therefore, exploit more information about the expected signal, enhancing the sensitivity of the experiment. This would require, however, a method to correctly model the uncertainties of the background model as the current statistical error for the background model would vanish. Also the origin of the non-Gaussian ER background component remains unknown and a phenomenological parameterisation of this event population might underestimate shape uncertainties due to limited statistics in the calibration sample. Hence, the improvement of this analysis must be twofold. It should exploit the benefits of a full unbinned profile likelihood analysis and has to model the background from limited statistics in absence of a physically motivated parametric pdf. A possible solution to this problem is given in the next chapter.

Chapter 4

Shape uncertainties of the XENON100 background model

In this chapter, a method is introduced aiming to improve the analysis presented in chapter 3, namely the lack of a procedure to address shape uncertainties of the background model in the likelihood function. As a consequence, uncertainties were effectively modeled by artificially binning the analyzed parameter space. This allowed to define a statistical error, but the complete knowledge of the signal shape in terms of the scintillation and charge signal could not be exploited in its full extend (see section 3.7). In this chapter, a twofold solution is presented. Firstly, an improved estimation of the data driven background model is developed in absence of a physical motivation for a parametric model. Secondly, a modification of the likelihood function allows to consider the shape uncertainties of a non-parametric background pdf to the likelihood function. A combination of both procedures enables, for the first time, a complete unbinned analysis of the XENON100 data.

The content of this chapter is structured as follows. In section 4.1 the problem of modeling uncertainties in the XENON100 analysis is outlined. A non-parametric method to derive the background pdf is illustrated in section 4.2 and the modified likelihood function to account for shape uncertainties is presented in section 4.3. An example analysis of Monte-Carlo-generated data for the proposed method is given in section 4.4. Finally, in section 4.5 the method is applied to XENON100 data and results are shown in the minimal velocity parameter space. Sections 4.1, 4.3 and 4.4 are based on an article [128] where the author of this thesis contributed significantly to the analysis and is the second author.

4.1 Modeling of shape uncertainties

The modeling of the shape of the signal and background pdf is of particular importance if the data is analyzed by means of a profile likelihood (PL) method as introduced in section 1.7. In contrast to other methods, the PL technique is designed to exploit the shapes of the signal and background pdf, assuming that all uncertainties are accounted for and correctly parameterized. Only then, results of a likelihood ratio test can show

the correct statistical behavior. Examples exist, in which dark matter experiments observed an excess of events above the background estimation [129, 130], only to demonstrate afterwards that it stems from an underestimated background [131, 132, 133]. Possible sources of mistakes are manifold. Some experiments cannot simulate their background due to very rare signatures of events with unknown origin. Due to the low probability of these event topologies, dedicated calibration campaigns might still lack sufficient statistics. In addition, time consuming Monte Carlo simulations of rare processes might fail to provide a background model with low statistical uncertainty and high accuracy of the pdfs shape (e.g. [97]).

The PL method features a natural prescription to account for systematic and statistical uncertainties of nuisance parameters while gaining sensitivity by exploiting the shape of the signal f_s and background f_b pdfs (see section 1.7). A generic likelihood equation used in rare event searches for N_s signal events in presence of N_b background events is defined by equation 1.14. For illustration, a simplified likelihood function is defined by

$$\mathcal{L} = \text{Poiss}(N|N_s + N_b) \prod_{i=1}^{N} \frac{N_s f_s(x_i) + N_b f_b(x_i)}{N_s + N_b}, \tag{4.1}$$

if no uncertainties are assumed in the signal and background pdf. For N total measured events, the first part of the equation describes the Poisson nature of a counting experiment. The product in equation 4.1 considers the shape of the background and signal pdfs. Furthermore, the pdfs depend on the position x, or on a multidimensional vector $\vec{x}$, of the measured events. By using the PL ratio test statistic q defined by equation 1.15, hypothesis tests of the background-only or signal-and-background hypotheses can be performed. In the following, a data analysis performed by equation 4.1 is referred to as the *conventional method*. An example for a wrong modeling of the background pdf is shown in figure 4.1. The figure shows a Monte-Carlo-generated background-only

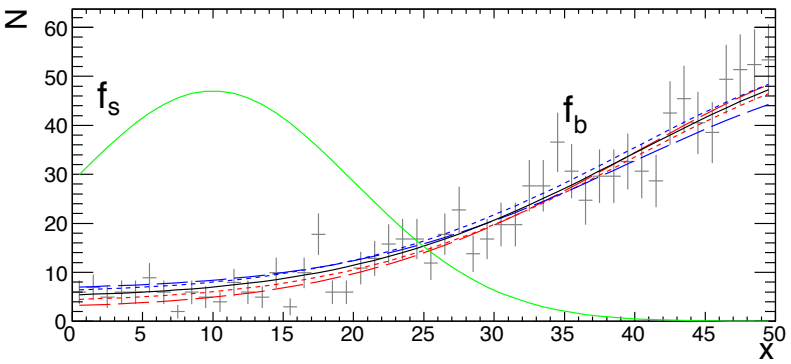

Figure 4.1: Example of a signal (green line) and background pdf (black line) superimposed to a Monte-Carlo-generated background dataset (black markers). The red (blue) lines indicate different levels for an underestimation (overestimation) of the background pdf. Figure published in [128].

dataset (black markers), representing a *science dataset* from which N_s is estimated.

The shape of the background pdf is shown by the black line and the signal pdf is indicated by the green line. A background reference dataset (*calibration dataset*) is used to estimate the background pdf (blue and red lines) as, in general, the true background model is unknown. By construction, the red lines underestimate the true background pdf whereas the blue lines indicate pdfs with an overestimated background. For each Monte-Carlo-generated science dataset with no injected signal events, the test statistic q_0 defined by equation 1.17 is computed and its cumulative density function (CDF) distribution is shown by figure 4.2. The expected $\frac{1}{2}\chi^2$ asymptotic distribution of the

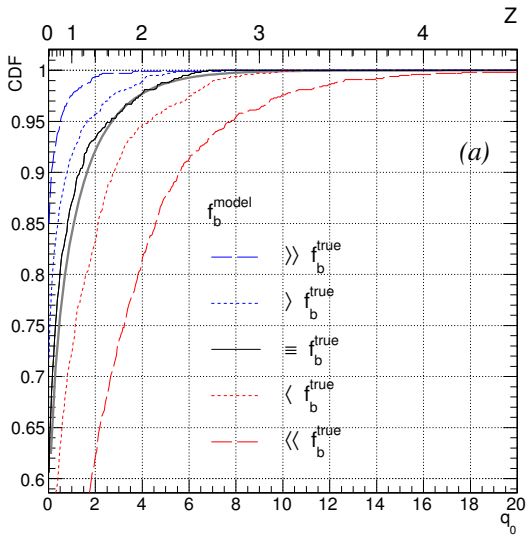

Figure 4.2: The cumulative density function of the discovery test statistic, $f(q_0|0)$ using the true background model (black) and 4 variations as shown in figure 4.1. The expected $\frac{1}{2}\chi^2$ asymptotic behavior is shown in gray. Figure published in [128].

likelihood ratio q_0 for testing the background only hypothesis (see section 1.7) is shown by the gray line. Using the correct background model (black), the q_0 distribution approaches the expected CDF. However, a biased estimation of the background pdf, leads to an over- or under-coverage as indicated by the blue and red lines, respectively. While an over-coverage (derived CDF steeper than a $\frac{1}{2}\chi^2$ distribution) results in conservative confidence levels, an under-coverage would result in an enhanced significance of an identified signal component which might be caused by statistical fluctuations of the background. The latter is particularly dangerous for experiments aiming to detect new particles. In the following sections a method is introduced to especially avoid under-coverage which could result in a false discovery of new physics phenomena.

4.2 Non-parametric density estimation

As mentioned before, the background model in XENON100 (see chapter 3) stems from a phenomenological parameterisation of the calibration data without a physical motivation of the fit function. As a consequence, a wrong choice of the fit function might

result in a bias, as illustrated by figure 4.2. In general, a parametric estimator $\hat{f}$ of the true background pdf makes use of a model $\hat{f}(x, \alpha_k)$ dependent on a vector of parameters α_k and observations x_i. The choice of the functional form of $\hat{f}$ as well as the parameters $\alpha_1, \alpha_2, ...$ should be, in general, motivated by the involved physical processes. A non-parametric ansatz avoids a model dependence of the density estimator $\hat{f}$ which is beneficial if a physics-motivated model is absent. The most common example of a non-parametric method is the histogram of the observations x_i which can be used as an estimator of the unknown parent distribution. However, in case of limited statistics of x_i, it is beneficial to avoid a binning of the data to reduce the unavoidable information loss within a bin. Furthermore, histograms are discontinuous while physical processes generally lead to a continuous distribution. In this section, the non-parametric and unbinned method of kernel density estimation (KDE) is introduced, which is used as an estimator of the parent distribution based on a limited number of observations.

4.2.1 Introduction to kernel density estimation

The basic idea of KDE is that each measured event at position x_i is represented by a kernel function K. By summing up all kernels for N events the kernel density estimate $\hat{f}$ of the parent density f is derived as,

$$\hat{f}(x) = \frac{1}{Nh} \sum_{i=1}^{N} K\left(\frac{x - x_i}{h}\right). \tag{4.2}$$

with the bandwidth h as a free parameter [134][135]. Various examples for kernel functions are shown by the colored lines in the left panel of figure 4.3 which are available in the ROOT framework [136]. Each observation x_i (black marker) is represented by a fixed choice of K and a bandwidth h (gray dashed line). For instance, in case of a Gaussian kernel, the bandwidth is identical to the width σ of a Gaussian distribution. For probability density estimation, the kernel function must satisfy the basic relations of probability theory:

- A kernel function $K(x) : \mathcal{R} \to \mathcal{R}$ can be any function satisfying $\int_{-\infty}^{\infty} K(x)dx = 1$
- A non-negative kernel satisfies $K(x) \geq 0 \, \forall \, x$.

The right panel of figure 4.3 illustrates a Gaussian kernel density estimate of several observations x_i. The distribution of the data is shown by the blue histogram which are randomly sampled from a fixed pdf (black). The estimate $\hat{f}^{KDE}$ is indicated by the red line. By increasing the number of sampled data points, the kernel density estimate approaches asymptotically the true pdf.

The function $\hat{f}^{KDE}$ depends on the choice of the bandwidth h and the kernel function K. Throughout this chapter, a Gaussian kernel is used. For h, several methods have been developed to derive the optimal value, given the data x_i. As an example, for normal distributed data the optimal bandwidth is given by [135]

$$h = \left(\frac{4}{3}\right)^{1/5} \sigma N^{-1/5}, \tag{4.3}$$

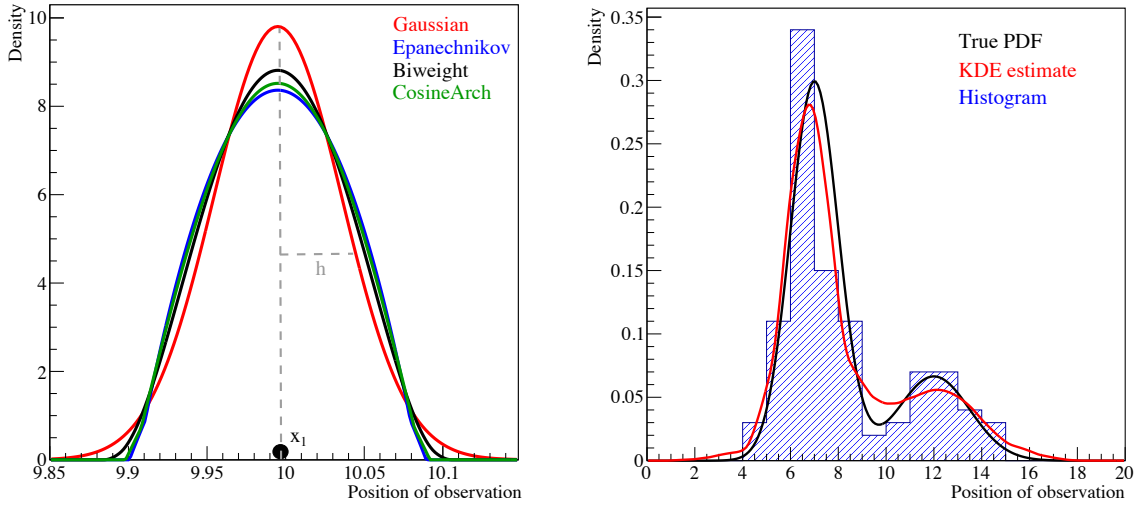

Figure 4.3: (Left) Various examples of commonly used kernel functions available in the root analysis framework [136]. (Right) The KDE method (red) in comparison to a histogram (blue) and the true distribution (pdf).

with the standard deviation σ of the data and N observed events. However, in case of non-uniform distributed data such as in long-tailed distributions, an optimal choice of the bandwidth is challenging. If the kernel estimate is sufficiently smoothed (large values of h) to describe the tails of the distribution, information in the main part of the distribution is lost due to an over-smoothing. This problem can be solved by exploiting a variable (or adaptive) bandwidth which accounts for differences in the data density and is explained in the following section.

4.2.2 Adaptive kernel density estimation

The optimal choice of the bandwidth reaches asymptotically zero in case of infinite statistics ($N \to \infty$). Thus, for a data sample with an inhomogeneous density distribution, denser regions should have a smaller bandwidth than regions with a low density. As a consequence, the bandwidth should be locally defined ($h_i = h(x_i)$) and is optimally performing when it scales inversely to the local observed density of the data sample, $h_i = h/\sqrt{f(h_i)}$ [137]. Accordingly, equation 4.2 can be modified, following the notation as in [135],

$$\hat{f}(x) = \frac{1}{N} \sum_{x_i=1}^{N} \frac{1}{h_i} \mathrm{K}\left(\frac{\mathrm{x} - \mathrm{x_i}}{\mathrm{h_i}}\right), \tag{4.4}$$

with the adaptive bandwidth h_i defined as:

$$h_i = \rho \cdot \left(\frac{4}{3}\right)^{1/5} \sqrt{\frac{\sigma}{\hat{f}_0(x_i)}} N^{-1/5}. \tag{4.5}$$

The adaptive bandwidth depends on the initial density estimate $\hat{f}_0$ computed with a fixed bandwidth. According to [135], the adaptive estimate $\hat{f}(x)$ is, in practice, independent of the initial dependency of the fixed kernel estimate $\hat{f}_0$. The factor ρ is commonly set to 1 and, only if the local standard deviation σ_{local} is two orders of magnitudes smaller than σ, it needs to be modified according to [135] by,

$$\rho = \sqrt{\frac{\sigma_{\text{local}}}{\sigma}}. \tag{4.6}$$

An illustration of the varying bandwidth is shown for a Gaussian kernel in figure 4.4. Events close together (x_3, x_4) result in a reduced bandwidth (h_4) due to the higher

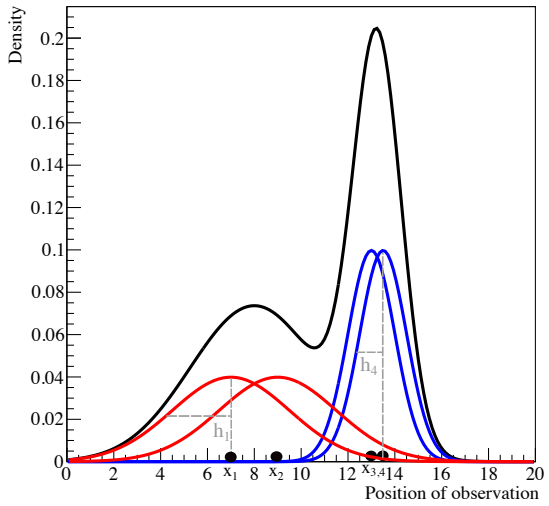

Figure 4.4: Example of adaptive kernel density estimation. In higher density regions (x_3, x_4) the bandwidth h_4 is smaller than in region with less density (x_1, x_2).

event density in this region of the parameter space. In contrary, two events further apart (x_1, x_2) are described with a larger bandwidth (h_1) accounting for the locally reduced statistics.

The fixed and adaptive KDE method defined by equation 4.2 and 4.4 can also be applied to higher dimensional density estimation [135].

An example for a two dimensional kernel is given by:

$$\hat{f}(x,y) = \frac{1}{N}\sum_{i=1}^{N}\left[\frac{1}{h_{x;i}\cdot h_{y;i}}K\left(\frac{x-x_i}{h_{x;i}}\right)\cdot K\left(\frac{y-y_i}{h_{y;i}}\right)\right] \tag{4.7}$$

with the two adaptive bandwidth $h_{y,i}$ and $h_{x,i}$ defined as,

$$h_{x,y;i} = \rho N^{-1/6}\left(\frac{\sigma_{x,y}}{\sigma}\right) f^{(-1/2)}(x_i, y_i). \tag{4.8}$$

In this case, the covariance structure of the data is assumed to be diagonal.

Due to the absence of parameters of the estimated pdf using KDE, it is not possible to define nuisance parameters which can be propagated to the profile likelihood analysis. Hence, a method is needed to correctly model the uncertainties arising by a non-parametric density estimate which can be accounted for in the likelihood function.

A possible usage of the bandwidth and ρ-parameter as a nuisance parameter in the likelihood ratio test was investigated to account for shape uncertainties. However, the induced shape perturbations of the background model did not account for all uncertainties in case of calibration sizes at the order of the science data. While an optimization of the background pdf estimation is possible by maximizing the likelihood for ρ, another approach is necessary to account for uncertainties which is introduced below.

4.3 Non-parametric shape uncertainties in likelihood functions

The shape uncertainty of f_b originates from limited statistics in the calibration sample combined with the absence of a physically motivated parametric background model. While the non-parametric kernel density estimate is model independent, it could still inherit shape uncertainties from insufficient statistics. By using the likelihood function as defined in equation 4.1, it is possible to restrict the estimation of background shape uncertainties in the region of the signal model. Hence, the uncertainties can be estimated similar to the shape term in equation 4.1 but applied to the calibration sample. This method, initially developed by the ATLAS collaboration [138], allows to identify a *spurious signal* in the calibration dataset. This is the case when the calibration sample shows locally a signal-like population which cannot be sufficiently well constrained by $\hat{f}_b$ due to low statistics. The likelihood function for the calibration dataset $\mathcal{L}_{cal}$ with n_c calibration events is then defined by

$$\mathcal{L}_{cal} = \prod_{i=1}^{n_c} \frac{n_s f_s(x_i) + n_b f_b(x_i)}{n_s + n_b} \tag{4.9}$$

with n_s signal and n_b background events contained in the calibration sample. Even though the calibration does not contain any signal events by construction, equation 4.9 can estimate the similarity of the calibration sample to the signal pdf. The number of n_s and n_b is of no particular interest, hence, equation 4.9 can be simplified to

$$\mathcal{L}_{cal} = \prod_{i=1}^{n_c} \epsilon f_s(x_i) + (1-\epsilon) f_b(x_i), \tag{4.10}$$

by a substitution of $\epsilon = \frac{n_s}{n_b+n_s}$. The term $\epsilon f_s(x_i) + (1-\epsilon) f_b(x_i)$ can be interpreted by a background model which is perturbed by the signal pdf by an amount ϵ. The level of a signal-like perturbation, however, is constrained by n_{cal} events. Combining equation 4.10 and 4.1 results in,

$$\mathcal{L}(N_s; N_b, \epsilon) = \mathcal{L}_{phys} \times \mathcal{L}_{cal}, \tag{4.11}$$

with the likelihood estimated on the science dataset $\mathcal{L}_{phys}$,

$$\mathcal{L}_{phys} = \text{Poiss}(N|N_s + N_b) \prod_{i=1}^{N} \frac{N_s f_s(x_i) + N_b(1-\epsilon) f_b(x_i) + N_b \epsilon f_s(x_i)}{N_s + N_b}. \tag{4.12}$$

4.3.1 Discovery tests

To verify the performance of the proposed modification of the likelihood function in equation 4.11, a likelihood ratio test for q_0 is performed on Monte Carlo data. For each simulation, 15 signal and 100 background events are randomly distributed according to f_s^{true} and f_b^{true}, respectively. The number of N_s and N_b are Poisson distributed. These events are merged to a single dataset, representing a science dataset from which the number of signal events are estimated. In addition, a background only calibration dataset is simulated, distributed according to f_b^{true} with 1000 events. These calibration events are used to estimate the background model f_b by various fits, as shown in figure 4.1. The distribution of the discovery potential Z, expressed in terms of standard deviations (see equation 1.16), of 15 injected signal events is shown in the 5 panels of figure 4.5. The top panel displays, as a reference to the optimal significance, the distribution if f_b^{true} is used to perform the likelihood ratio test (see section 1.7). The next two panels (red lines) show two background models which underestimate f_b^{true} at various levels, whereas the last two panels (blue lines) overestimate f_b^{true}. The solid lines show the result of the conventional likelihood ratio test. In case of an under (over)-estimation of f_b^{true} the discovery potential is larger (lower) than the reference distribution due to a biased estimation of the number of signal events N_s. By using the new modified likelihood function (dashed lines), the expected $\frac{1}{2}\chi^2$ distribution is recovered due to perturbations of f_b induced by the nuisance parameter ϵ.

The level of allowed perturbations, moderated by ϵ, depends on the number of calibration events n_c via the likelihood term in equation 4.10. The usage of the nuisance parameter ϵ leads to a reduction of discovery potential, depending on the calibration size. The loss is present, even in the hypothetical case that the true background pdf is known. This is shown in the left panel of figure 4.6 by the median discovery potential computed for several different calibration sizes using only the true pdfs. Also here, a total of 15 signal and 100 background events are simulated, where the total number of events is Poisson distributed. The red line is computed with the conventional likelihood function which is independent of the calibration size n_c if the true pdfs are used. However, when using the nuisance parameter ϵ, a decreasing calibration sample size results in a reduced discovery potential. Only in the asymptotic limit of high statistics, the values of ϵ approach zero and the theoretical discovery potential is approached. This effect is illustrated by the right panel of figure 4.6 where the distribution of ϵ is shown for 50 (red) and 1000 (blue) calibration events as computed in the left of figure 4.6. The smaller the number of calibration events, the larger values of ϵ are observed. Consequently, larger values of ϵ reduce the number of significant signal events in the analyzed dataset, resulting in the reduction of the discovery potential. As a result of the ϵ-correction it is not possible to claim a signal if the calibration dataset does not contain sufficient statistics to constrain the background model.

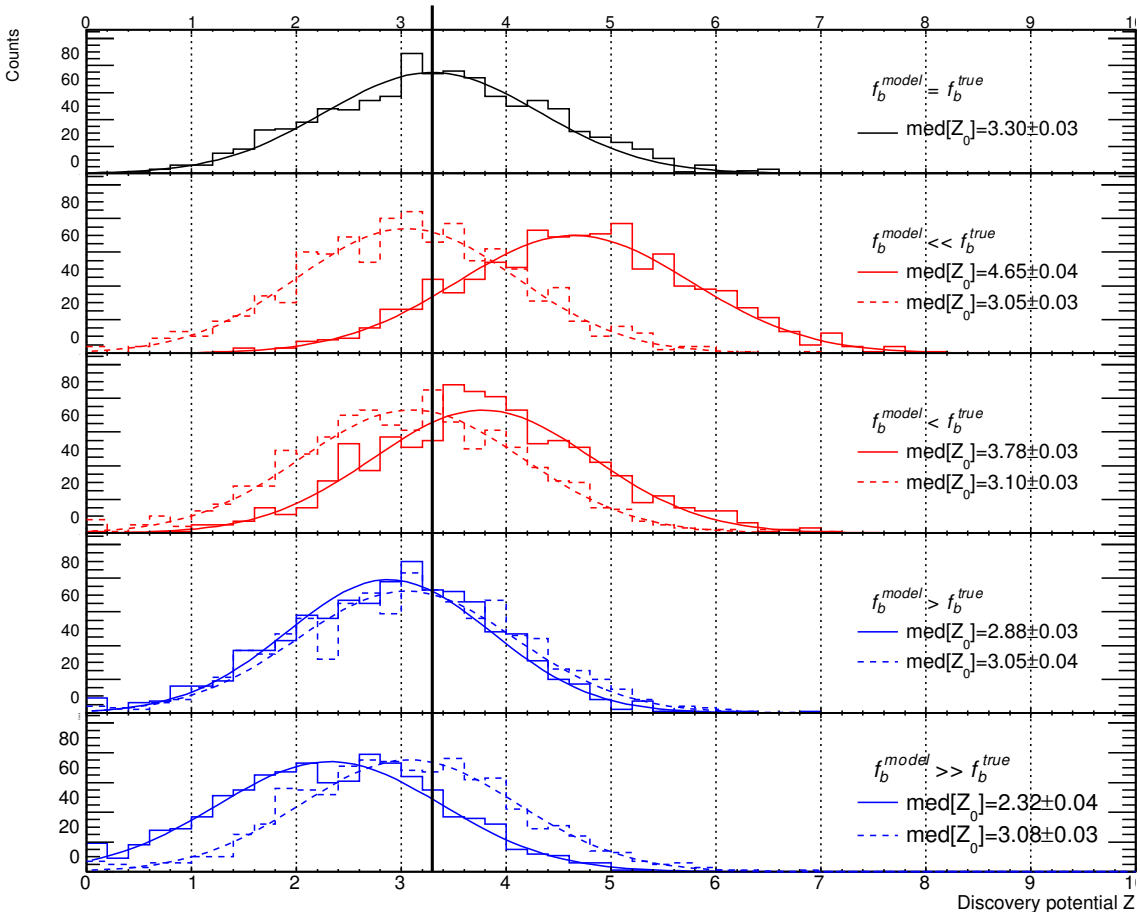

Figure 4.5: The panels show the discovery potential Z for 15 signal events in presence of 100 background events using a likelihood ratio test on Monte Carlo generated event distributions. The top panel (black) uses the true pdf for f_b and, hence, shows the optimal distribution of the discovery potential . The two red and blue panels illustrate the distribution in case of under- and over estimation of f_b. The solid lines are calculation with the conventional likelihood ratio, whereas the dashed lines are determined with the modified likelihood approach explained in this chapter. Figure from [128].

4.3.2 Exclusion tests

A second test of the proposed method is to exclude the presence of a signal at a defined confidence level (CL). For this analysis, 100 background events are randomly distributed according to f_b and the number of signal events corresponding to a 90 % CL is calculated for each of the 10^4 simulated datasets. Similarly to the previous section, the influence of an over and under-estimated background pdf is analyzed by using the pdfs in the two different likelihood functions. Results for a 90 % CL are shown in figure 4.7. To illustrate the impact, only the two extreme examples are shown. The conventional likelihood approach using the biased background pdfs results in an either enhanced or reduced exclusion limit, indicated by the difference between the black and red dashed lines. The ϵ-correction successfully restores the expected distribution.

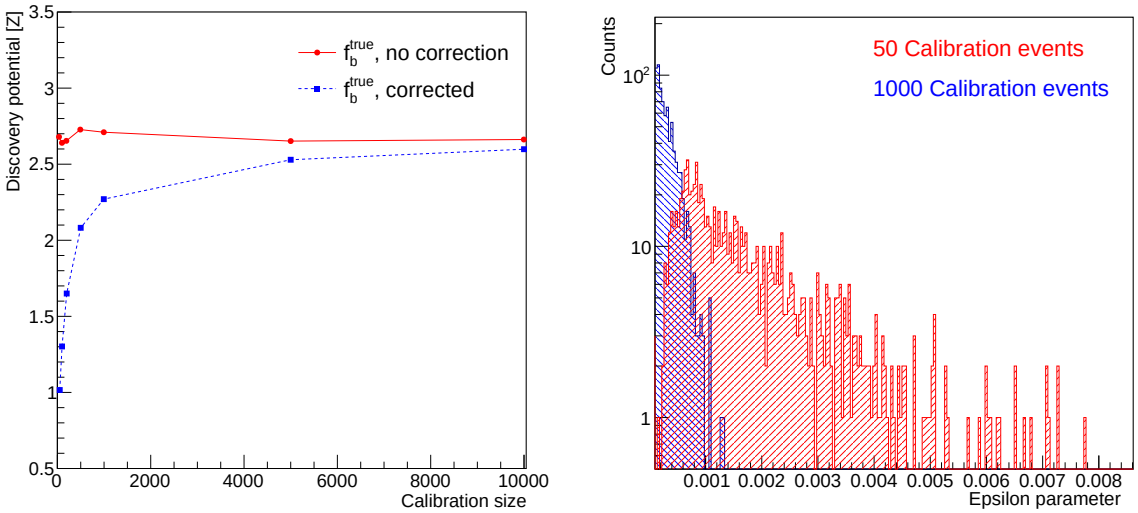

Figure 4.6: (Left) Derived discovery potential for 15 signal and 100 background events as a function of the calibration size, using the conventional likelihood formalism (red) and the proposed $\epsilon-$correction (blue). For this calculation the true background and signal pdfs are used to avoid the influence of a biased background pdf. By using the proposed $\epsilon-$correction, the discovery potential is reduced for small calibration sizes. (Right) Distribution of ϵ parameters evaluated with a calibration size of 50 (red) and 1000 (blue) calibration events.

In summary, the examples shown in figures 4.5 and 4.7 illustrate a possible bias of the PL method if uncertainties are neglected. The benefit of the ϵ-correction resolves a bias of the likelihood ratio without any assumption on the modeling errors of the background model.

4.4 Non-parametric statistical interference

In this section, the non-parametric kernel density estimate of the background pdf of section 4.2 is combined with the ϵ-correction of section 4.3. The KDE background pdf aims to solve the problem of an unknown functional form of the true f_b which is calculated from a calibration data sample with limited statistics. Furthermore, the KDE exploits the maximal information from data due to the unbinned approach. Shape uncertainties originating from the density estimate are propagated to the likelihood function by the ϵ-correction defined in section 4.3. The applicability of the proposed method is tested as a function of the number of events contained in the calibration dataset. The less information in the control sample, the more uncertain the pdf estimation and uncertainties have then to be modeled by the introduced background perturbation parameter ϵ. In the limit of infinite statistics in the control sample, the KDE should approach the true pdf and $\epsilon \to 0$.

As an example, a two dimensional signal (red) and background (blue) models are

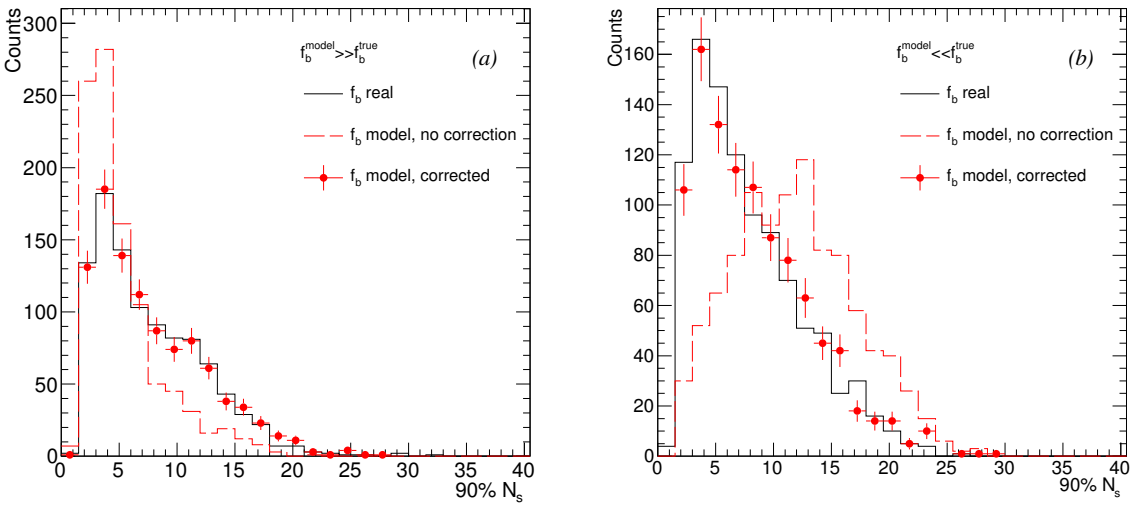

Figure 4.7: Exclusion limits for N_s at 90 % CL by using the true (black line) f_b and over- (left) or under- (right) estimated model. Results calculated by the conventional PL method are shown by the dashed lines and show significant deviations to the expected distribution. However, if the ϵ correction is introduced to the likelihood function (red points), shape uncertainties of the background model are correctly accounted for. Figure from [128].

shown in figure 4.8. The background model features a long tail to low values of y to mimic rare background events. Following the procedure of section 4.1, the generated science dataset contains either 0 or 15 signal events in presence of 100 background events. The KDE background model is derived from a calibration dataset with a varying number of simulated events n_c to test the performance of the method. The results of the PL analysis are shown in figure 4.9. The left panel indicates the false discovery rate of an hypothetical measurement with respect to the total number of events contained in the calibration dataset. For large calibration sizes ($\approx$ 500 events) the derived f_b by the KDE method is sufficient to estimate the background pdf and the false discovery rate is approximately 0, even without a modification of the likelihood function (red markers). For smaller calibration sizes, the false discovery rate increases up to 32 % of the trials due to an insufficient accuracy of the estimated background pdf. By perturbing f_b with f_s and ϵ the false discovery rate is less than 1 %, indicating a correct consideration of the shape uncertainties. As a consequence, the discovery potential is reduced (right panel of figure 4.9) in comparison to the optimal potential (gray area) if the calibration sample is small (blue markers). The optimum potential is given by using the true background pdf and the conventional likelihood ratio. In particular, the small number of calibration events leads to a bias of the median and large variation the discovery potential due to underestimated background pdfs (red points), which is compensated by ϵ. The absolute loss of discovery potential without a bias of the underestimated background model is given by figure 4.6. As a consequence, a stronger measured signal is necessary if the background estimate is based on insufficient data.

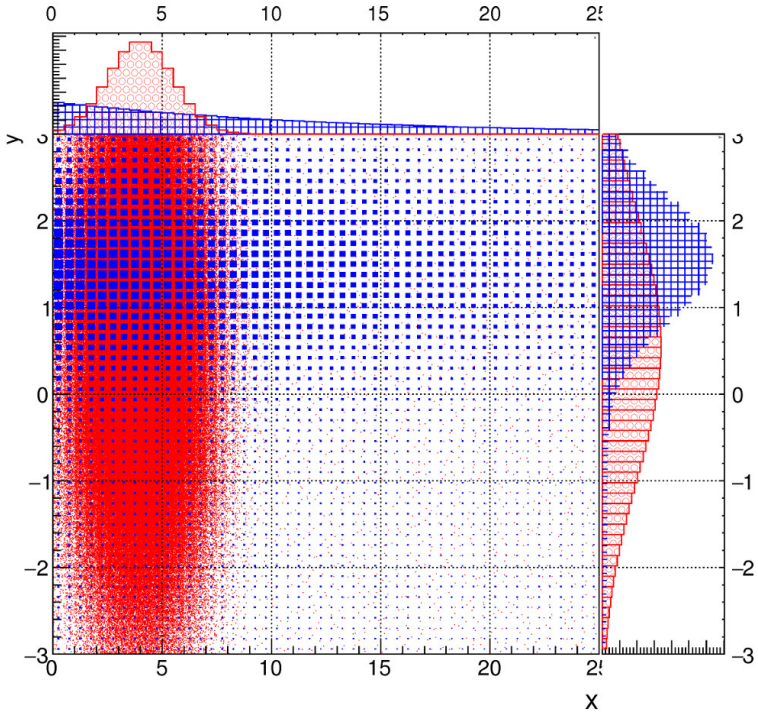

Figure 4.8: Example of a two dimensional signal model (red) in presence of background contamination (blue). The x and y axes illustrate two observables of a hypothetical experiment. Figure published in [128].

By increasing the calibration size, the expected discovery potential is asymptotically approached.

4.5 XENON100 ϵ-corrected results in the minimal velocity parameter space

An application of the proposed ϵ-correction is presented in this section for XENON100 science run II data (see chapter 3) featuring 225 live days. A simplified likelihood ratio analysis is performed with the conventional as well as the ϵ-corrected likelihood function, allowing for a comparison of the two approaches. An adaptive multivariate KDE method is used to calculate the ER background pdf which replaces the parametric fit as used in section 3.4 and [106][89][85]. In addition, the signal model is modified to remove the dependency on astrophysical parameters which reduces the systematic uncertainties contained in the derived limits of chapter 3 (more details can be found in section 1.6 and [86]).

4.5.1 The signal model in terms of v_{min}

The rate equation which is used to derive results in the minimal velocity parameter space is introduced in section 1.6, but the relevant equations are recapitulated below.

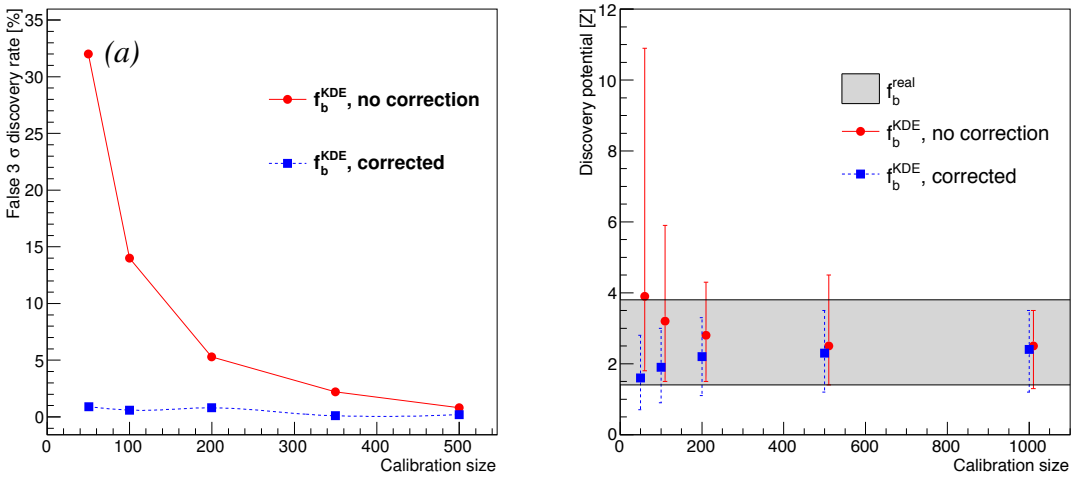

Figure 4.9: Results of a likelihood ratio analysis of simulated data using the signal and background pdfs as shown in figure 4.8. The background contribution is fixed to 100 events. (Left) False discovery rate with a significance above 3σ in absence of a signal for different calibration dataset sizes. Results of the conventional PL analysis using a background model estimated by KDE is shown by the red markers. The blue markers are calculated by the modified likelihood function. (Right) Discovery potential of 15 signal events as a function of the calibration size. Again red (blue) markers display results of the conventional (modified) PL approach. Figure published in [128].

By defining the parameter η as in equation 1.13

$$\eta = \frac{\rho_0 \cdot \sigma_p}{m_\chi} \cdot \int_{v_{min}} \frac{f(\mathbf{v}, t)}{v} \mathrm{d}^3 v, \tag{4.13}$$

all astrophysical assumptions are subsumed in a single parameter and the rate equation of equation 1.12 simplifies to

$$\frac{dR}{dE}(v_{min}) = \frac{1}{2\mu_p^2} \cdot \eta(v_{min}) \cdot A^2 \cdot F^2(v_{min}). \tag{4.14}$$

Here all explicit dependencies on the recoil energies are mapped to the minimal velocity v_{min} defined by

$$v_{min} = \sqrt{\frac{m_A E}{2\mu_A^2}}. \tag{4.15}$$

Furthermore, the explicit dependency of η on the velocity v_{min} can be removed by exploiting the monotonicity of the dark matter velocity integral [61],

$$\eta(v_{min}) \geq \eta(\hat{v}_{min}) \Theta(\hat{v}_{min} - v_{min}). \tag{4.16}$$

The approximation includes the Heaviside step function Θ and, as a consequence, η depends on a fixed velocity $\hat{v}_{min}$. Finally the signal pdf f_s is defined by

$$f_s = \frac{\frac{dR}{dE}(v_{min})}{\int_0^{\hat{v}_{min}} \frac{dR}{dE}(v_{min})}. \tag{4.17}$$

The left panel of figure 4.10 shows the derived signal model computed in terms of the detector parameters cS1 and $cS2_b$ for science run II, following the method and notation of section 3.3. For simplicity, the energy threshold is applied in cS1 at 3 PE, and the analysis is performed without the light collection efficiency dependency introduced in chapter 3. The color coded scale indicates the scattering rate for a 9 GeV/c^2 WIMP

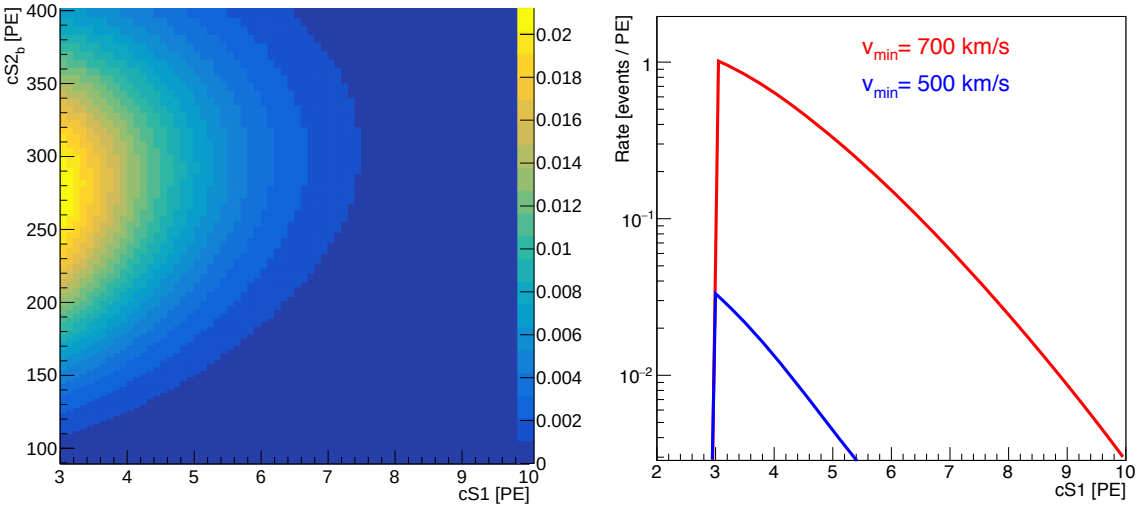

Figure 4.10: (Left) Signal model as a function for cS1 and $cS2_b$ for a 9 GeV/c^2 WIMP in the minimal velocity parameter space for a fixed minimal velocity of 700 km/s. The color coded scale indicates the expected rate for a specific value of η. (Right) Projections of the signal model for a minimal velocity of 500 km/s (blue line) and 700 km (red line) projected in cS1. For more information see text.

mass with an assumed minimal velocity of 700 km/s. For comparison, a signal model for a 50 GeV/c^2 WIMP mass is shown in figure 4.14. The right panel of figure 4.10 shows the difference of expected rates for varying velocities projected in cS1. The blue (red) line indicates a signal model with a minimal velocity of 500 km/s (700 km/s), corresponding to a maximal energy deposition of 3.2 keV (6.3 keV) as given by equation 4.15. These recoil energies are below the applied constant energy threshold of 6.6 keV, hence, the observed rates are caused by fluctuations of the scintillation signal, as explained in section 3.3. It is worth mentioning that the illustration of the event rate of a 700 km/s minimal velocity exceeds the maximal allowed escape velocity of 608 km/s [114] for gravitationally bound dark matter particles.

4.5.2 Adaptive KDE background model for XENON100

The ER background model for science run II (see section 3.4) is estimated from ^{232}Th and ^{60}Co calibration data [84]. An adaptive Gaussian kernel function is used here to particularly account for rare anomalous leakage events. Furthermore, a multivariate kernel in two dimensions is necessary to model f_b in terms of cS1 and $cS2_b$. Following

equation 4.7 the KDE function for XENON100 reads,

$$\hat{f}_0(\vec{x}) = \frac{1}{N}\sum_{i=1}^{N}\left[h_{S1,i}\cdot h_{S2,i}\cdot K\left(\frac{x_{S1}-x_{i,S1}}{h_{S1,i}}\right)\cdot K\left(\frac{x_{S2}-x_{i,S2}}{h_{S2,i}}\right)\right] \tag{4.18}$$

with

$$h_{S1,S2;i} = N^{-1/6}\left(\frac{\sigma_{S1,S2}}{\sigma}\right) f^{(-1/2)}(x_{S1,S2;i}). \tag{4.19}$$

This method allows for an estimation of the background pdf in both observables (cS1, $cS2_b$) based on calibration data without the limitation of a certain choice of a parameterisation. The method will adapt the bandwidth in different regions with higher and lower density. The derived shape of the ER background pdf for science run II is shown in figure 4.11. For comparison, projections in cS1 and $cS2_b$ are shown in figure 4.12 for the two dimensional KDE estimate (red line) as well as the conventional XENON100 method for Gaussian and anomalous leakage contribution (blue line) (see section 3.4). The left panel shows the projected pdfs as a function of cS1. The blue line illustrates the parametric fit to the data in bins of 1 PE, resulting in an unphysical non-differentiable background pdf. The KDE pdf, however, shows a smooth and differentiable pdf. In the $cS2_b$ parameter both pdfs show a similar shape. The residuals of the two background models are shown in figure 4.13 for cS1 and $cS2_b$ in the left and right panel, respectively. Both methods show only small differences at values above ∼5 PE in cS1 and ∼1000 PE in $cS2_b$. In particular, around 300 PE in $cS2_b$, the KDE predicts a larger background due to a discontinuous modeling of the anomalous leakage component in the XENON100 background pdf (see section 3.4). The adaptive KDE estimate below 5 PE in cS1 shows systematic lower probabilities in comparison, indicating an influence of the 3 PE threshold of the method. This might be solved by

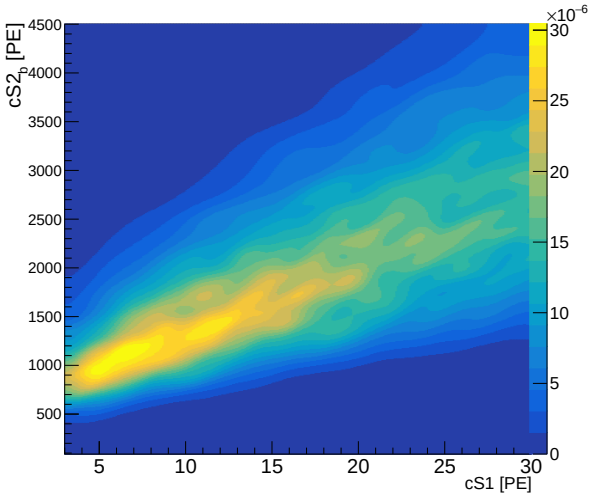

Figure 4.11: The color coded scale indicates the ER background probability in terms of the detector parameters cS1 and $cS2_b$. The pdf is calculated by the multivariate adaptive KDE using a Gaussian kernel function.

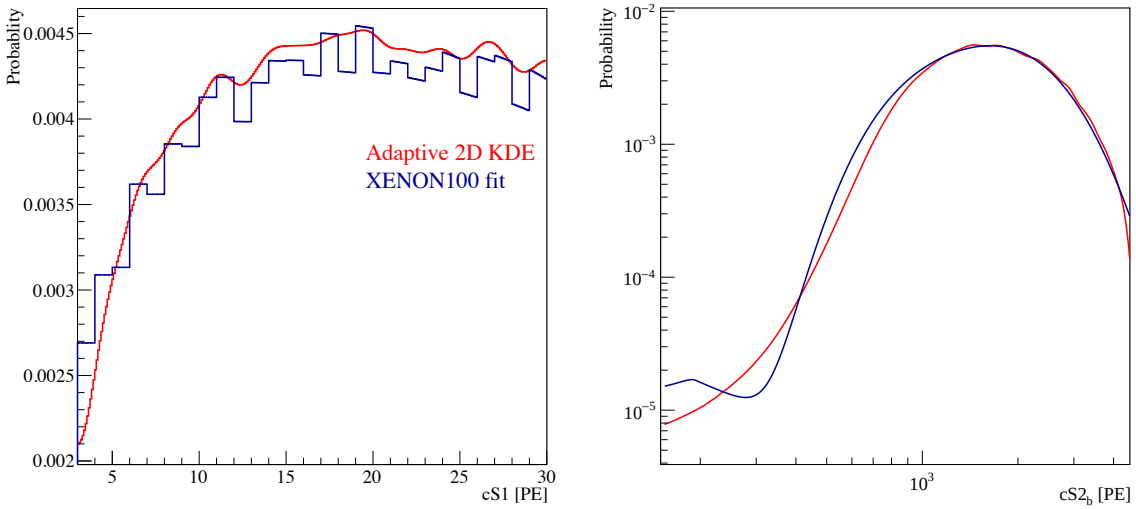

Figure 4.12: Projections of the XENON100 ER background pdfs with respect to detector parameters cS1 (left) and cS2$_b$ (right). The blue line indicates the XENON100 parametric fit while the red line shows the result of an adaptive two dimensional kernel.

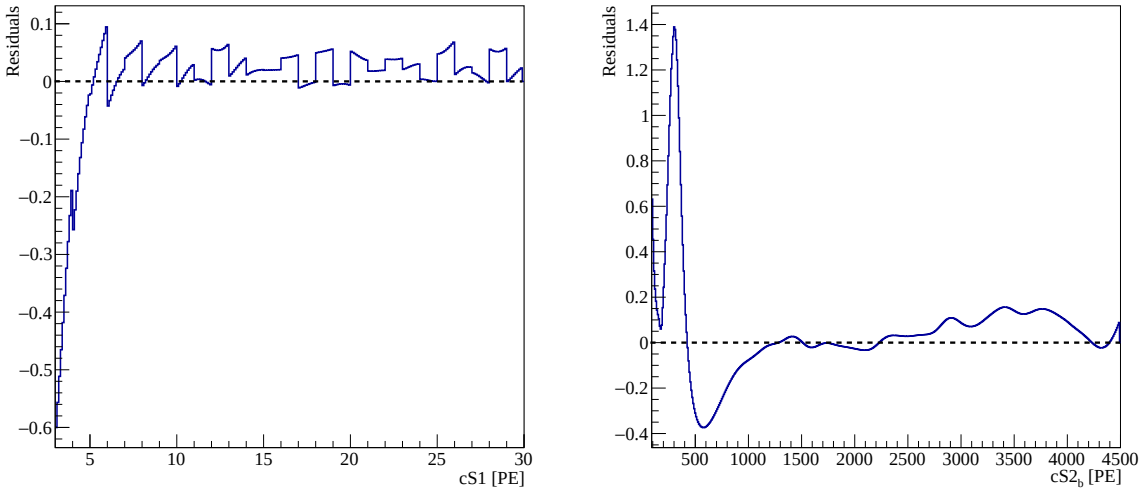

Figure 4.13: Residuals of the two pdfs as shown in figure 4.12 for a projection in cS1 (left) and cS2$_b$ (right).

applying the 3 PE threshold to the background model directly instead of a cut to the calibration data.

4.5.3 Profile likelihood ratio test

In this section, the applicability of the ϵ-corrected likelihood function combined with the model independent KDE background model applied to XENON100 is shown for science

run II data [85]. The background and 50 GeV/c^2 signal pdfs are shown in figure 4.14 in the left and right panel, respectively. In addition, the signal sizes measured in terms of cS1 and cS2$_b$ of events acquired in science run II are shown by black markers. By using

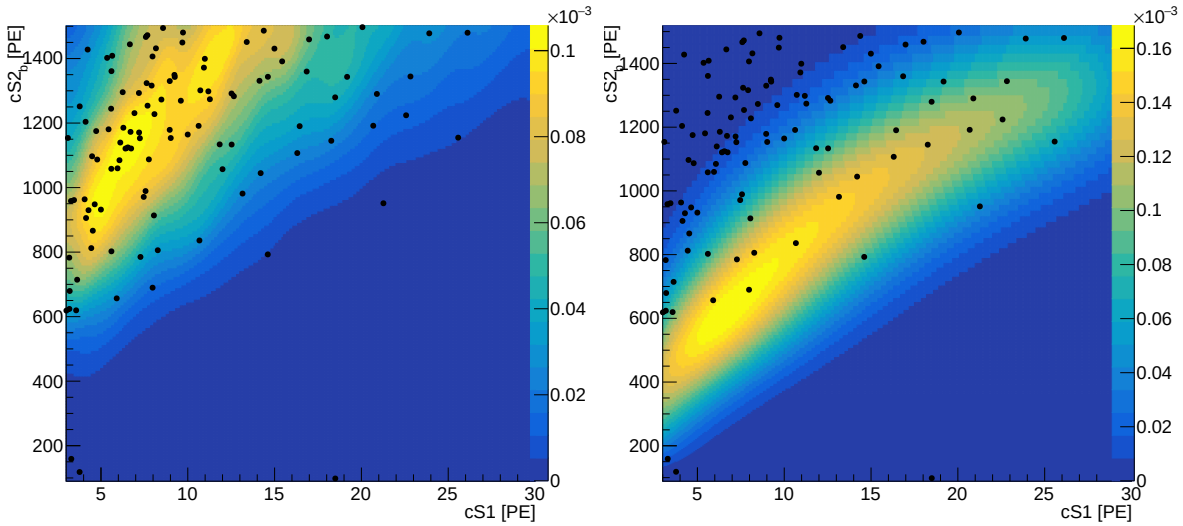

Figure 4.14: (Left) Two-dimensional adaptive kernel density estimate of the ER background (color coded scale) in science run II. Black markers show the final event selection of the dark matter data in science run II. (Right) The color coded scale indicates the signal pdf in the v_{min} space for a 50 GeV/c^2 WIMP. Black markers indicate science run II data.

the proposed ϵ-correction, it is possible to exploit the full parameter space without the necessity of defining bands based on the signal shape as shown in section 3.3.

The cross-check of the method is performed with a likelihood ratio test as discussed in section 1.7. The signal pdf is derived in the minimal velocity parameter space for a 9 GeV/c^2 WIMP mass and the background shape is given by the pdf as shown in figure 4.11. A calculation of the likelihood ratio while profiling in N_s for a 9 GeV/c^2 WIMP model results in the likelihood curves as shown in figure 4.15. The blue line indicates the result of the conventional likelihood ratio and for the calculation of the red line, the newly proposed correction is applied by using the ϵ-correction, constrained by the ER background, for the XENON100 science run II. The correction results in a reduced likelihood value at $N_s = 0$ which indicates the correct modeling of the uncertainties in the background model. Due to the absence of further nuisance parameters accounting for uncertainties in f_b and f_s (see section 3.5) in this example, the conventional method would result in a detection of 2 events. At larger values for N_s both methods give equal results. Hence, the computation of a one sided confidence level (CL) (or exclusion limit) on the number of estimated signal events at likelihood values of 2.71, corresponding to a 90 %CL assuming a χ-squared distribution of the test statistic [70], shows no difference in calculated limits.

The ϵ procedure is applied, as an example, for the pdfs of a 7 GeV/c^2 and 9 GeV/c^2 WIMP mass and several values of v_{min}. The likelihood curves allow to compute limits

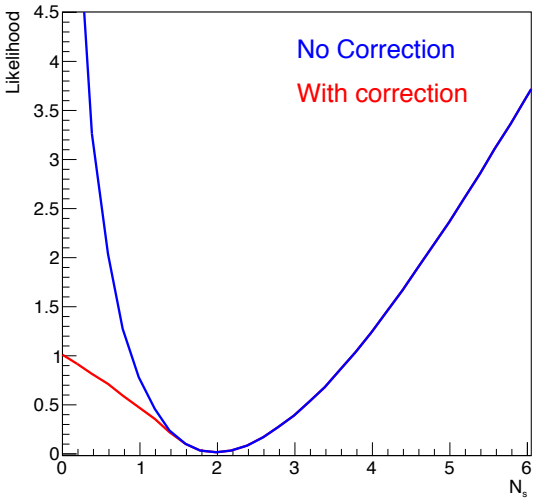

Figure 4.15: Minimized likelihood values computed as a function of the number of signal events for a 9 GeV/c^2 WIMP mass and a v_{min} of 550 km/s. The blue (red) lines show results from the conventional (modified) likelihood function.

on η at a 90 % CL which are shown in figure 4.16 for a 7 GeV/c^2 WIMP mass in the left panel and for 9 GeV/c^2 in the right. For simplicity, only N_b and ϵ are used as nuisance parameters. As a reference, the CDMS-II-Si results for three v_{vmin} intervals are added, which are taken from [139]. It can be seen, that the XENON100 result cannot fully exclude the CDMS-II-Si signal for the lowest velocity interval. These calculated exclusion limits for XENON100 are, in principle, more robust than derived by the conventional method in terms of the cross-section and WIMP mass, since systematic uncertainties from astrophysical parameters are removed due to the v_{vmin} method as well as uncertainties of the background model are profiled out by ϵ.

4.6 Discussion

In this chapter, a possible solution is presented to improve the XENON100 analysis. Due to a missing method to correctly model the shape uncertainties contained in background model of XENON100, the parameter space is artificial binned in terms of cS1 and cS2$_b$. These, so-called bands, allow to define a statistical uncertainty, but lead to a reduction of the exploited parameter space of the signal model within the bands. It is shown that a biased estimation of the background model without a correct parameterisation of the uncertainties, results in an over or under-coverage of the confidence level calculated by a profile likelihood analysis.

The solution is twofold. First of all, an adaptive multivariate kernel density estimate is used to derive the background model based on a calibration data sample. The KDE method is, by construction, non-parametric and, hence, model independent. An adaptive kernel naturally accounts for a varying density in the control sample, especially important if rare event signatures of unknown origin cannot be calibrated with

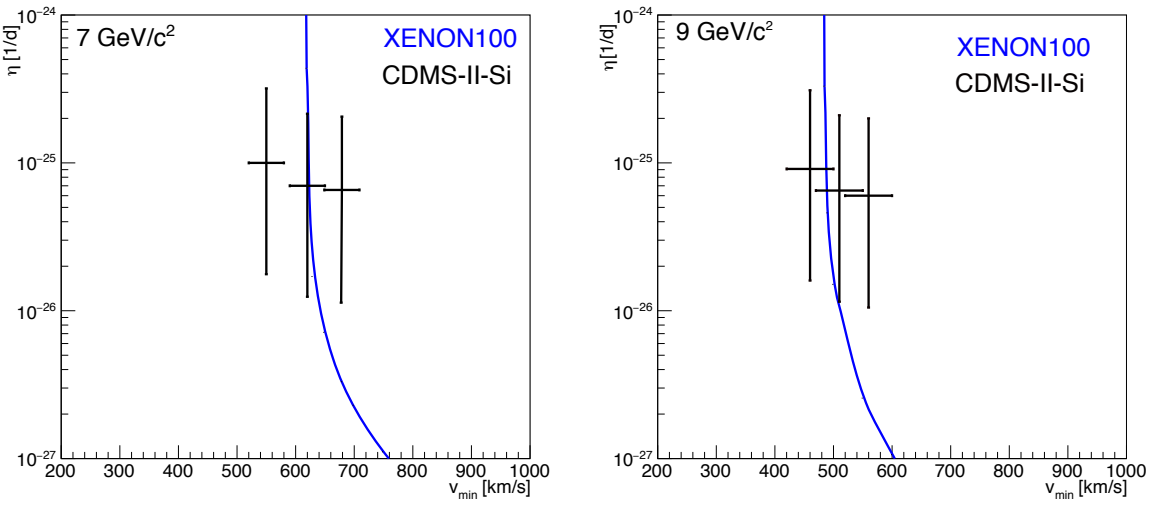

Figure 4.16: The left (right) panel shows the results of a $7\,\mathrm{GeV/c^2}$ ($9\,\mathrm{GeV/c^2}$) WIMP mass expressed in the minimal velocity parameter space. The derived limit for XENON100 science run II is shown in blue and derived values, taken from [139], for the CDMS-II-Si signal is illustrated in black.

sufficient statistics. Secondly, a modified likelihood function allows to consider shape uncertainties in the background pdf without the need to identify nuisance parameters of the background model. The method itself introduces a new nuisance parameter ϵ, which is independent of the background model and accounts for the shape uncertainties of the estimated pdf. This is achieved by anti-correlating the signal and background pdf via ϵ. In this way, a biased estimation of the background pdf due to low statistics in the calibration data can be compensated for. In addition, the ϵ parameter is constrained by the likelihood calculated from the calibration dataset. This results in a negligible effect of ϵ in case of sufficient statistics in calibration dataset leading to a robust background model. It reduces, however, signal-like fluctuations in the science data in case of a poor knowledge of the background model. As a result, the false discovery rate of Monte-Carlo-generated tests is less than 1 %, indicating a correct modeling of uncertainties in the background model. Furthermore, it is shown that the protection against a false discovery results in the reduction of the discovery potential in presence of a signal for small calibration datasets. Only for sufficiently large calibration datasets the theoretical possible discovery potential is recovered. In conclusion, this new method allows to model shape uncertainties of a non-parametric pdf by means of a profile likelihood analysis. In future the adaptive KDE background estimate might be optimized by maximizing the likelihood for different values of the smoothing parameter ρ.

Finally the new method is applied, for the first time, to data from XENON100 science run II. The adaptive KDE background pdf results in a comparable shape to the previously used ER background model. While the KDE shows less systematic uncertainties in the modeling of anomalous leakage events, the density estimation can be

improved by removing artificial boundaries in the calibration dataset. In particular, the S1 threshold should not be applied to the calibration data, but directly to the background pdf to avoid a bias of the KDE in vicinity of a boundary. A new signal model is derived to present XENON100 exclusion limits independent of astrophysical parameters which leads not only to a reduction of systematic uncertainties in calculated results but also improves the comparability of different experiments. The chapter is concluded with a simplified profile likelihood analysis of the XENON100 data with the conventional as well as the modified approach. The analysis exploits the signal model in terms of cS1 and $cS2_b$ without the necessity of binning or banding the signal parameter space due to uncertainties in the background mode. The ϵ parameter successfully accounts for all shape uncertainties in the background model, by reducing the sensitivity of the detector. An improved analysis in terms of v_{min} should be performed on the uncorrected parameters S1 and $S2_b$ as well as account for shape uncertainties in the energy scales and cut acceptances. In addition, the KDE ER-background model should be extended by adding the smaller contributions of the AC and NR components as performed in chapter 3. This chapter shows for the first time the application of the ϵ-correction for XENON100 science data combined with a novel non-parametric approach to estimate the ER background and presents exclusion limits derived by a profile likelihood analysis in a parameter space free of astrophysical assumptions.

Chapter 5

Light detection in XENON1T

To observe particle interactions inside the XENON1T TPC it is essential to efficiently detect photons created by scintillation and electroluminescence processes. Two arrays of photomultiplier tubes (PMT) at the top and bottom of the detector are equipped with a total of 248 Hamamatsu 3" R11410-21 light sensors (see section 2.3.2). To reduce the risk of failures during the detector operation and verify their specified performance, all PMTs have been tested prior to their final assembly. These tests are performed with a special focus on equal test conditions for each PMT to derive comparable parameters of their performance. In this chapter, general properties of the Hamamatsu R11410-21 PMT are introduced in section 5.1. The test facilities are described in section 5.2 and results are summarized in section 5.3. Furthermore, the construction of the two XENON1T PMT arrays is summarized in section 5.4 and the performance of the tubes during the first year of operation is presented in section 5.5. The structure and content of sections 5.2 and 5.3 follow the publication [140] of which the author of this thesis is a corresponding author.

5.1 Hamamatsu R11410-21 tube

It is important to optimize the light sensors for the detection of the small number of photons generated by particle recoils in liquid xenon by depositing energies of only a few keV. First of all, such a device must be able to detect light at the level of single photons featuring a wavelength of 178 nm [79]. Furthermore, the device must operate stably at time scales of several years inside liquid xenon at a cryogenic temperature of $-100\,^{\circ}\mathrm{C}$. In addition, all parts of the photosensor should comply with the ultra low radioactivity levels required of all materials in the vicinity of the dark matter target. Those requirements are only fulfilled by photomultiplier tubes produced by Hamamatsu Photonics, in particular, the R11410-21 model, which features a circular quartz window of 3" in diameter (see left picture in figure 5.13). An illustration of the inner parts of the photosensor is shown in the right panel of figure 5.13. A xenon vacuum ultraviolet (VUV) photon (see section 2.2) interacts, by the photoelectric effect, with the photocathode *(1)* and produces an electron (photoelectron). To enhance this process, the selection of the material of the photocathode is optimized for the 178 nm xenon light by using a certain bialkali alloy to maximize the production efficiency of

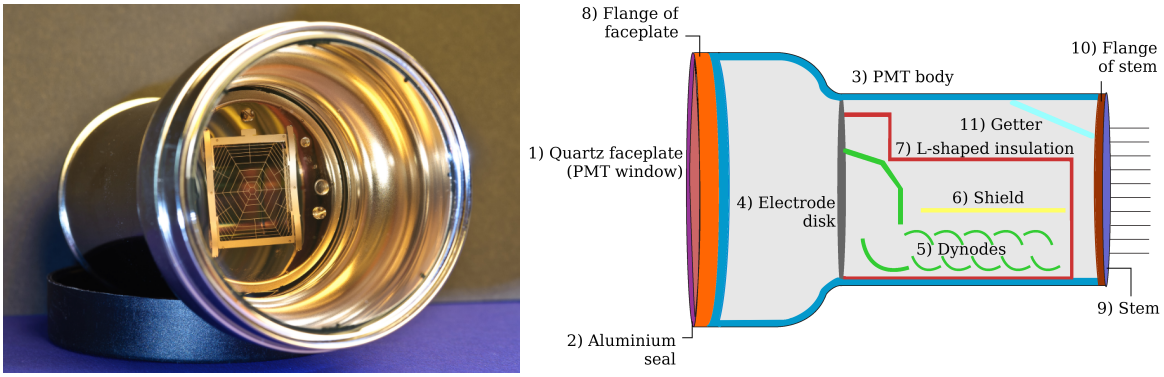

Figure 5.1: (Left) Picture of a Hamamatsu 3" R11410-21 PMT. (Right) Illustration of the components of the Hamamatsu R11410-21 photomultiplier tube (PMT). Right figure from [141].

photoelectrons (PE). The probability to produce a PE from an incident VUV photon is denoted as the quantum efficiency (QE) stated at a particular wavelength. An applied electric field inside the tube focuses the created photoelectrons through an electrode disc *(4)* to a chain of 12 dynodes *(5)* which amplify the initial PEs to a measurable voltage at the anode. The probability of the electron multiplication mechanism is quantified by the collection efficiency (CE). The amplification factor for photoelectrons is in the range of $10^5 - 10^7$ and stated as the gain with respect to an applied voltage.

The extensive procedure of optimizing the material selection to manufacture the tube is summarized in [141]. Each component is individually screened for its intrinsic radioactivity, measured by high-purity germanium detectors [142, 143, 144, 145]. As a result, the average radioactivity level of all PMTs is reduced to less than 13 mBq/PMT for ^{238}U, 0.4 (0.1) mBq/PMT for ^{228}Th and 12 (2) mBq/PMT for ^{40}K [141]. A Monte Carlo simulation of the expected background in XENON1T [98] estimated that the PMTs contribute only 4 % to the radiogenic neutron background. The electronic recoil background is enhanced due to the PMTs by 7 % [98] in part by contributing to the ^{222}Rn budget and to the natural radioactivity of surrounding materials (see section 2.1). As a result, the improved PMT for XENON1T contributes significantly less to the background in comparison to XENON100, where PMTs account for 65 % of the total ER [96] and 21 % of the radiogenic NR [97] background.

First performance studies of earlier versions of the R11410 phototube are reported in [146][147]. Results of the operation of the tube in gaseous and liquid xenon are reported by PandaX [148], NEXT [149] and RED [150][151] collaborations. A similar tube developed for the operation in liquid argon is reported by DarkSide [152] and GERDA [153]. The usage of 37 R11410-MOD PMTs inside the dual-phase TPC of the PandaX experiment is shown in [154]. Also next generation experiments, for example LZ [108], will operate this PMT model. The widespread use of this tube becomes evident and the following detailed performance study of the various PMT parameters for a total of 321 tubes is the most extensive study to this date.

5.2 PMT test facilities

In total, three different facilities were used to test the tubes. While two facilities are located at the Max-Planck-Institut für Kernphysik and are optimized to test all 321 PMTs, a third facility operated at the University of Zurich is designed for long term stability tests for a selection of tubes ($\sim 15\,\%$). The first facility in use to measure parameters at room temperature is able to test up to 12 PMTs simultaneously. Each slot is equipped with a high voltage power supply, signal cable and a light guide allowing for a LED calibration at 380 nm [155]. The LED has a particular narrow pulse width of ~ 1.4 ns which allows to quantify precisely the timing differences of the tubes. The second facility, also able to test 12 PMTs in parallel, allows to operate the tubes at cryogenic temperatures and its design is sketched in figure 5.2. Two PMTs arrays,

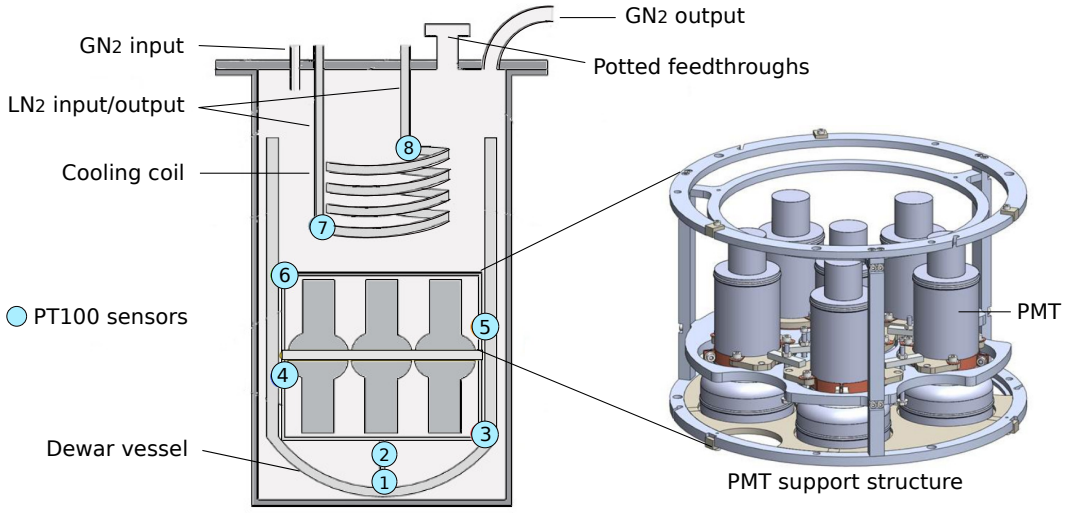

Figure 5.2: PMT test facility to operate and test PMTs at cryogenic temperatures ($-100\,°C$). Two structures equipped with up to 6 PMTs each can be installed inside a Dewar while always pairs of PMT windows face each other. In total 8 PT100 thermometers at various positions measure the temperature inside the Dewar and allow to stabilize the inner temperature by manually regulating the flux of the nitrogen through the coil. Figure from [140].

each equipped with 6 tubes, are contained in a vessel which can be cooled to cryogenic temperatures of $-100\,°C$ in ambient nitrogen vapor. The relative position of the arrays is designed such that pairs of PMT windows face each other at a distance of 2 cm. By flushing liquid nitrogen through a copper coil at the top of the vessel, the temperature is stabilized at $-100\,°C$ within a few degrees Celsius. Several thermometers, placed at various positions inside the tank, allow a precise measurement of the temperature gradient and time evolution.

Both setups use the same data acquisition (DAQ) to read out the PMT signals. First, the signal is amplified by a factor of 10 and sent to a fan-out. Then the signal is divided to be processed by a charge-to-digital converter (QDC) and the other signal

is further amplified by a factor of 10. Hence, the signal output is amplified by a factor 100 which is sent to a discriminator and is further read out by a scaler and a time-to-digital converter (TDC). The TDC has a maximal time span of 1.2 μs with a time resolution of 0.3 ns. The final outputs of the QDC, TDC, and scaler are recorded by a computer, including the timing information of the LED trigger. Detailed information can be found in [155].

A third setup, located at the University of Zurich (UZH), is used for long term stability tests of the tube in liquid and gaseous xenon. Up to 5 PMTs can be tested in parallel and are usually operated for several weeks, hence, only a selection of PMTs could be tested in this setup. More details can be found in [140][156].

5.3 PMT performance tests

The goal of the extensive test campaign for the total 321 PMTs is twofold. First of all, the measurements aim to quantify the performance of tubes and cross-check the data provided by the producer. With this information 248 PMTs have been selected for XENON1T and tubes which do not fulfill the requirements can be replaced prior to installation with less effort and time delays. And, secondly, the tubes are exposed to thermal stress by at least two thermal cycles between room temperature and $-100\,^{\circ}\mathrm{C}$ to ensure the performance inside the liquid xenon.

5.3.1 Quantum efficiency

A low energy threshold of the XENON1T detector is essential to detect dark matter as shown in section 1.4. As a consequence, the tubes must efficiently detect single photons as only a few percent of the produced photons at the interaction site reach the PMT photocathode. As mentioned before, the probability of converting an incoming photon to a photoelectron is quantified by the quantum efficiency, and values, measured by Hamamatsu, at the xenon wavelength are shown in figure 5.3 for all 321 tested PMTs (red) and the 248 selected PMTs. After rounding, both distributions show a mean of 34.5 % with a standard deviation of 2.8 %. The producer guaranteed a minimal QE of 28 %, but maximal values of more than 40 % were achieved. A measurement of the spatial distribution of the photon detection efficiency (combined QE and CE), values at different locations of the cathode is shown in [157] and proves the homogeneity to a level of (5-10) %. The temperature and wavelength dependence of the QE values are presented in [158] indicating an increase of the QE at cryogenic temperatures by a factor of 1.1 - 1.15 at 175 nm. In addition, the high energetic xenon VUV scintillation light induces a (18-24) % contribution of double photoelectron emission [159] which is not present if the tubes are calibrated with the lower energetic blue LED light. This is an effect of particular relevance for an operation of these PMTs in LXe as shown in [159] and should be considered if the LXe target is used as a calorimeter.

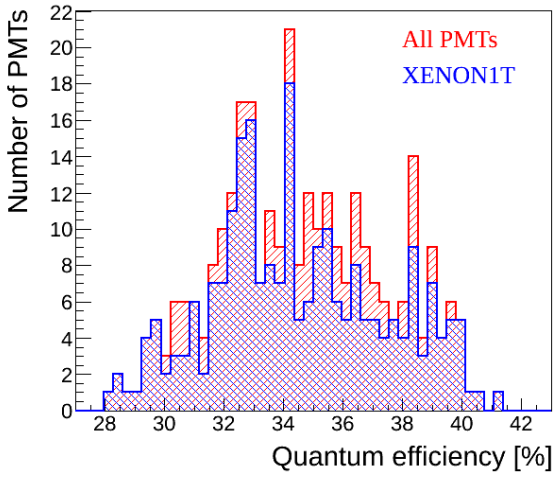

Figure 5.3: The figure shows the quantum efficiency for all tested (red) and the selection of 248 PMTs (blue). The measurements were performed and provided by Hamamatsu. Both distributions show an average of 34.5 % and a standard deviation of 2.8 % after rounding. Figure published in [140].

5.3.2 Gain distribution

The definition of the gain quantifies the PMT response to single photoelectrons and can be derived by a measurement of the charge spectrum induced by a light source. An example for a measurement to determine the gain can be seen in figure 5.4. Noise, generated by the electronics, creates a pedestal in the charge spectrum which is modeled by a Gaussian of amplitude A_0, mean μ_0 and width σ_0 (see equation 5.1) as indicated by the red line in figure 5.4. The measured charge induced by the LED illumination results in the SPE peak and higher PE contributions, as the number of emitted photons follows Poisson statistics. These additional peaks i are also modeled by a Gaussian distribution with A_i, μ_1 and σ_1 (blue lines). The combined fit function (green line) can be written as a function of the measured charge Q as

$$f(Q) = A_0 \exp\left(-\frac{(Q-\mu_0)^2}{2\,\sigma_0^2}\right) + \sum_{i=1}^{N} A_i \exp\left(-\frac{(Q-i\mu_1)^2}{2i\sigma_1^2}\right) + B\exp(-Q\tau). \quad (5.1)$$

To improve the fit between the pedestal and the SPE peak, an empirical exponential function (orange line) is added as suggested in [155][160]. The gain is calculated by $g = \frac{\mu_1}{e}$, with e being the elemental charge. It is worth mentioning that the gain estimation by this fit can also be performed by a model independent method as shown in [161]. The method determines the gain by exploiting the statistical properties of the distribution, in particular, the mean and variance of the single photoelectron peak.

The evaluation of the gain at 1500 V is performed for all tested PMTs with the same LED configuration in order to minimize systematic uncertainties. As a result, the distribution for all tested tubes (red) and the selection (blue) is shown in the right panel of figure 5.4. The mean for all PMTs is 5.4×10^6 with a standard deviation

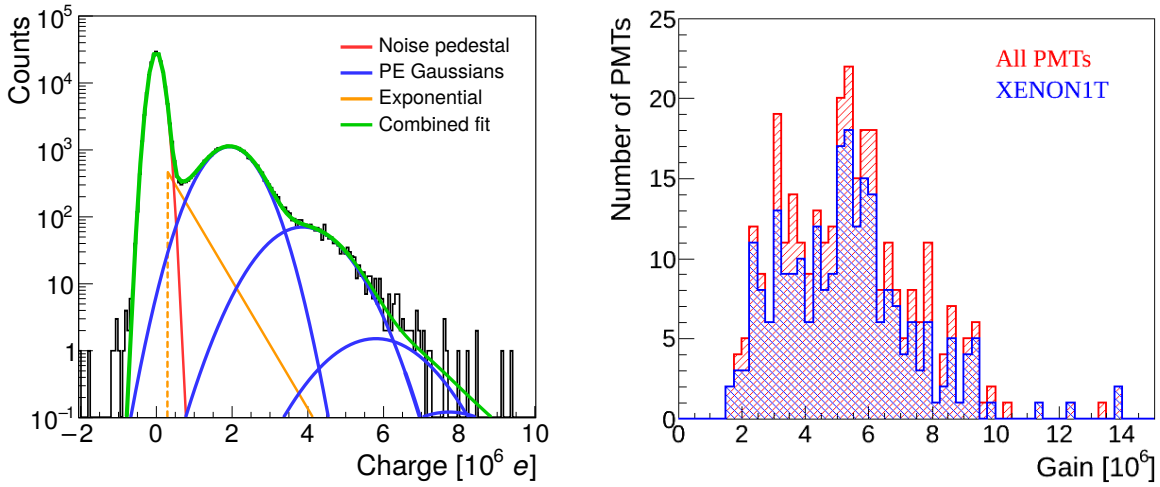

Figure 5.4: (Left) PMT response to a LED calibration inducing single photoelectrons (black). The colored lines indicate the individual components which are fitted to the data. For more information see text. (Right) Derived gains at a common bias voltage of 1500 V for 248 selected (blue) and all 321 tested PMTs (red). An average value for the 248 selected PMTs of 5.3×10^6 with a standard deviation of 2.1×10^6 is derived. For the full sample of tubes a mean of 5.4×10^6 with a standard deviation of 2.1×10^6 is computed. Figures published in [140].

of 2.1×10^6 and the result for those selected tubes for XENON1T is 5.3×10^6 and a standard deviation of 2.1×10^6. Furthermore, the gain is measured at 8 different voltages between 1320 V and 1680 V to enable a parameterisation of the gain values with respect to the applied voltage. This information is used to verify parameters at an equalized gain or, for instance, was used during the commissioning phase of XENON1T when a dedicated calibration of the PMT gain was not yet possible. The final gain-calibration procedure of the XENON1T PMTs should also account for the possibility of a double electron emission caused by xenon VUV light (see section 5.3.1) to avoid a bias of the reconstruction of the deposited energy [159].

None of the PMTs were returned due to a too low gain but a few tubes showed a larger value which is beneficial for the operation.

5.3.3 Single photoelectron resolution and peak-to-valley ratio

To quantify the performance of a PMT by its response to single photons, a fit as shown in equation 5.1 allows to define parameters which describe the level of separation of the pedestal and SPE peak. The resolution of the SPE peak can be computed by $R = \frac{\sigma_1}{\mu_1}$, where σ_1 and μ_1 are given by equation 5.1. In addition, the peak-to-valley ratio is defined as the ratio between the maximal height of the SPE peak and the minimal value of the valley between the peak and the noise pedestal. Both, the SPE resolution and peak-to-valley ratio quantify the separation power between the noise pedestal and SPE response. An optimized performance of PMTs with respect to these parameters

allows, in general, to reduce the trigger threshold of the experiment, enabling a lower energy threshold. The distribution of the computed SPE resolution and peak-to-valley ratio with respect to the gain is shown in the left and right of figure 5.5, respectively. The color coded scale indicates the frequency of computed values of all PMTs, whereas

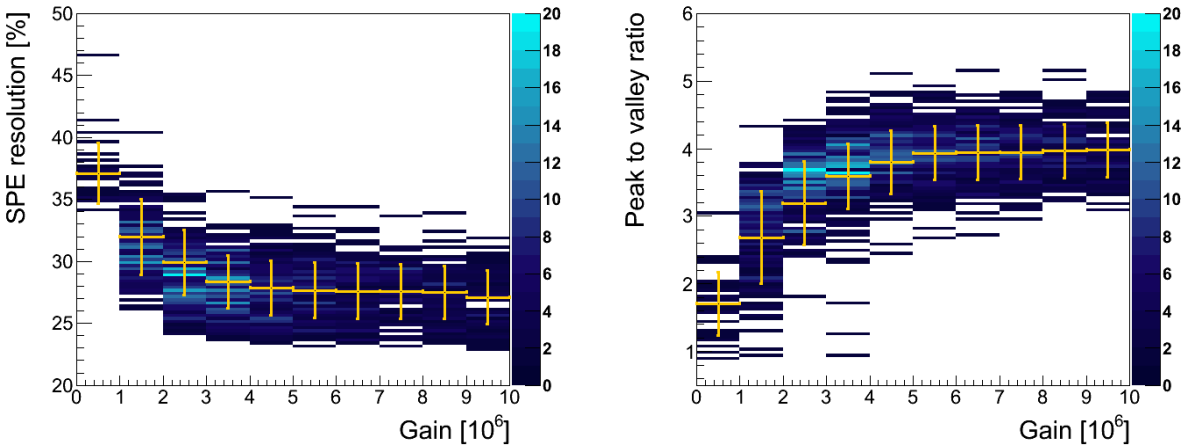

Figure 5.5: (Left) Single photoelectron resolution as a function of gain for the selected PMTs. (Right) Peak-to-valley ratio as a function of gain. The color coded scale displays in both plots the computed values for all PMTs. The yellow markers show for each bin the average values. Figures published in [140].

the mean values for each bin is shown by the yellow markers. The SPE-resolution as well as the peak-to-valley ratio improves if the PMT is operated with a larger gain until it levels off at a gain above $\sim 4 \times 10^6$. However, the higher bias voltage reduces, in general, the stability and lifetime of the tube, thus a compromise is necessary. None of the PMTs showed an exceptional abnormal behavior in these parameters and thus no PMT was rejected by this criterion.

5.3.4 Transit time measurement

The timing performance of the tubes are quantified by the transit time spread (TTS), defined by the distribution of transit times given by the time difference between the LED trigger and arrival time of the photoelectrons. A trigger signal of the LED corresponds, in first order, to the interaction of the photon with the photocathode, whereas the arrival time estimates the appearance of the electron avalanche at the anode. The intrinsic transit time of the tube is difficult to measure as the DAQ contributes significantly to the delay. The spread of arrival times, however, is specific to the PMT and is, therefore, used to quantify the timing performance of the tube. The TTS spectrum is measured by an illumination of the tube with a LED at single photoelectron intensity to ensure that approximately 10 % of the events are caused by SPE signals. If the TTS distribution features a narrow width, the time coincidence window among the PMTs in XENON1T can be chosen smaller, reducing possible random coincidences.

As an example the transit time spectrum for a single PMT signal is shown in figure 5.6 (left). The red line indicates the most probable arrival of the electron avalanche

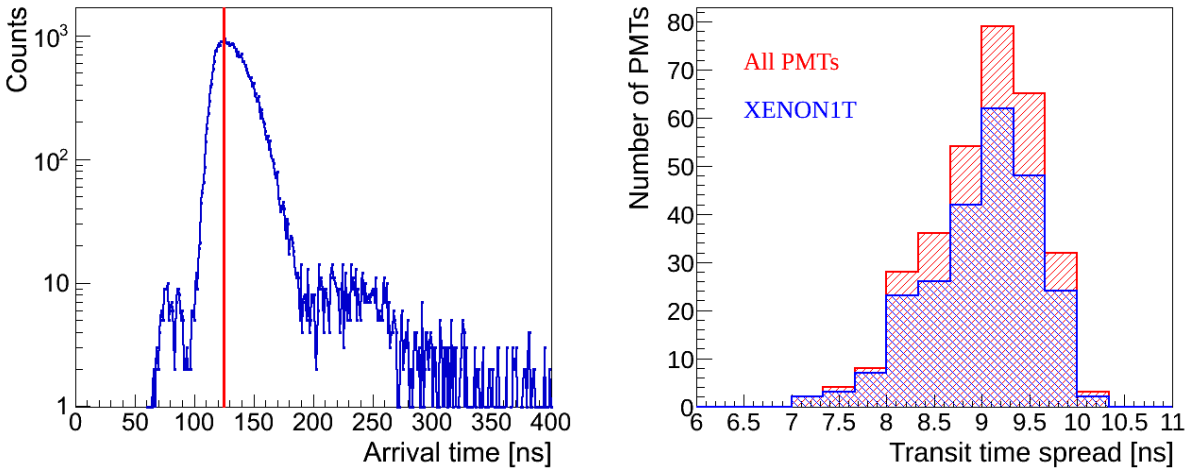

Figure 5.6: (Left) Transit time spectrum for a single PMT signal with the most probable arrival time indicated by the red line. (Right) Distribution of the measured transit time spread values, defined as the FWHM of the main peak, for all tested tubes (red) and XENON1T selection (blue). Figures published in [140].

at the anode which is, in this example, approximately 125 ns after the LED trigger. This time period includes the time delays caused by the DAQ. According to the producer, Hamamatsu, the time delay of the tube itself is around 46 ns. A population before the main peak might be attributed to photons which transmit through the PMT window and interact directly with the first dynode. Events after the main peak are caused, for example, by back-scattered photoelectrons from the first dynode [162].

The width of the main peak is defined by the FWHM and the distribution of TTS values is shown for all (red) tubes and the XENON1T selection (blue) in figure 5.6 (right). The mean of the 248 selected PMTs is (9.2 ± 1.3) ns and must be deconvolved with the 1.4 ns pulse width of the LED, resulting in the TTS for the tubes alone of (9.1 ± 1.3) ns. Hence, the particular narrow LED pulse width has a negligible impact on the presented measurements. These results are in agreement with the TTS of 9 ns reported in the specifications by Hamamatsu. No PMT was returned due to a significant deviation of the TTS value.

5.3.5 Dark count rates

The dark count (DC) rate is defined by the total number of signals per time above a fixed threshold in absence of a light source and is given in units of Hz. At room temperature the DC rate is dominated by thermal electrons emitted by the surfaces from the cathode and dynodes, and is even enhanced due to the choice of materials to reduce the work function [163]. This thermal component is strongly suppressed at cryogenic temperatures when other effects start to dominate. According to the

producer [163] the DC rate at −100 °C is, in part, caused by a leakage current generated between the anode and last dynode as well as by an imperfect insulation between, for instance, the anode pin and other pins. Additionally, electrons can be created by field emission due to the high electric fields applied to the dynode chain. A further contribution of the DC rate is induced by ambient and intrinsic radioactivity as well as cosmic particles. A reduction of all mentioned components is essential for low PMT DC rates during operation which is necessary to minimize the probability of accidental coincidences while 248 PMTs are operated in parallel.

The evolution of the DC rate during a cooling cycle, as described in section 5.2, is shown in figure 5.7 (left). The left plot of figure 5.7 illustrates the time evolution of the

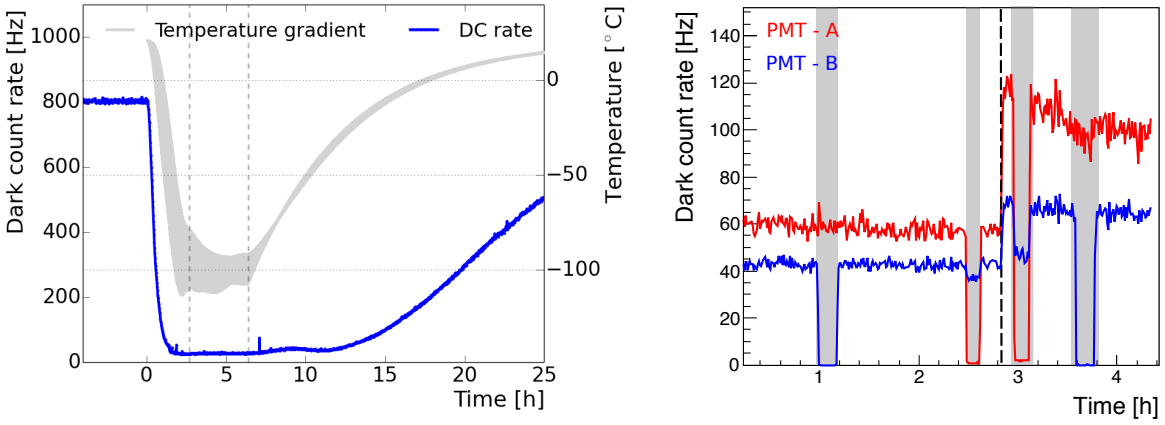

Figure 5.7: (Left) Evolution of the dark count rate for one PMT during a cooling cycle (blue curve). The gray band indicates the temperature differences between the lower PMT array (position 3 in figure 5.2) and the upper PMTs (position 6). The time interval for dedicated PMT tests is indicated by black vertical dashed lines. (Right) While the PMT operates in stable conditions, the DC rate as well as tests for micro light emission are performed by measuring changes in the average DC rates (see text). The vertical dashed lines indicates a change of the applied bias voltage of an initial 1500 V to 1680 V. Figures published in [140].

dark count rate (blue line) for one PMT during a typical cooling cycle. The temperature gradient is indicated by the gray band as measured by an upper and lower thermometer inside the cooling vessel (see figure 5.2). The strong correlation between the DC rate and temperature can be explained by the suppression of thermal electrons at cryogenic temperatures. The cooling speed does not exceed a rate of of 1.5 K/min to prevent any damage to the PMT. In general, the DC rate decreases until $\sim -20\,^{\circ}\mathrm{C}$ and a stable performance of the tubes at the target temperature of −100 °C is reached after approx. 2.5 h (vertical black dashed lines). A hysteresis of the dark count rate during the period of warming up is observed. This is explained by a higher heat capacity of the PMT as the thermometer measures the temperature of the nitrogen vapor and not the temperature of the tube itself. This procedure is performed at least twice for every PMT to expose the tubes to thermal stress. In addition to these thermal tests,

the DC rates are measured at 1500 V and 1680 V bias voltage as well as at a voltage corresponding to an equalized gain of 3×10^6.

While the PMTs operate at −100 °C they are tested for their DC rate stability, level of dark count rate as well as for instabilities such as sudden and strong light flashes or a continuous and small level of light emission. The latter is tested by turning off individual tubes while monitoring the DC rate of the PMT facing it. An example is shown in figure 5.7 (right). As two PMT windows are facing each other, light emission of the PMT under study will cause signals in the observing PMT, allowing the identification of problematic PMTs. The vertical black dashed line indicates a change of the bias voltage of 1500 V to 1680 V for PMT A (red line), resulting in an increased observed difference in the dark count rate of PMT B (blue line) (Δ=25 Hz) with respect to the lower applied HV (Δ=10 Hz). This indicates a correlation between the applied HV and the level of light emission. A more detailed analysis of the light emission of tubes is presented in section 5.3.6 and the induced effect in XENON1T in section 5.5.2. The distribution of measured DC rates for an equalized gain of 3×10^6 at room temperature and at −100 °C is shown in the left and right of figure 5.8, respectively. Again, the red (blue) distributions illustrate results for all (selected) PMTs. At room temperature

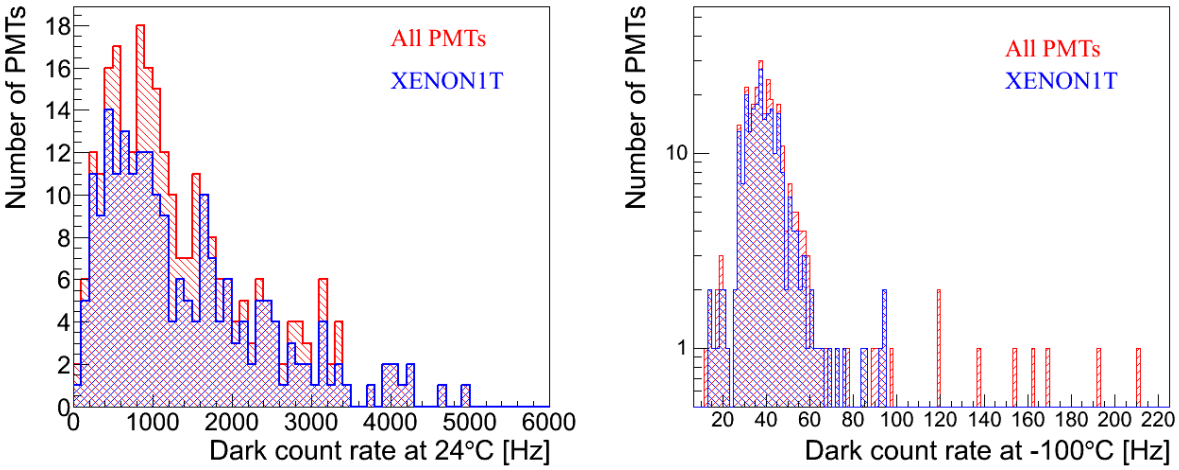

Figure 5.8: (Left) Dark count rates measured at an equalized gain of 3×10^6 at room temperature. (Right) Dark count rates at −100 °C. The red (blue) histograms indicate the data for all tested (selected) PMTs. Figures published in [140].

the average dark count rate among all PMTs (selection) is measured to be 1348 Hz (1400 Hz) with a standard deviation of 988 Hz (1025 Hz). The relatively high rates are explained by the emission of thermal electrons and can be reduced by lowering the operation temperature. Hence, at −100 °C the DC rates are reduced to 44 Hz (40 Hz) with a notably smaller standard deviation of 24 Hz (13 Hz). The tail of the red distribution to higher DC rates are PMTs which were rejected. In total 12 PMTs were rejected either due to too large DC rate or showed an unstable performance.

These results are derived for a threshold of approximately $\frac{1}{4}$ PE set at room temperature. It was measured that the gain increases at cryogenic temperatures by an

average of 10 % [140], due to an increase of the conductivity of cables, which effectively lowers the threshold to ∼0.15 PE and increases slightly the single photoelectron acceptance by ∼ 2 %. Furthermore, the distance between the two arrays correlates with the observed DC rate. A larger gap increases the solid angle of each PMT to observe Cherenkov radiation and scintillation photons (390 nm) in N_2 vapor [164] caused by ionizing radiation of for example cosmic particles and alpha particles. In this setup, the distance between two PMT windows is 2 cm. A larger gap was used for some tests and showed a factor of 2 increase in the average dark count rate measured at the same applied HV. This indicates that a significant part of the measured DC rate is not intrinsic to the PMTs and is caused by external radiation (cosmic rays, alpha particles,...). Accordingly, the expected DC rates in XENON1T should be smaller due to the strongly reduced radioactivity inside the TPC (see section 5.5).

5.3.6 PMT light emission

One of the most problematic features of this PMT version is the discovery of light emission from the tube itself. The emission and a subsequent detection of such photons is problematic, when a large number of PMTs are operated in parallel as they could randomly trigger coincident signals. As a consequence, those events would increase the background of the experiment (see section 3.4). Two different sources of light emission are identified. The first effect has a signature of a sudden *flash* which increases the DC rate and is also observed by one or many neighboring PMTs. The light emission is very large and probably causes an excitation of molecules in the quartz window which decay on time scales of minutes (see figure 5.9). The frequency of those observed flashes were

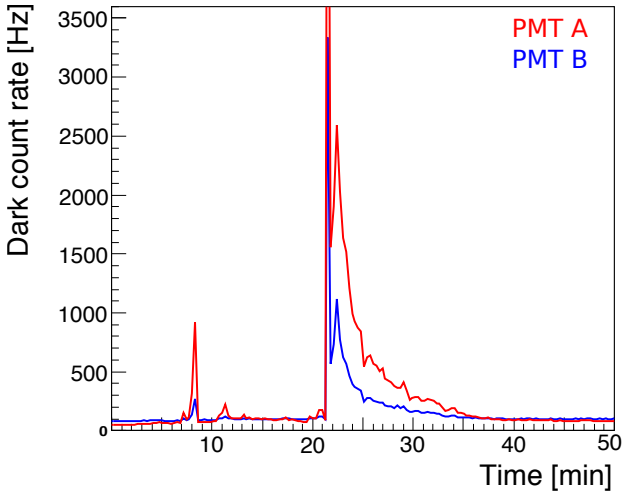

Figure 5.9: The dark count rate of PMT A increases rapidly due to a *flash* and decreases in the next minutes to its normal level. This strong light emission is also observed by the opposite PMT B.

below 1 % in all measurements, however, the presented test campaign is not suitable to

quantify those events reliably due to the relatively short operation period at cryogenic temperatures of approx. 10 to 15 h per PMT. No permanent damage is observed after a flash and, therefore, these PMTs were not replaced.

The second effect of light emission is labeled by the producer as *micro light emission* (see section 5.3.5). In this case, the light output of the tube is much smaller and continuous, hence, more subtle to detect. A detection of these emitted photons is possible by a second PMT, placed opposite of the first with the orientation of the window towards the light emitting tube. By turning the light emitting PMT off, a change of the dark count rate of the opposite PMT is observable (see figure 5.7 (right)). This allows to identify problematic tubes to a certain level of light output but with this setup it is not possible to quantify the total amount of emitted light nor the energy of the emitted photons. A visual check of these pulses on the oscilloscope shows measured sizes on the level of single photoelectrons with no specific features. To increase the sensitivity, the distance between two PMT windows is chosen as small as possible to maximize the possibility to detect photons emitted by the tube.

The difference in the dark count rate of the observing PMT is used to quantify the level of micro light emission (see right panel of figure 5.7). In the left plot of figure 5.10 the difference in the DC rate is shown with respect to the applied bias voltage to the light emitting PMT, measured in cold (blue markers) and at room temperature (red markers). The right plot correlates the effect of light emission with the temperature of

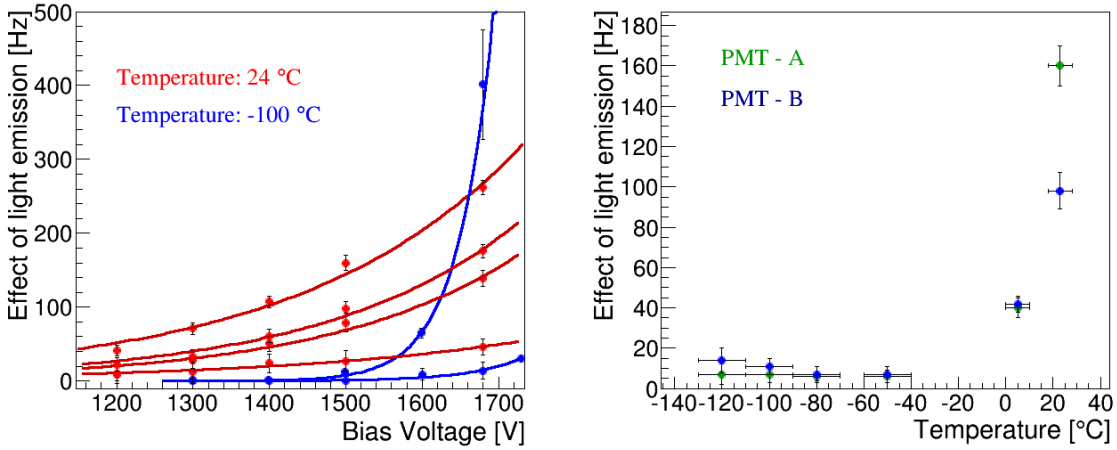

Figure 5.10: (Left) The level of micro light emission with respect to the applied bias voltage of the problematic PMT. The red markers indicate the observed effect at room temperature, whereas the blue markers show results at −100 °C. (Right) The effect of micro light emission measured at different temperatures at 1500 V. Figures published in [140].

two PMTs, showing a strong increase of the light output for higher temperatures at a constant bias voltage. The increase in temperature enhances the thermal emission of electrons and more electrons are amplified. As a consequence, the increase of the light output should correlate with the higher DC rate.

From all 73 rejected PMTs 52, (73 %) were rejected due to a severe level ($\Delta > 5$ Hz at 1680 V) of micro light emission. Triggered by the high PMT rejection rate, the producer started with counter measures to prevent light emission for future produced tubes. The origin of the light production is, according to the producer, generated at the last dynode stage and the photons exit the tube through the window. To the time of writing, 9 modified tubes were tested and, still, one PMT showed a clear signature of micro light emission. The statistics of 9 tested PMTs is small but first tests indicate an improvement, however, the problem is not yet solved. Furthermore, other studies verify the presence of light emission by this PMT model [165][166].

5.3.7 PMT leak tests

The PMTs are operated in the TPC of XENON1T in LXe and GXe for timescales of years. It is evident that even tiny leaks are extremely problematic as the loss of the vacuum inside the tube will lead to its complete damage. Therefore, dedicated tests were performed with the goal to identify leaks in PMTs by exploiting the rate of afterpulses. Residual gases in the vacuum are ionized due to strongly accelerated photoelectrons. The created ions drift to the photocathode and produce further, but delayed, secondary photoelectrons. The timing of these afterpulses is determined by the ratio of charge and mass of the ions, hence, allowing to identify various residual gases inside the tube. More details can be found in [140][156].

Afterpulse spectra are taken for all PMTs in nitrogen vapor at normal pressure and for a subset of 44 PMTs in liquid xenon. As an example the time spectrum of a measurement before (blue) and after (red) an operation in gaseous N_2 (left) and LXe (right) is shown in figure 5.11. A change of the afterpulse rate at around 1.4 μs and 2.8 μs [140] indicates a problematic PMT as shown by the increase of the nitrogen and xenon afterpulse rate, respectively. The afterpulse spectra shown in the left panel feature an exponential contribution of pulses, rising at small time delays. These events are mainly caused by secondary electrons and dark counts [140] which are not present in the right panel as they have been removed for the analysis, enabled by a more complex read out system of the DAQ [156]. The relative change of the two measurements, however, shows a clear peak caused by nitrogen afterpulses at 1.4 μs , illustrated in figure 5.12 by two vertical red dashed lines.

All PMTs were exposed to N_2 but only one PMT was identified with a leak. In contrary, of a total of 44 measured PMTs in LXe, 8 (20 %) tubes were identified with a leak. If this result is combined with the knowledge of PMT failures after one year of operation in XENON1T it becomes evident that measurements in N_2 vapor for about 15 h do not show the required sensitivity to detect these small leaks. For future tests the procedure to identify leaks must be modified by, for instance, a longer exposure of the tube to the tracer gas. On time scales of two weeks, as suggested by the UZH measurements, most problematic PMTs are identified [156]. However, the operation of tubes on time scales of weeks in LXe are not feasible for a large number of PMT tests. A solution would be to store the PMTs one to two weeks, without turning them on, in liquid nitrogen or argon. An afterpulse measurement before and after the long exposure to the tracer gas should results in a higher sensitivity to identify problematic

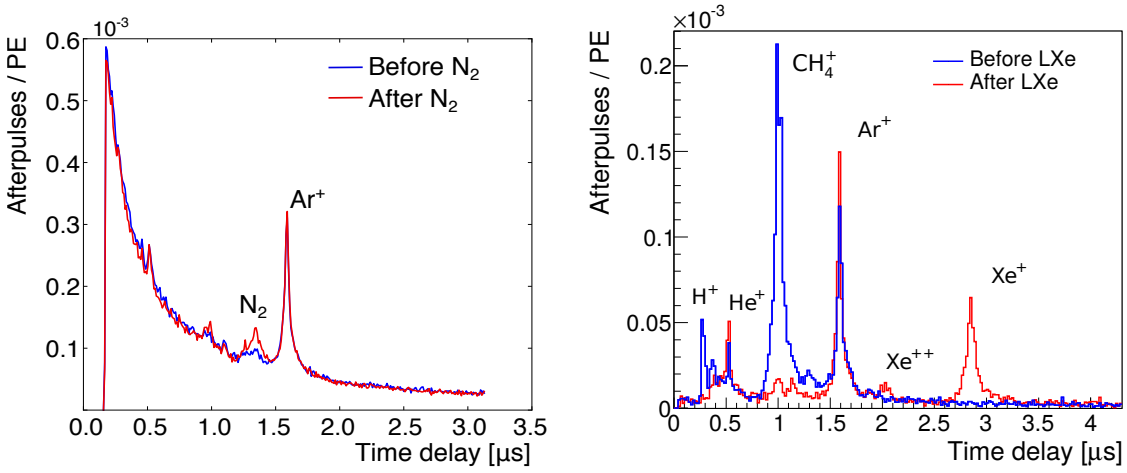

Figure 5.11: Time spectrum of afterpulses taken before (blue) and after (red) the operation in gaseous N_2 (left) and LXe (right). PMT with leaks are rejected if after the operation an increase of the nitrogen peak at 1.4 μs (left) or xenon peak at 2.8 μs (right) is observed. Right figure from [140].

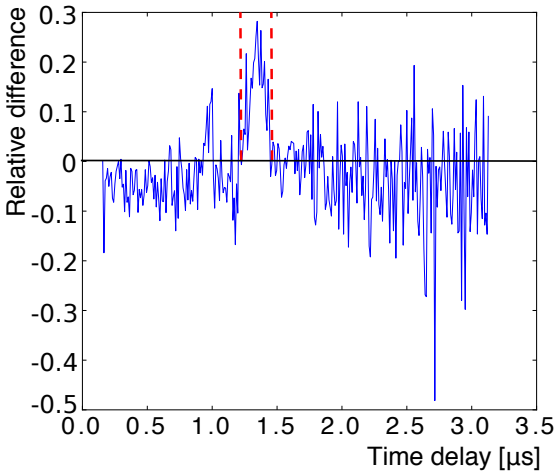

Figure 5.12: Relative change of the afterpulse spectra, taken before and after the exposure to nitrogen and two temperature cycles. The initial spectra are shown in the left panel of figure 5.11. The red dashed lines indicate the enhanced afterpulse rate due to nitrogen.

tubes.

5.4 XENON1T PMT arrays

At the end of 2015, the XENON1T TPC including the two PMTs arrays were assembled and mounted into the cryostat. A selection of 248 PMTs, based on the results above, are distributed among the top and bottom array. In the following, the array construction and installation into the XENON1T TPC is briefly summarized. Finally, first commissioning data of the PMT performance of XENON1T is presented with a focus on the effect of micro light emission.

5.4.1 PMT array assembly

The PMTs are placed inside a holding structure machined in parts of copper and Teflon. Prior to assembly the copper and Teflon are degreased and prepared for a dedicated cleaning procedure of the surfaces. This is necessary as ^{226}Ra, contained in the surface of materials, contributes to the enhancement of its daughter nuclide ^{222}Rn concentration, which is one of the main background sources of the experiment [98] (see section 2.3.1). By etching the surfaces of the used materials, ^{226}Ra and other radioactive isotopes are effectively removed [167].

The copper pieces are immersed for 5 minutes in a solution of 1 % H_2SO_4 and 3 % H_2O_2 to etch the surfaces. In a second step, the copper is passivated by immersion of the copper in a 1 % citric acid solution for further 5 minutes to prevent a recontamination. Finally, the copper is cleaned several times with deionized water and pure ethanol. The cleaning of the Teflon is more challenging as this material soaks up liquids and gases until it is saturated and is only in parts removed by increasing its temperature and exposure to vacuum. Due to the size of the Teflon arrays with diameter of 1 m, no facility to evacuate or bake was available. Hence, all pieces were only wiped in deionized water and immersed in pure ethanol to clean the Teflon of soaked in water.

After assembly of the holding structure the PMTs were placed inside the array including their bases and attached signal and HV cables. The fully equipped arrays were placed inside custom made transport boxes to be able to ship the entire structure to the site of the experiment at LNGS in Italy, with minimal risk of damage. In addition, these boxes are designed to operate each PMT in a dark environment to be able to check the functionality of the PMTs after the assembly of the arrays as well as after the transport to the experiment. The goal is to reduce risk of non operational PMTs after installation of the TPC since it is very time consuming to exchange tubes after the operation in LXe.

5.4.2 PMT-arrays

The time projection chamber of XENON1T is designed to operate two arrays of in total 248 PMTs at the top and bottom of the LXe target (see chapter 2.3.2). The bottom array is operated in LXe and shows in general a higher light collection efficiency for scintillation light than the top array due to the total reflection of photons at the liquid-gas surface (see also figure 3.1). Hence, the arrangement of PMTs in the bottom array is optimized for the scintillation light detection by maximizing the coverage.

Figure 5.13: (Left) The pictures show the assembled PMT array placed inside the open transport boxes at MPIK. (Right) PMTs are connected to their base and placed inside the array.

By arranging high QE PMTs at the center of the bottom array, as displayed by the color coded scale in figure 5.14 (right), the light collection efficiency is enhanced. The top array is optimized for the position reconstruction of interactions, achieved by an arrangement of PMTs in concentric rings as shown in figure 5.14 (left). The average QE

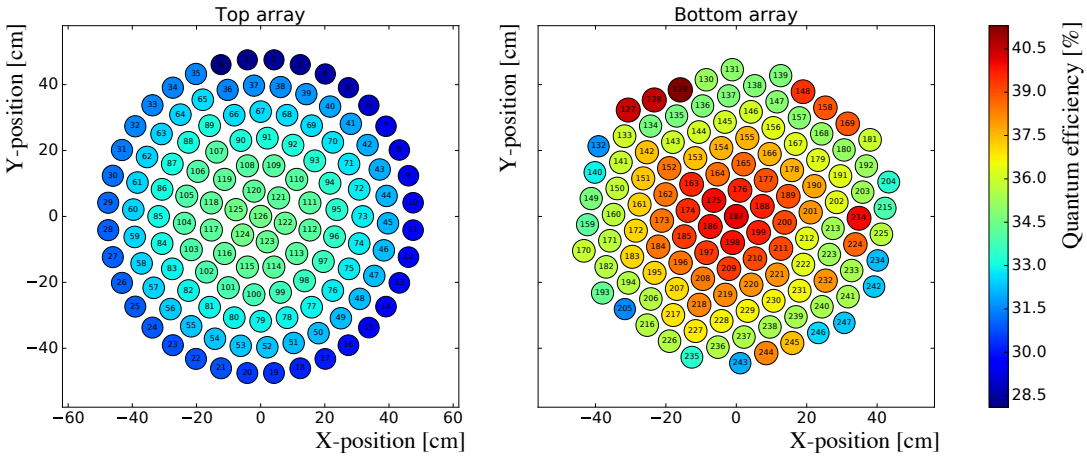

Figure 5.14: (Left) Arrangement of PMTs in the top array. Concentric rings of tubes allow a better position reconstruction of interactions in LXe. (Right) PMTs in the bottom array are arranged to maximize the light collection efficiency. In both plots, the color coded scale indicates the quantum efficiency.

of in the bottom array (36 %) is higher than in the top array (32.2 %) and is radially decreasing starting from the center.

All PMTs were screened for their radioactivity in batches up to 16 tubes. After the selection of 248 PMTs, a batch of 13 and 10 tubes showed by a factor of 2 larger radioactivity level than the average of 0.5 ± 0.1 mBq/PMT in ^{226}Ra and 11.9 ± 1.9 mBq/PMT in ^{40}K [141]. These tubes are placed at the outer rings of the arrays to maximize the distance to the fiducial volume and reduce their contribution to the background (markers in figure 5.15). PMTs with a larger ^{40}K (^{226}Ra) value are marked in green (orange). Due to a large number of rejected PMTs and following production delays, a total of

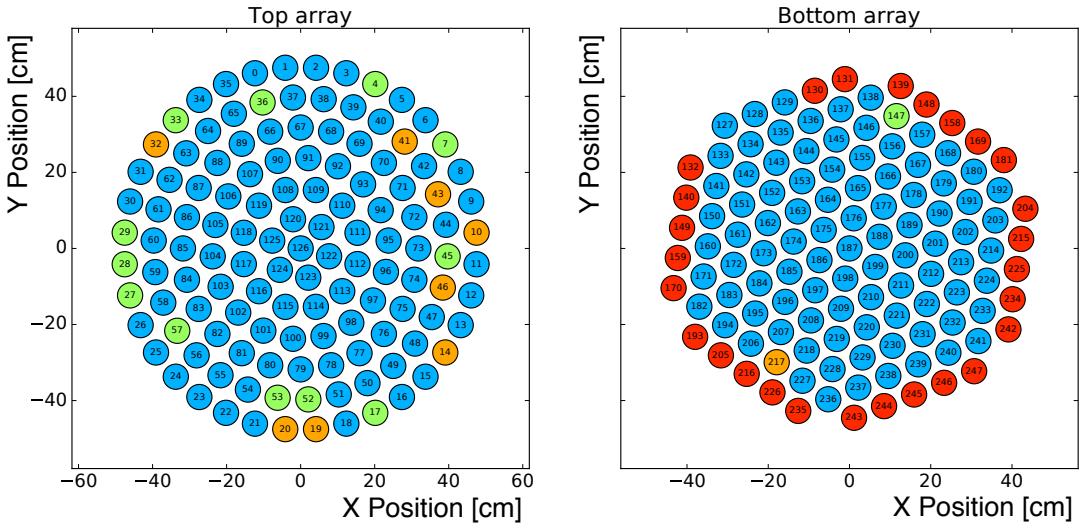

Figure 5.15: Distribution of problematic PMTs in the arrays prior to operation. PMTs marked in red show small levels of micro light emission. PMTs with a higher ^{40}K (green) and ^{226}Ra (orange) than average radioactivity level are placed at the outer rings to enlarge the distance to the fiducial volume.

27 light emitting PMTs had to be used to fully equip the arrays (marked in red). To allow for an easier accessibility of the tubes in case of an exchange, these light emitting PMTs are placed in the outer ring of the bottom array. In the first test inside the cryostat all PMTs were operational and each tube showed a signal in the scope.

5.5 PMT performance in XENON1T

An almost continuous operation of the PMTs of more than one year, inside the XENON1T TPC, allows a first analysis of their long term stability. In this section, the performance of the PMTs during the detector commissioning is discussed. Several PMTs showed problems and needed to be turned off permanently. The cause of the various effects are summarized and, in particular, a study on the influence of micro light emission is presented.

5.5.1 PMT stability

After several months of optimizing the HV of the PMTs to achieve the optimal gain for the analysis, the final gain distribution of the first science run is shown in the right of figure 5.16. The distribution has a median of 2.8×10^6. The bias voltage of the tubes is tuned to operate the PMTs at a gain of 2.5×10^6. A subset of PMTs which show an exceptional large gain are operated at higher voltages to increase the signal to noise ratio, but with a conservative maximum HV of 1550 V to protect the PMT and reduce possible light emission.

The DAQ system of XENON1T operates, in parallel to the event trigger, a software trigger which records continuously each triggered PMT pulse above $\sim$0.1 PE. If the drift and extraction field are turned off and in absence of a calibration source, the measured dark count rate is only biased by the scintillation light of LXe. The software trigger is able to distinguish signals, where no other PMT shows a coincident pulse, reducing a bias of the dark count rate measurement by physical interactions. This allows for an estimation of the DC rate of the tubes operated inside the ultra-low radioactivity environment of XENON1T. The average dark count rate for the top and bottom array of 1 h of data is shown in figure 5.16. The median of the average

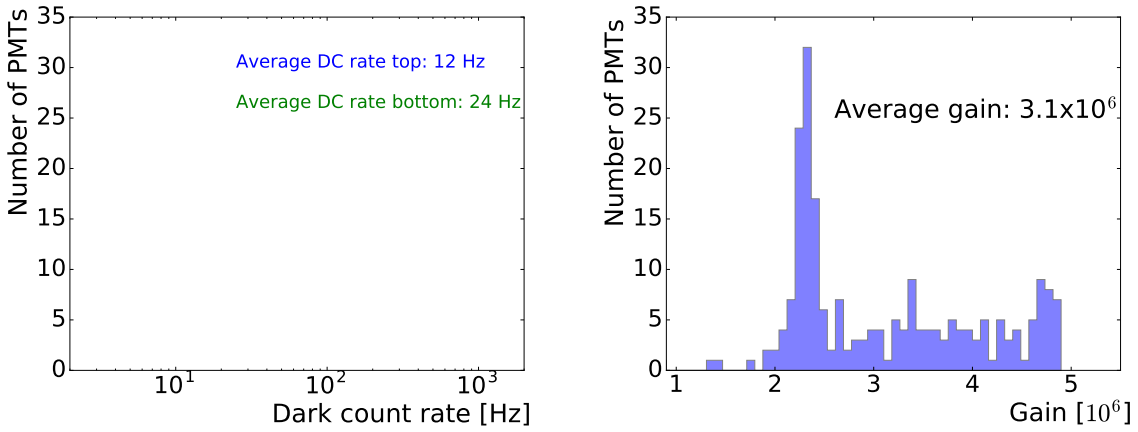

Figure 5.16: (Left) Dark count rate measurement of all PMTs for the top (blue) and bottom (green) PMT array. The median is 12 Hz (25 Hz) for the top and bottom PMTs, respectively. (Right) Gain distribution of PMTs operated in XENON1T. Most PMTs are equalized to a gain of 2.5×10^6 and a subset is operated at higher bias voltages to increase their single photoelectron acceptance.

rates is 12 Hz for the top and 25 Hz for the bottom array. Due to a total reflection of scintillation light at the liquid-gas interface, the bottom array shows a factor of 2 larger hit rate. The exceptional low DC rate of a few PMTs in the bottom array is caused by a significantly reduced HV to maintain their stability during operation. The distribution of DC rates can be compared to the average rate of 40 ± 13 Hz measured during the PMT test campaign at MPIK (section 5.3). A comparison of these values is possible due to a similar threshold during the PMT test campaign of around 0.15 PE at $-100\,^{\circ}$C

(see section 5.3.5). Hence, the differences suggest that the DC rates inside the cooling test setup at MPIK are probably biased by the cosmic radiation and higher natural radioactivity of surrounding materials and, hence, are not intrinsic to the PMTs.

During a continuous operation for over one year several PMTs showed problems that affected their operation and were turned off permanently or are operated with a lower bias voltage to reduce the emission of light. The main reason of PMT failures can be attributed to small leaks and subsequent loss of the vacuum. If the xenon concentration inside the PMT reaches a critical value, it is likely that avalanches of afterpulses force the PMT to trip. A number of PMTs show various levels of xenon afterpulses. PMTs with the highest afterpulse rates are turned off since their stability can not be maintained. In total $\sim 20\,\%$ of the tubes are affected by a leak after the exposure to xenon of one year which corresponds to the same fraction of problematic PMTs as observed at the measurements of UZH [140]. However, the xenon afterpulse rate of most PMTs is small enough for a stable operation and can be used in the analysis.

It seems that these leaks are too small to be observed by the test procedure used at MPIK. Figure 5.17 illustrates the consecutive production of tubes in terms of the PMT serial number. A production stop by the manufacturer is indicated by the gray line. The black markers show values of the measured Ar or CO_2 afterpulse rate during the MPIK test campaign. It is worth noting that by using afterpulses it is not possible to differentiate between Ar or CO_2 as they feature the same mass-to-charge ratio. The measured increase in vacuum degrading PMTs (red markers) after the fabrication stop around serial numbers 400 can be correlated with an increase in the Ar or CO_2 afterpulse rate observed after restarting production as seen in figure 5.17. This fact

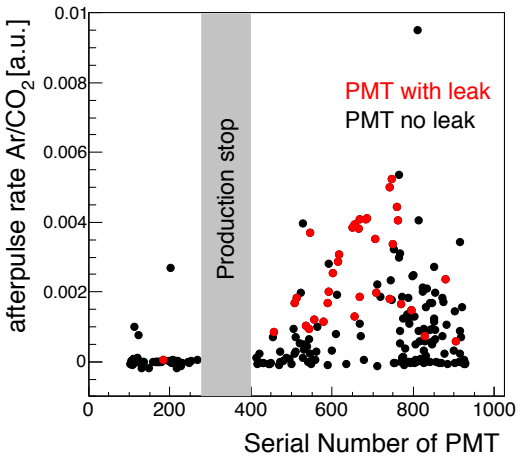

Figure 5.17: Measurement of Ar and CO_2 afterpulses from the PMT test campaign prior to the operation in xenon (black markers). In total 49 PMTs developed leaks during a one year exposure to xenon (red markers). A clear correlation between the afterpulse rate between Ar and CO_2 and xenon after the fabrication stop is observed.

suggests a change in the production procedure from the producer which lead to small

leaks in the tubes as some parts of the tube are assembled in an argon atmosphere according to Hamamatsu. It is worth noting that from 34 PMTs which were tested for approx. 2 weeks in LXe prior to their operation in XENON1T, still 4 tubes feature a measurable xenon afterpulse rate after one year.

5.5.2 Light emission in XENON1T

In section 5.3.6 the distinction of two effects of PMT light emission are described. On the one hand a sudden and large light flashes, and on the other a continuous and small micro light emission. Figure 5.18 shows a typical flash in the top panel during standard detector operation. The shape is similar as observed during the performance tests as shown by figure 5.9. The bottom panel illustrates a selection of PMTs which observe a

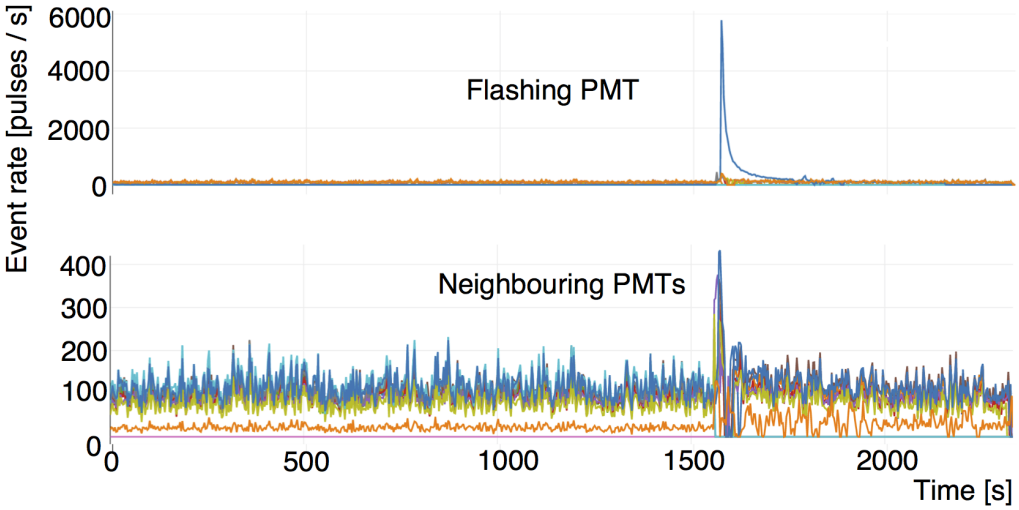

Figure 5.18: Dark count rates of several PMTs monitored over 1 h. The top panel shows a sudden flash of one PMT and the characteristic decay of its dark count rate. The bottom panel illustrates a different set of PMTs which measure the large light output from the flashing PMT. This light is observed in all PMTs of the bottom and top array but only a selection is shown here for clarity.

coincident and strong light signal. The light is seen by all PMTs regardless if placed at the top or bottom array, confirming the existence of photons emitted by the flashing PMT. As these flashes induce a large amount of light into the TPC, these time periods must be identified during a dark matter science run and removed from the analysis to avoid an enhanced background rate as indicated in the right panel of figure 3.2. Furthermore, PMTs which show frequent flashes should be turned off permanently to reduce the dead time of the TPC.

A dedicated measurement is performed to quantify the influence of the 27 tubes where a continuous emission of light at the level of $\sim 10\,\mathrm{Hz}$ at 1680 V was identified during the test campaign (see figure 5.15). The extraction field and drift field of the

TPC are turned off during the measurements to avoid the large contribution of S2s. In total 4 datasets of 1 h each are acquired starting and ending with the default configuration where the tubes are operated at their nominal HV values. To test light emission, 26 operational light emitting PMTs (1 was turned off prior to the test) in the bottom array are first turned off to avoid their light output. In another measurement, those tubes are set to a higher bias voltage (1550 V) to increase the emission of light as observed in section 5.3.6. The first indication of light emission is a change in the dark count rate (see section 5.3.6). The average dark count rate per PMT as measured by the software trigger is shown in figure 5.19 for the top and bottom array. The green

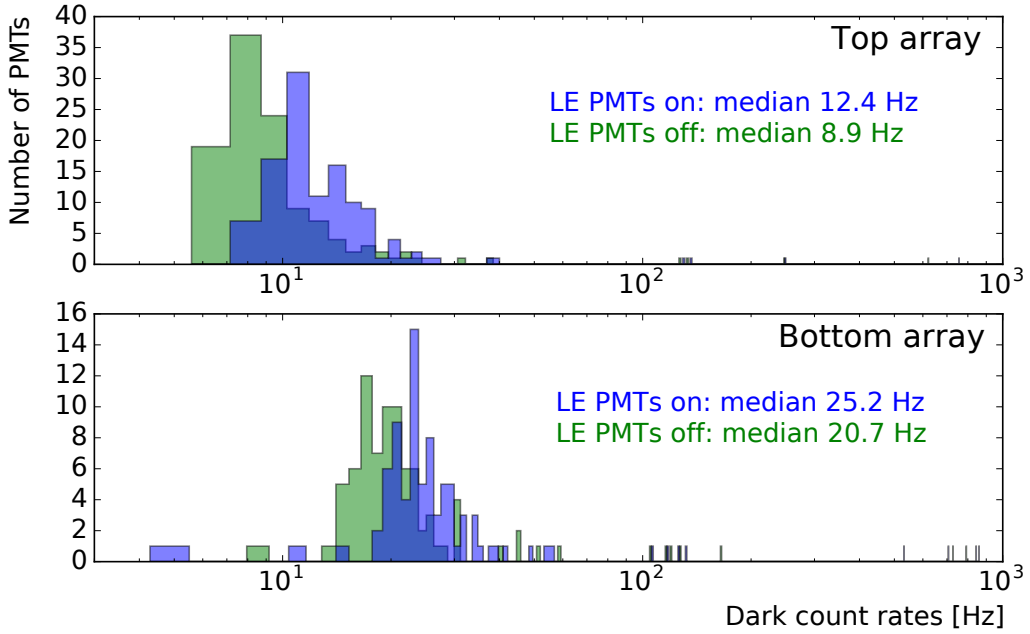

Figure 5.19: The top (bottom) plot shows the average dark count rate per channel of the top (bottom) array when all PMTs are on in blue and 26 light emitting PMTs are off in green.

histogram displays data when the problematic 26 PMTs are turned off, hence, a configuration with reduced light emission in the detector. The blue histogram shows a measurement while light emitting PMTs are turned on with a bias voltage of 1550 V. In both, the top and bottom array a reduction of the median dark count rates from 12.4 Hz to 8.0 Hz (-35 %) and 25.2 Hz to 20.7 Hz (-18 %) is observed, respectively, if light emitting PMTs are turned off. The reduction seems stronger in the top array, which is opposite to the 26 light emitting PMTs and in direct line of sight. This result, however, is derived before the data is processed and peak finding algorithms are applied to the data. It is not yet evident that this light output influences the analysis of dark matter science data, but it is likely that it influences the accidental coincidence rate.

An analysis of the processed data is shown in figure 5.20 where all recorded peaks

contained in triggered events are used. The width of all peaks as a function of the S1 area is shown. Events caused by interactions in LXe show generally a width of ~ 50 ns if the drift fields are turned off (see figure 5.21). The width is governed by the xenon

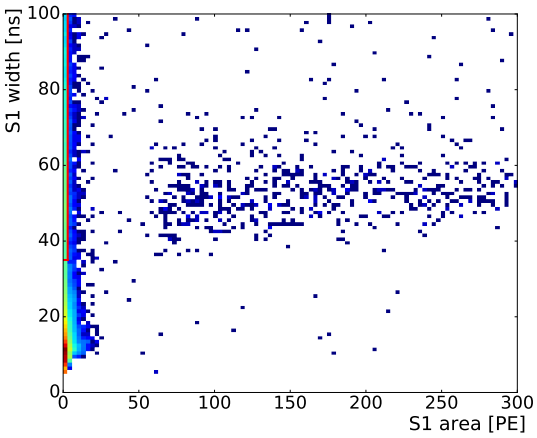

Figure 5.20: Display of all peaks contained in a waveform with respect to the peak size and width. Interactions of particles result in typical peak sizes larger than several PEs and show a width of $\sim$50 ns.

scintillation process (~ 30 ns), jitter of the PMTs (~ 9 ns) and the sampling rate of the data acquisition system (~ 10 ns). At small S1 sizes a large population is visible and a zoom into this region is shown in the left panel of figure 5.21. A selection of peaks with a width larger than 35 ns reduces most peaks triggered by noise, verified by observing several noisy peaks featuring a width smaller than 35 ns and 3 PE in size. Below a S1 size of 3 PE and a width larger than 35 ns a second population is visible which is marked by the red lines. The waveform of these peaks show good signals and are clearly not caused by noise. A selection of these peaks where the 26 light emitting PMTs are powered at nominal HV (green), increased HV (red) and turned off (blue) is shown by the histograms in the right panel of figure 5.21. The histograms display the average area in PE of each peak in a waveform for the top PMT array only. Signals in the bottom PMTs are neglected in this comparison to reduce systematic uncertainties by turning off a significant number of PMTs. A decrease of the total number of measured peaks is observed in absence of the problematic PMTs. Moreover, an increase of the applied bias voltage results in a larger population of events caused by light emission as observed in the PMT tests at MPIK (see left plot in figure 5.10). As a cross check this test was repeated by comparing two different dataset acquired this time in equal detector conditions (no PMTs were turned off) and a similar shape of the two S1 spectra are derived.

A second method possibly able to identify micro light emitting PMTs exploits the enhanced DC rate of tube which emits light. Photons produced inside the tube have to pass the photocathode to exit the tube to either enter the TPC or produce a photoelectron within the tube itself. Hence, an enhanced DC rate of micro light emitting

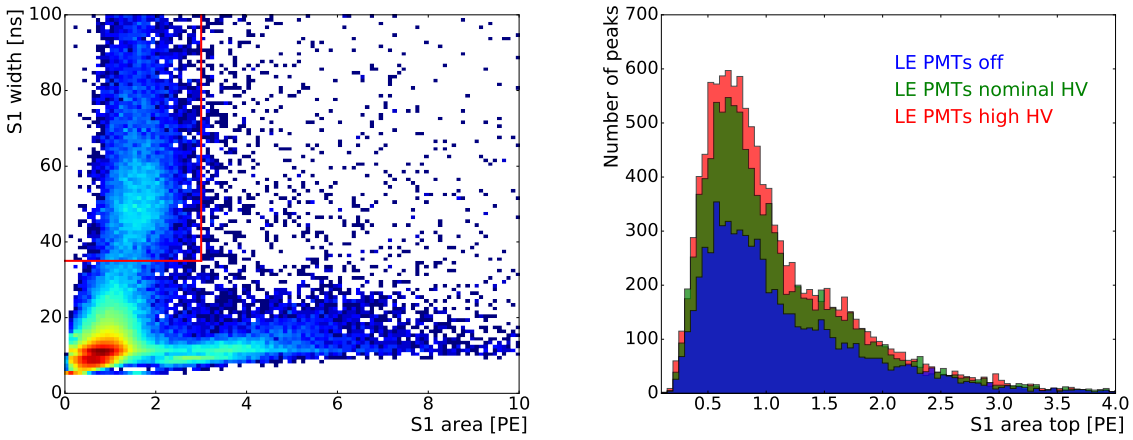

Figure 5.21: (Left) The plot shows all peaks contained in a waveform with respect to their width and size. The red box indicates a population which is affected by micro light emission. (Right) Peaks observed by the top array when the light emitting PMTs were at 1550 V (red), default high voltage (green) and off (blue).

PMTs can be expected caused by a self-detection of emitted photons, especially, if high bias voltages are applied to the known ring of problematic PMTs as shown in figure 5.15. A map of the number of hits per PMT, contributing to peaks in the region defined by figure 5.21, is shown in figure 5.22. In only one hour, a visible increase of

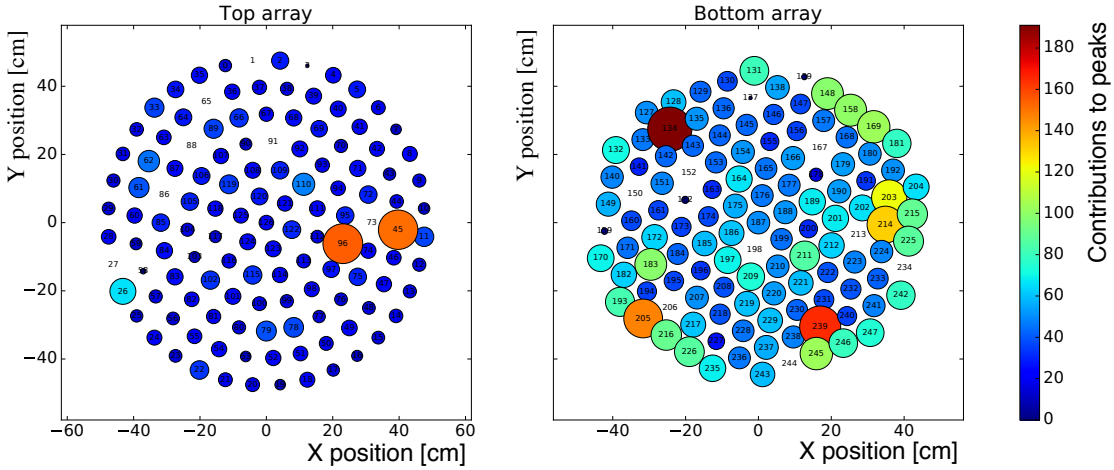

Figure 5.22: The map of the XENON1T top (left) and bottom (right) PMT arrays. The color coded scale indicates the number of contributing signals of each PMT to a peak in the micro light emission region defined in figure 5.21.

peak contributions of the outer ring of the bottom PMT array is observed. A visual

check of several waveform verify the absence of noise and, indeed, show signals at the level of single photoelectrons.

Furthermore, various other PMTs, for instance, PMT 134 and 239, show in figure 5.22 an enhanced contribution of signals to the selected peaks, indicating possible micro light emission also in these PMTs. A separate study for PMT 134 is performed to verify the method to identify problematic PMTs by an increased dark count rate caused by micro light emission at zero field. Figure 5.23 shows the dark count rate of PMT 134 taken over 1 h. A large and fluctuating DC rate of PMT 134 of several kHz

Figure 5.23: PMT 134 event rate in a dataset of 1 h taken without fields and featuring an enhanced dark count rate (top). In the next hour (bottom) the PMT is turned off (red line) after 30 min to test its impact to the data. For more information see text.

is observed while all other PMTs show rates below 50 Hz. The data in the top panel is used as a reference to analyze the impact by turning off PMT 134 in the bottom panel. Both datasets are split into equal length of 1800 s before and after switching off PMT 134 (vertical red dashed line). Again, by selecting the region of micro light emission (see figure 5.21) a difference of the S1 size distribution is observed as shown in the right panel of figure 5.24 compared to the reference data shown in the left. Both datasets are of equal length and the same selection of peaks is applied. Any measured signals of PMT 134 are neglected in the processed data due to its high rate and, hence, by turning this PMT off no difference should be visible in the data. The enhanced rate in the right plot is, therefore, caused by the emitted photons of PMT 134 which are detected by the other PMTs. To quantify the effect, residuals of the two histograms are calculated in the left panel of figure 5.25. Between 1 PE and 3 PE an enhanced rate due to micro light emission is visible, while the reference data is comparable with 0.

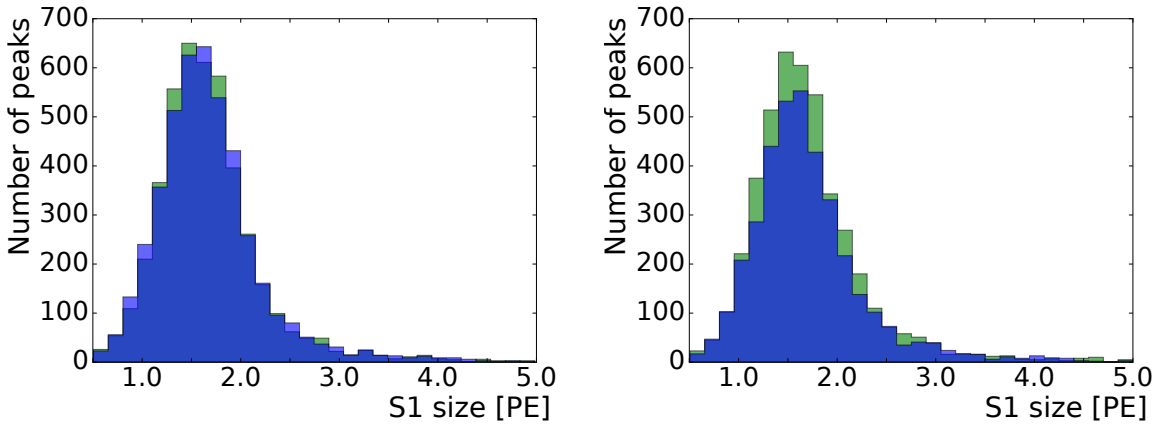

Figure 5.24: S1 spectra for the two datasets shown in figure 5.23 split in time before and after turning of PMT 134. (Left) Reference spectrum shows a constant rate in both intervals. (Right) The green histogram indicates the time interval before turning off PMT 134 and in blue after. By excluding PMT 134 from the data processor, the enhanced rate can only be explained by a detection of emitted photons from the remaining PMTs.

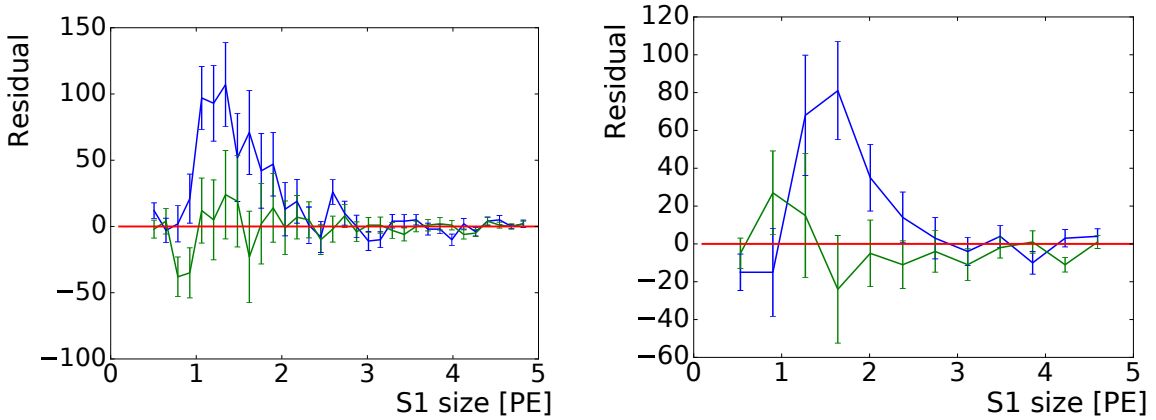

Figure 5.25: (Left) Residuals calculated from the histograms shown in figure 5.24 as a function of S1 including signals which are observed by only one PMT. The green lines show the reference datasets and in blue the dataset with the turned off PMT 134. (Right) Same dataset as in the left plot but selecting peaks with an at least twofold coincidence. For more information see text.

The data includes events where only one PMT observes a signal above the baseline. In the right panel of figure 5.25 a condition for an at least twofold coincidence level for peaks is applied. This reduces the total number of events as it is less probable that two or more photons are randomly paired. Still, a rise in the same S1 interval can be observed.

These results are derived where no fields are applied and only S1 signals are visible, as the sensitivity for micro light emission tests is reduced in presence of a large number of S2s. An analysis of data taken with fields verifies the influence of micro light emission, however, with less significance. A similar effect might have been observed in PandaX [154] where the lone S1 rate was unstable of some PMTs which possibly caused by micro light emitting PMTs.

It becomes evident that the first science run of XENON1T is affected by micro light emission and several counter measures are necessary to avoid a bias of the analysis. First of all, the energy threshold in S1 could be optimized to avoid a direct contribution of the LE population. Secondly, the PMT coincidence requirement could be increased to reduce the probability of accidental coincidences. Light emitting PMTs should be identified by the introduced method of self-detection and either be turned off or removed from the coincidence level. It might also be possible to reduce the effects of light emission by boosted-decision-trees as shown in [104]. Finally, the final background model should consider the possibly higher accidental coincidence rate as computed in section 3.4 by an estimation of the lone S1 and S2 rate.

5.6 Discussion

This chapter summaries the extensive performance test campaign for the XENON1T Hamamatsu R11410-21 PMT. In total 321 PMTs were tested at room temperature to determine their afterpulse rates, gain, peak-to-valley ratio and single photo electron ratio. In addition, all PMT are cooled at least twice to cryogenic temperatures ($-100\,^{\circ}\mathrm{C}$), not only to test their thermal stability but to probe also their dark count rate and performance stability over several hours at their final operation temperature. A third testing facility, located at University of Zurich, performed long term tests with approx. 15 % of the tubes. In general, the PMTs performed according to their specifications. The gain values are verified within 10 % and no PMTs were rejected due to an abnormal transit time spread, peak-to-valley ratio or SPE resolution.

In total 73 PMTs were returned and replaced. The main rejection reason is the detection of micro light emission of 53 tubes above 5 Hz at 1680 V. 12 PMTs were rejected due to an unstable DC rate. From the subset of 44 PMTs which were tested continuously in LXe for more than 2 weeks, 8 ($\sim 20\,\%$) were replaced as they developed a significant contribution of xenon afterpulses, indicating a leak. All PMTs were tested for leaks during the MPIK tests, however, only a few PMTs showed a significant change of the after pulse rate before and after cooling. As a consequence for future PMT tests, the leak testing must be modified to be more sensitive to these small leaks. An exposure of the PMTs to cryogenic liquids, such as LXe, LAr, LN_2, for approx. two weeks should identify most problematic PMTs. In addition, Hamamatsu started to build modified tubes with countermeasures to prevent the light output. Out of 9 tested new PMTs only one tube showed micro light emission. A statistic of 9 PMTs is small but indicates an improvement, however, the problem does not seem to be completely solved and further modifications of the tube might be necessary.

By analyzing the performance tests, 248 tubes were selected for the operation in

XENON1T. Two PMT arrays were assembled at MPIK, shipped to the experiment at LNGS in Italy and mounted to the TPC. At the time of installation of the TPC in XENON1T, all PMTs were operational and showed a signal. After a full year of operation in LXe and finalized commissioning of all detector systems an AmBe neutron calibration shows a light yield of $\sim 6.4\,\mathrm{PE}$ at 40 keV, a factor of 2.2 increase compared to XENON100. This result indicates the good performance of the PMTs. However, several tubes showed problems during operation due to a missing signal, frequent trips, unstable pulse rates or pulse rates above 1 kHz. The main cause of problems was the observation of small leaks and, at a certain afterpulse rate, their stability could not be maintained and were turned off. Furthermore, 27 PMTs, which showed a small level of micro light emission during the tests, had to be used to equip the bottom PMT array. An analysis of these 27 PMTs, including additional problematic PMTs, show that the light output has a significant impact on the data. Not only by an enhanced dark count rate of the PMT itself but the light output also induces signals at the level of single photoelectrons in other PMTs. A method to identify PMTs with a large light emission is developed which can be used in future analyses of science data to identify problematic PMTs and remove their impact, for example, by neglecting their signals in the number of coincident PMTs required for a valid S1 signal. A large contribution from events induced by the light emission is present at sizes of less than 3 PE and could be avoided by using an appropriate lower energy threshold. Finally, the background model should also take into account the lone S1 rate, which is probably enhanced by accidental coincidences originating from peaks triggered by micro light emission. By randomly pairing these lone S1s with lone S2s a dark matter like waveform could be accidentally created. This accidental coincidence background rate could be modeled as shown in section 3.4. Finally, boosted-decision-trees might be able to reduce the accidental coincidence rate as shown in [104].

Chapter 6

Summary

In the present work, the particular importance of direct detection experiments to solve the quest of dark matter is emphasized in chapter 1. Various dark matter signatures are discussed with a focus on the recoil energy spectrum of the expected WIMP interaction rate with ground-based detectors. Furthermore, it is argued that liquid xenon dual-phase TPCs are especially well suited to directly detect dark matter, explaining the superior performance of this technology in the last decade and visible in the current results of direct detection experiments (chapter 2).

The XENON100 experiment, features the longest measurement of a LXe dual-phase TPC to the time of writing, if the three major science runs are combined to a total of 477 live days and an exposure of 1.75×10^4 kg$\cdot$ day. The analysis presented in chapter 3, not only focuses on the combination of three science runs but improves also the analysis in several aspects. For the first time, the S1 energy threshold is now applied prior to its signal correction, similar as performed for the S2 threshold. This results in a more robust analysis for interactions in the upper part of the TPC, which features a low light collection efficiency, particularly important for recoil energies close the detectors energy threshold. At the same time, it exploits the high light collection efficiency in the bottom part of the fiducial volume reducing the energy threshold from the previous 6.6 $\mathrm{keV_{nr}}$ to 3 $\mathrm{keV_{nr}}$. The signal model is improved by an analytic calculation of the WIMP spectra in terms of cS1 and $\mathrm{cS2}_b$, which allows to apply all cut acceptances and thresholds directly to the corresponding parameter in cS1, S1, $\mathrm{cS2}_b$ and $\mathrm{S2}_b$. Furthermore, the extension to a two-dimensional signal model allows to define signal contours as a function of the WIMP mass, which enhances the signal to background ratio but maintains the definition of a statistical uncertainty of the background pdf. An improved background model estimates more precisely the accidental coincidence rate as a function of cS1 and $\mathrm{cS2}_b$. Finally, the likelihood function is adapted to combine three science runs, while accounting for all run-specific and run-independent nuisance parameters. As a result, an upper limit on the WIMP-nucleon spin independent cross-section at 1.1×10^{-45} cm^2 for a 50 GeV/c^2 WIMP is calculated. An improvement to the previous result by a factor of 1.8. In addition, spin dependent limits are computed with benchmark values for proton coupling at 5.2×10^{-39} cm^2 and neutron coupling at 2.0×10^{-40} cm^2 for a 50 GeV/c^2 WIMP mass.

A WIMP mass dependent banding of the signal region is used in the analysis men-

tioned above (chapter 3) to address a statistical uncertainty of the background pdf for each band based on the number of contained calibration events. This is necessary, as the background model is partly based on a parameterisation of the calibration data obtained without the knowledge of its functional form. Hence, an estimation of the background shape uncertainties of the pdf is demanding. The outlined solution in chapter 4 is twofold. An adaptive kernel density estimator is used to derive a model independent ER background pdf. The non-parametric KDE pdf is combined with a modification of the background shape term in the likelihood function. The background pdf is anticorrelated with the signal model by an additional nuisance parameter ϵ which is constrained by the background calibration dataset. It is shown that this method results in the required theoretical distributions of the test statistic in presence of a biased estimation of the background pdf or in case of limited statistics of the calibration data. The method is applied to the XENON100 science run II, with a KDE estimate of the ER background. The signal model is computed, for the first time, in terms of the minimal velocity and a parameter η which subsumes all astrophysical parameters and uncertainties. The computed constraints of the WIMP model are therefore more robust, due to an improved estimation of the background shape uncertainties in an astrophysical independent parameter space.

A further increase of the XENON100 sensitivity by longer measurements is a procedure of diminishing returns, as the background becomes at a certain duration the limiting factor. Hence, a larger detector with a reduced background is necessary. Therefore, the XENON1T experiment featuring a fiducial volume of $\sim$1 t LXe is constructed at the underground Laboratori Nazionali del Gran Sasso (LNGS) of INFN in Italy. To allow for a possible detection of WIMP recoils with the target by producing photons via scintillation and electroluminescence processes, 248 Hamamatsu R11410-21 3" PMTs are in use. An extensive testing campaign is summarized in chapter 5 which has been performed of in total 321 PMTs to verify and quantify its specified performance at room temperature and at $-100\,^{\circ}$C. The tubes performed, in general, according to their specifications, but two main rejection criteria were identified. A subset of tubes were operated in LXe over several weeks and 20 % showed a leak, while a non significant number of tubes have been identified on shorter time scales in N_2 vapor at cryogenic temperatures. In addition, a large number of 52 tubes were rejected due to a continuous emission of light. The best 248 performing PMTs were assembled in two arrays and mounted to the XENON1T TPC in Italy. However, not all light emitting PMTs could be replaced, which made it necessary to employ 27 light emitting PMTs in the bottom PMT array. After one year of operation and commissioning of the detector, the first science run has been acquired. The influence of light emitting PMTs in the acquired data is shown and these PMTs should not be employed in future experiments. In addition, various PMTs suffered a vacuum loss, instabilities or showed light emission and were turned off during the first year of operation. However, the majority of the tubes performed as expected and the average light yield at 40 keV$_{nr}$ is improved by a factor of 2.2 in comparison to XENON100. In summary, this excellent performance of the XENON detectors shows the high potential of LXe dual phase TPCs to directly detect WIMPs and larger detectors are planned for the next decade with XENONnT and DARWIN [168], which feature a high dark matter discovery potential.

Bibliography

[1] T. Marrodán Undagoitia and L. Rauch, "Dark matter direct-detection experiments," *J. Phys.* **G43** no. 1, (2016) 013001, arXiv:1509.08767.

[2] G. Bertone, ed., *Particle dark matter*. Cambridge University Press, 2010.

[3] **WMAP** Collaboration, G. Hinshaw *et al.*, "Nine-Year Wilkinson Microwave Anisotropy Probe (WMAP) Observations: Cosmological Parameter Results," *Astrophys. J. Suppl.* **208** (2013) 19, arXiv:1212.5226.

[4] **Planck** Collaboration, P. A. R. Ade *et al.*, "Planck 2013 results. I. Overview of products and scientific results," *Astron. Astrophys.* **571** (2014) A1, arXiv:1303.5062.

[5] **Planck** Collaboration, "Planck 2015 results. XIII. Cosmological parameters," arXiv:1502.01589.

[6] V. Springel, S. D. White, A. Jenkins, C. S. Frenk, N. Yoshida, *et al.*, "Simulating the joint evolution of quasars, galaxies and their large-scale distribution," *Nature* **435** (2005) 629, arXiv:astro-ph/0504097.

[7] J. o. Schaye, "The EAGLE project: simulating the evolution and assembly of galaxies and their environments," *Mon. Not. Roy. Astron. Soc.* **446** (Jan., 2015) 521, arXiv:1407.7040.

[8] M. Vogelsberger *et al.*, "Introducing the Illustris Project: Simulating the coevolution of dark and visible matter in the Universe," *Mon. Not. Roy. Astron. Soc.* **444** no. 2, (2014) 1518, arXiv:1405.2921.

[9] **2dFGRS** Collaboration, M. Colless, B. A. Peterson, C. Jackson, J. A. Peacock, S. Cole, *et al.*, "The 2dF Galaxy Redshift Survey: Final data release," arXiv:astro-ph/0306581.

[10] **BOSS** Collaboration, L. Anderson *et al.*, "The clustering of galaxies in the SDSS-III Baryon Oscillation Spectroscopic Survey: baryon acoustic oscillations in the Data Releases 10 and 11 Galaxy samples," *Mon. Not. Roy. Astron. Soc.* **441** no. 1, (2014) 24, arXiv:1312.4877.

[11] A. G. Sanchez, M. Crocce, A. Cabré, C. M. Baugh, and E. Gaztañaga, "Cosmological parameter constraints from SDSS luminous red galaxies: a new

treatment of large-scale clustering," *Mon. Not. Roy. Astron. Soc.* **400** (Dec., 2009) 1643, arXiv:0901.2570.

[12] M. Mateo, "Dwarf galaxies of the Local Group," *Ann. Rev. Astron. Astrophys.* **36** (1998) 435–506, arXiv:astro-ph/9810070.

[13] A. Pontzen and F. Governato, "Cold dark matter heats up," *Nature* **506** (2014) 171, arXiv:1402.1764.

[14] M. Bartelmann and P. Schneider, "Weak gravitational lensing," *Phys. Rept.* **340** (2001) 291, arXiv:astro-ph/9912508.

[15] L. Van Waerbeke, Y. Mellier, and H. Hoekstra, "Dealing with systematics in cosmic shear studies: New results from the VIRMOS-Descart survey," *Astron. Astrophys.* **429** (2005) 75, arXiv:astro-ph/0406468.

[16] T. Treu, "Strong Lensing by Galaxies," *Ann. Rev. Astron. Astrophys.* **48** (2010) 87–125, arXiv:1003.5567.

[17] D. Clowe, M. Bradac, A. H. Gonzalez, M. Markevitch, S. W. Randall, *et al.*, "A direct empirical proof of the existence of dark matter," *Astrophys. J.* **648** (2006) L109, arXiv:astro-ph/0608407.

[18] M. Bradac, S. W. Allen, T. Treu, H. Ebeling, R. Massey, *et al.*, "Revealing the properties of dark matter in the merging cluster MACSJ0025.4-1222," *Astrophys. J.* **687** (2008) 959, arXiv:0806.2320.

[19] W. A. Dawson, D. Wittman, M. Jee, P. Gee, J. P. Hughes, *et al.*, "Discovery of a Dissociative Galaxy Cluster Merger with Large Physical Separation," *Astrophys. J.* **747** (2012) L42, arXiv:1110.4391.

[20] D. Harvey, R. Massey, T. Kitching, A. Taylor, and E. Tittley, "The non-gravitational interactions of dark matter in colliding galaxy clusters," *Science* **347** (2015) 1462, arXiv:1503.07675.

[21] F. Kahlhoefer, K. Schmidt-Hoberg, M. T. Frandsen, and S. Sarkar, "Colliding clusters and dark matter self-interactions," *Mon. Not. Roy. Astron. Soc.* **437** no. 3, (2014) 2865, arXiv:1308.3419.

[22] F. Zwicky, "Die Rotverschiebung von extragalaktischen Nebeln," *Helvetica Physica Acta* **6** (1933) 110.

[23] V. C. Rubin, N. Thonnard, and J. Ford, W. K., "Extended rotation curves of high-luminosity spiral galaxies.," *Astrophys. J* **225** (1978) L107.

[24] E. E. Richards *et al.*, "Baryonic distributions in the dark matter halo of NGC 5005," *Mon. Not. Roy. Astron. Soc.* **449** no. 4, (2015) 3981, arXiv:1503.05981.

[25] M. Milgrom, "A Modification of the Newtonian dynamics as a possible alternative to the hidden mass hypothesis," *Astrophys. J.* **270** (1983) 365.

[26] J. D. Bekenstein, "Relativistic gravitation theory for the MOND paradigm," *Phys. Rev.* **D70** (2004) 083509, arXiv:astro-ph/0403694.

[27] M. D. Seifert, "Stability of spherically symmetric solutions in modified theories of gravity," *Phys. Rev.* **D76** (2007) 064002, arXiv:gr-qc/0703060.

[28] N. E. Mavromatos, M. Sakellariadou, and M. F. Yusaf, "Can the relativistic field theory version of modified Newtonian dynamics avoid dark matter on galactic scales?," *Phys. Rev. D* **79** no. 8, (Apr., 2009) 081301, arXiv:0901.3932.

[29] S. D. White, C. Frenk, and M. Davis, "Clustering in a Neutrino Dominated Universe," *Astrophys. J.* **274** (1983) L1.

[30] S. Tremaine and J. E. Gunn, "Dynamical role of light neutral leptons in cosmology," *Phys. Rev. Lett.* **42** (1979) 407.

[31] K. N. Abazajian *et al.*, "Light Sterile Neutrinos: A White Paper," arXiv:1204.5379.

[32] R. Adhikari *et al.*, "A White Paper on keV Sterile Neutrino Dark Matter," *JCAP* **1701** no. 01, (2017) 025, arXiv:1602.04816.

[33] G. G. Raffelt, "Astrophysical axion bounds," *Lect. Notes Phys.* **741** (2008) 51, arXiv:hep-ph/0611350.

[34] S. Weinberg, "A New Light Boson?," *Phys. Rev. Lett.* **40** (1978) 223.

[35] L. Visinelli and P. Gondolo, "Dark Matter Axions Revisited," *Phys. Rev.* **D80** (2009) 035024, arXiv:0903.4377.

[36] P. Sikivie, "Experimental Tests of the Invisible Axion," *Phys. Rev. Lett.* **51** (1983) 1415.

[37] L. Abbott and P. Sikivie, "A Cosmological Bound on the Invisible Axion," *Phys. Lett.* **B120** (1983) 133.

[38] J. L. Feng, "Dark Matter Candidates from Particle Physics and Methods of Detection," *Ann. Rev. Astron. Astrophys.* **48** (2010) 495–545, arXiv:1003.0904.

[39] G. Gelmini and P. Gondolo, "DM Production Mechanisms," arXiv:1009.3690.

[40] **CMS** Collaboration, S. Chatrchyan *et al.*, "The CMS experiment at the CERN LHC," *JINST* **3** (2008) S08004.

[41] **ATLAS** Collaboration, G. Aad *et al.*, "The ATLAS Experiment at the CERN Large Hadron Collider," *JINST* **3** (2008) S08003.

[42] **ATLAS** Collaboration, M. Aaboud *et al.*, "Search for new phenomena in final states with an energetic jet and large missing transverse momentum in pp collisions at $\sqrt{s} = 13$TeV using the ATLAS detector," *Phys. Rev.* **D94** no. 3, (2016) 032005, arXiv:1604.07773.

[43] **CMS** Collaboration, A. M. Sirunyan *et al.*, "Search for dark matter produced with an energetic jet or a hadronically decaying W or Z boson at sqrt(s) = 13 TeV," arXiv:1703.01651.

[44] L. E. Strigari, "Galactic Searches for Dark Matter," *Phys. Rept.* **531** (2013) 1, arXiv:1211.7090.

[45] J. Conrad, "Indirect Detection of WIMP Dark Matter: a compact review," in *Interplay between Particle and Astroparticle physics (IPA2014) London, United Kingdom, August 18-22, 2014*. 2014. arXiv:1411.1925.

[46] E. Bulbul *et al.*, "Detection of An Unidentified Emission Line in the Stacked X-ray spectrum of Galaxy Clusters," *Astrophys. J.* **789** (2014) 13, arXiv:1402.2301.

[47] A. Boyarsky, O. Ruchayskiy, D. Iakubovskyi, and J. Franse, "Unidentified Line in X-Ray Spectra of the Andromeda Galaxy and Perseus Galaxy Cluster," *Phys. Rev. Lett.* **113** (2014) 251301, arXiv:1402.4119.

[48] **PAMELA** Collaboration, O. Adriani *et al.*, "An anomalous positron abundance in cosmic rays with energies 1.5-100 GeV," *Nature* **458** (2009) 607, arXiv:0810.4995.

[49] **AMS** Collaboration, M. Aguilar *et al.*, "First Result from the Alpha Magnetic Spectrometer on the International Space Station: Precision Measurement of the Positron Fraction in Primary Cosmic Rays of 0.5350 GeV," *Phys. Rev. Lett.* **110** (2013) 141102.

[50] A. Ibarra, D. Tran, and C. Weniger, "Indirect Searches for Decaying Dark Matter," *Int. J. Mod. Phys.* **A28** (2013) 1330040, arXiv:1307.6434.

[51] M. W. Goodman and E. Witten, "Detectability of Certain Dark Matter Candidates," *Phys. Rev.* **D31** (1985) 3059.

[52] J. Lewin and P. Smith, "Review of mathematics, numerical factors, and corrections for dark matter experiments based on elastic nuclear recoil," *Astropart. Phys.* **6** (1996) 87.

[53] A. Drukier, K. Freese, and D. Spergel, "Detecting Cold Dark Matter Candidates," *Phys. Rev.* **D33** (1986) 3495.

[54] K. Freese, M. Lisanti, and C. Savage, "Colloquium: Annual modulation of dark matter," *Rev. Mod. Phys.* **85** (2013) 1561, arXiv:1209.3339.

[55] D. N. Spergel, "The Motion of the Earth and the Detection of Weakly interacting massive particles," *Phys. Rev.* **D37** (1988) 1353.

[56] R. H. Helm, "Inelastic and Elastic Scattering of 187-MeV Electrons from Selected Even-Even Nuclei," *Phys. Rev.* **104** (1956) 1466.

[57] L. Vietze, P. Klos, J. Menndez, W. Haxton, and A. Schwenk, "Nuclear structure aspects of spin-independent WIMP scattering off xenon," *Phys. Rev.* **D91** no. 4, (2015) 043520, arXiv:1412.6091.

[58] P. Klos, J. Menéndez, D. Gazit, and A. Schwenk, "Large-scale nuclear structure calculations for spin-dependent WIMP scattering with chiral effective field theory currents," *Phys. Rev.* **D88** (2013) 083516, arXiv:1304.7684.

[59] J. Menéndez, D. Gazit, and A. Schwenk, "Spin-dependent WIMP scattering off nuclei," *Phys. Rev.* **D86** (2012) 103511, arXiv:1208.1094.

[60] P. Belli *et al.*, "Extending the DAMA annual modulation region by inclusion of the uncertainties in the astrophysical velocities," *Phys. Rev.* **D61** (2000) 023512, arXiv:hep-ph/9903501.

[61] P. J. Fox, J. Liu, and N. Weiner, "Integrating Out Astrophysical Uncertainties," *Phys. Rev.* **D83** (2011) 103514, arXiv:1011.1915.

[62] P. J. Fox, G. D. Kribs, and T. M. P. Tait, "Interpreting Dark Matter Direct Detection Independently of the Local Velocity and Density Distribution," *Phys. Rev.* **D83** (2011) 034007, arXiv:1011.1910.

[63] C. McCabe, "The Astrophysical Uncertainties Of Dark Matter Direct Detection Experiments," *Phys. Rev.* **D82** (2010) 023530, arXiv:1005.0579.

[64] M. T. Frandsen, F. Kahlhoefer, C. McCabe, S. Sarkar, and K. Schmidt-Hoberg, "Resolving astrophysical uncertainties in dark matter direct detection," *JCAP* **1201** (2012) 024, arXiv:1111.0292.

[65] E. Del Nobile, G. B. Gelmini, P. Gondolo, and J.-H. Huh, "Update on the Halo-Independent Comparison of Direct Dark Matter Detection Data," *Phys. Procedia* **61** (2015) 45, arXiv:1405.5582.

[66] M. Blennow, J. Herrero-Garcia, T. Schwetz, and S. Vogl, "Halo-independent tests of dark matter direct detection signals: local DM density, LHC, and thermal freeze-out," arXiv:1505.05710.

[67] G. J. Feldman and R. D. Cousins, "A Unified approach to the classical statistical analysis of small signals," *Phys. Rev.* **D57** (1998) 3873, arXiv:physics/9711021.

[68] J. Conrad, "Statistical Issues in Astrophysical Searches for Particle Dark Matter," *Astropart. Phys.* **62** (2014) 165, arXiv:1407.6617.

[69] S. Yellin, "Finding an upper limit in the presence of unknown background," *Phys. Rev.* **D66** (2002) 032005, arXiv:physics/0203002.

[70] G. Cowan, K. Cranmer, E. Gross, and O. Vitells, "Asymptotic formulae for likelihood-based tests of new physics," *Eur. Phys. J.* **C71** (2011) 1554, arXiv:1007.1727.

[71] S. S. Wilks, "The large-sample distribution of the likelihood ratio for testing composite hypotheses," *Annals Math. Statist.* **9** no. 1, (1938) 60–62.

[72] **DAMA** Collaboration, R. Bernabei *et al.*, "First results from DAMA/LIBRA and the combined results with DAMA/NaI," *Eur. Phys. J.* **C56** (2008) 333, arXiv:0804.2741.

[73] **LUX** Collaboration, D. S. Akerib *et al.*, "Results from a search for dark matter in the complete LUX exposure," *Phys. Rev. Lett.* **118** no. 2, (2017) 021303, arXiv:1608.07648.

[74] **SuperCDMS** Collaboration, R. Agnese *et al.*, "WIMP-Search Results from the Second CDMSlite Run," arXiv:1509.02448.

[75] **CRESST** Collaboration, G. Angloher *et al.*, "Results on light dark matter particles with a low-threshold CRESST-II detector," arXiv:1509.01515.

[76] **PandaX-II** Collaboration, C. Fu *et al.*, "Spin-Dependent Weakly-Interacting-Massive-Particle–Nucleon Cross Section Limits from First Data of PandaX-II Experiment," *Phys. Rev. Lett.* **118** no. 7, (2017) 071301, arXiv:1611.06553.

[77] **PICO** Collaboration, C. Amole *et al.*, "Improved dark matter search results from PICO-2L Run 2," *Phys. Rev.* **D93** no. 6, (2016) 061101, arXiv:1601.03729.

[78] A. Lansiart, A. Seigneur, J.-L. Moretti, and J.-P. Morucci, "Development research on a highly luminous condensed xenon scintillator," *Nucl. Instrum. Meth.* **135** (1976) 47.

[79] O. Cheshnovsky, B. Raz, and J. Jortner, "Temperature dependence of rare gas molecular emission in the vacuum ultraviolet," *Chem. Phys. Lett.* **15** (1972) 475.

[80] E. Aprile and T. Doke, "Liquid xenon detectors for particle physics and astrophysics," *Rev. Mod. Phys.* **82** (2010) 2053, arXiv:0910.4956.

[81] J. Thomas and D. Imel, "Recombination of electron-ion pairs in liquid argon and liquid xenon," *Phys. Rev.* **A36** (1987) 614.

[82] T. Doke, H. Crawford, A. Hitachi, J. Kikuchi, P. Lindstrom, *et al.*, "Let dependence of scintillation yields in liquid argon," *Nucl.Instrum.Meth.* **A269** (1988) 291–296.

[83] J. Birks, "The theory and practice of scintillation counting," *International Series of Monographs on Electronics and Instrumentation* **27** (1964) .

[84] **XENON100** Collaboration, E. Aprile *et al.*, "The XENON100 Dark Matter Experiment," *Astropart. Phys.* **35** (2012) 573, arXiv:1107.2155.

[85] **XENON100** Collaboration, E. Aprile *et al.*, "Dark Matter Results from 225 Live Days of XENON100 Data," *Phys. Rev. Lett.* **109** (2012) 181301, arXiv:1207.5988.

[86] L. Rauch, "Detector characterization, electronic-recoil energy scale and astrophysical independent results in xenon100," Master's thesis, Max Planck Institute for Nuclear Physics, 2014.

[87] G. Plante *et al.*, "New Measurement of the Scintillation Efficiency of Low-Energy Nuclear Recoils in Liquid Xenon," *Phys. Rev.* **C84** (2011) 045805, arXiv:1104.2587.

[88] E. Aprile, C. Dahl, L. DeViveiros, R. Gaitskell, K. Giboni, *et al.*, "Simultaneous measurement of ionization and scintillation from nuclear recoils in liquid xenon as target for a dark matter experiment," *Phys. Rev. Lett.* **97** (2006) 081302, arXiv:astro-ph/0601552.

[89] **XENON100** Collaboration, E. Aprile *et al.*, "Dark Matter Results from 100 Live Days of XENON100 Data," *Phys. Rev. Lett.* **107** (2011) 131302, arXiv:1104.2549.

[90] **LUX** Collaboration, D. S. Akerib *et al.*, "Low-energy (0.7-74 keV) nuclear recoil calibration of the LUX dark matter experiment using D-D neutron scattering kinematics," arXiv:1608.05381.

[91] **XENON100** Collaboration, E. Aprile *et al.*, "Response of the XENON100 Dark Matter Detector to Nuclear Recoils," *Phys. Rev.* **D88** (2013) 012006, arXiv:1304.1427.

[92] **XENON100** Collaboration, E. Aprile *et al.*, "Observation and applications of single-electron charge signals in the XENON100 experiment," *J. Phys. G: Nucl. Part. Phys.* **41** (2014) 035201, arXiv:1311.1088.

[93] **LVD** Collaboration, M. Aglietta *et al.*, "Neutrino induced and atmospheric single muon fluxes measured over five decades of intensity by LVD at Gran Sasso Laboratory," *Astropart. Phys.* **3** (1995) 311–320.

[94] **MACRO** Collaboration, M. Ambrosio *et al.*, "Vertical muon intensity measured with MACRO at the Gran Sasso laboratory ," *Phys. Rev. D* **52** (1995) 7.

[95] **XENON100** Collaboration, E. Aprile *et al.*, "Material screening and selection for XENON100," *Astropart. Phys.* **35** (2011) 43, arXiv:1103.5831.

[96] **XENON100** Collaboration, E. Aprile *et al.*, "Study of the electromagnetic background in the XENON100 experiment," *Phys. Rev.* **D83** (2011) 082001, arXiv:1101.3866.

[97] **XENON100** Collaboration, E. Aprile *et al.*, "The neutron background of the XENON100 dark matter search experiment," *J. Phys.* **G40** (2013) 115201, arXiv:1306.2303.

[98] **XENON** Collaboration, E. Aprile *et al.*, "Physics reach of the XENON1T dark matter experiment," *JCAP* **1604** no. 04, (2016) 027, arXiv:1512.07501.

[99] **XENON1T** Collaboration, E. Aprile *et al.*, "Conceptual design and simulation of a water Cherenkov muon veto for the XENON1T experiment," *JINST* **9** (2014) 11006, arXiv:1406.2374.

[100] **XENON** Collaboration, E. Aprile *et al.*, "Online ^{222}Rn removal by cryogenic distillation in the XENON100 experiment," arXiv:1702.06942.

[101] S. Bruenner, D. Cichon, S. Lindemann, T. Marrodn Undagoitia, and H. Simgen, "Radon depletion in xenon boil-off gas," *Eur. Phys. J.* **C77** no. 3, (2017) 143, arXiv:1611.03737.

[102] **LUX** Collaboration, D. S. Akerib *et al.*, "First results from the LUX dark matter experiment at the Sanford Underground Research Facility," *Phys. Rev. Lett.* **112** (2014) 091303, arXiv:1310.8214.

[103] D. Akerib *et al.*, "Radiogenic and Muon-Induced Backgrounds in the LUX Dark Matter Detector," *Astropart. Phys.* **62** (2015) 33, arXiv:1403.1299.

[104] **PandaX-II** Collaboration, A. Tan *et al.*, "Dark Matter Results from First 98.7 Days of Data from the PandaX-II Experiment," *Phys. Rev. Lett.* **117** no. 12, (2016) 121303, arXiv:1607.07400.

[105] **XENON100** Collaboration, E. Aprile *et al.*, "Implications on Inelastic Dark Matter from 100 Live Days of XENON100 Data," *Phys. Rev.* **D84** (2011) 061101, arXiv:1104.3121.

[106] E. Aprile *et al.*, "XENON100 dark matter results from a combination of 477 live days," *Phys. Rev.* **D94** no. 12, (2016) 122001, arXiv:1609.06154.

[107] P. Grothaus, M. Lindner, and Y. Takanishi, "Naturalness of neutralino dark matter," *Journal of High Energy Physics* **7** (July, 2013) 94, arXiv:1207.4434.

[108] **LZ** Collaboration, D. S. Akerib *et al.*, "LUX-ZEPLIN (LZ) Conceptual Design Report," arXiv:1509.02910.

[109] S. Lindemann and H. Simgen, "Krypton assay in xenon at the ppq level using a gas chromatographic system combined with a mass spectrometer," *Eur. Phys. J. C* **74** no. 2, (2014) 1, arXiv:1308.4806.

[110] D. Stolzenburg, "On the krypton background in the xenon100 and xenon1t dark matter search experiments," Master's thesis, Max Planck Institute for Nuclear Physics, 2014.

[111] **XENON100** Collaboration, E. Aprile *et al.*, "Analysis of the XENON100 Dark Matter Search Data," *Astropart. Phys.* **54** (2014) 11, arXiv:1207.3458.

[112] J. Aalbers and C. Tunnell, "The pax data processor v4.0.0," July, 2016. http://dx.doi.org/10.5281/zenodo.58613.

[113] A. M. Green, "Astrophysical uncertainties on direct detection experiments," *Mod. Phys. Lett.* **A27** (2012) 1230004, arXiv:1112.0524.

[114] M. C. Smith, G. Ruchti, A. Helmi, R. Wyse, J. Fulbright, *et al.*, "The RAVE Survey: Constraining the Local Galactic Escape Speed," *Mon. Not. Roy. Astron. Soc.* **379** (2007) 755, arXiv:astro-ph/0611671.

[115] **XENON** Collaboration, A. Brown. Personal communication.

[116] **XENON100** Collaboration, E. Aprile *et al.*, "Likelihood Approach to the First Dark Matter Results from XENON100," *Phys. Rev.* **D84** (2011) 052003, arXiv:1103.0303.

[117] A. L. Read, "Modified frequentist analysis of search results (the CLs method)," in *Proceedings, First Workshop on Confidence Limits*, pp. 81–101. CERN, Geneva, Switzerland, 17 - 18 jan, 2000.

[118] **PICO** Collaboration, C. Amole *et al.*, "Dark matter search results from the PICO-60 CF_3I bubble chamber," *Phys. Rev.* **D93** no. 5, (2016) 052014, arXiv:1510.07754.

[119] **XENON100** Collaboration, E. Aprile *et al.*, "A low-mass dark matter search using ionization signals in XENON100," arXiv:1605.06262.

[120] **DarkSide** Collaboration, P. Agnes *et al.*, "Low Radioactivity Argon Dark Matter Search Results from the DarkSide-50 Experiment," arXiv:1510.00702.

[121] **XENON100** Collaboration, E. Aprile *et al.*, "Limits on spin-dependent WIMP-nucleon cross sections from 225 live days of XENON100 data," *Phys. Rev. Lett.* **111** (2013) 021301, arXiv:1301.6620.

[122] **LUX** Collaboration, D. S. Akerib *et al.*, "First spin-dependent WIMP-nucleon cross section limits from the LUX experiment," arXiv:1602.03489.

[123] **DRIFT** Collaboration, J. B. R. Battat *et al.*, "First background-free limit from a directional dark matter experiment: results from a fully fiducialised DRIFT detector," *Phys. Dark Univ.* **9** (2014) 1, arXiv:1410.7821.

[124] R. Bernabei *et al.*, "Investigating the DAMA annual modulation data in a mixed coupling framework," *Phys. Lett.* **B509** (2001) 197.

[125] **ZEPLIN-III** Collaboration, V. N. Lebedenko *et al.*, "Limits on the spin-dependent WIMP-nucleon cross-sections from the first science run of the ZEPLIN-III experiment," *Phys. Rev. Lett.* **103** (2009) 151302, arXiv:0901.4348.

[126] **CDMS** Collaboration, Z. Ahmed *et al.*, "Search for Weakly Interacting Massive Particles with the First Five-Tower Data from the Cryogenic Dark Matter Search at the Soudan Underground Laboratory," *Phys. Rev. Lett.* **102** (2009) 011301, arXiv:0802.3530.

[127] **SIMPLE** Collaboration, M. Felizardo, T. Girard, T. Morlat, A. Fernandes, A. Ramos, *et al.*, "Final Analysis and Results of the Phase II SIMPLE Dark Matter Search," *Phys. Rev. Lett.* **108** (2012) 201302, arXiv:1106.3014.

[128] N. Priel, L. Rauch, H. Landsman, A. Manfredini, and R. Budnik, "A model independent safeguard for unbinned Likelihood," arXiv:1610.02643 [physics.data-an].

[129] **CoGeNT** Collaboration, C. Aalseth *et al.*, "CoGeNT: A Search for Low-Mass Dark Matter using p-type Point Contact Germanium Detectors," *Phys. Rev.* **D88** (2013) 012002, arXiv:1208.5737.

[130] **CRESST** Collaboration, G. Angloher *et al.*, "Results from 730 kg days of the CRESST-II Dark Matter Search," *Eur. Phys. J.* **C72** (2012) 1971, arXiv:1109.0702.

[131] **CRESST-II** Collaboration, G. Angloher *et al.*, "Results on low mass WIMPs using an upgraded CRESST-II detector," *Eur. Phys. J.* **C74** (2014) 3184, arXiv:1407.3146.

[132] J. H. Davis, "The Past and Future of Light Dark Matter Direct Detection," *Int. J. Mod. Phys.* **A30** (2015) 1530038, arXiv:1506.03924.

[133] J. H. Davis, C. McCabe, and C. Boehm, "Quantifying the evidence for Dark Matter in CoGeNT data," *JCAP* **1408** (2014) 014, arXiv:1405.0495.

[134] B. W. Silverman, *Density estimation for statistics and data analysis*. London: Chapman and Hall, 1986.

[135] K. S. Cranmer, "Kernel estimation in high-energy physics," *Comput. Phys. Commun.* **136** (2001) 198–207, arXiv:hep-ex/0011057.

[136] R. Brun and F. Rademakers, "Root - an object oriented data analysis framework," in *AIHENP'96 Workshop, Lausane*, vol. 389, pp. 81–86. 1996.

[137] I. S. Abramson, "On bandwidth variation in kernel estimates-a square root law," *The Annals of Statistics* **10** no. 4, (1982) 1217–1223.

[138] **ATLAS** Collaboration, G. Aad *et al.*, "Measurement of Higgs boson production in the diphoton decay channel in pp collisions at center-of-mass energies of 7 and 8 TeV with the ATLAS detector," *Phys. Rev.* **D90** no. 11, (2014) 112015, arXiv:1408.7084.

[139] E. Del Nobile, G. B. Gelmini, P. Gondolo, and J.-H. Huh, "Update on Light WIMP Limits: LUX, lite and Light," *JCAP* **1403** (2014) 014, arXiv:1311.4247.

[140] P. Barrow *et al.*, "Qualification Tests of the R11410-21 Photomultiplier Tubes for the XENON1T Detector," arXiv:1609.01654.

[141] **XENON** Collaboration, E. Aprile *et al.*, "Lowering the radioactivity of the photomultiplier tubes for the XENON1T dark matter experiment," *Eur. Phys. J.* **C75** no. 11, (2015) 546, arXiv:1503.07698.

[142] L. Baudis *et al.*, "Gator: a low-background counting facility at the Gran Sasso Underground Laboratory," *JINST* **6** (2011) P08010, arXiv:1103.2125.

[143] D. Budjas *et al.*, "Highly Sensitive Gamma-Spectrometers of GERDA for Material Screening: Part 2," arXiv:0812.0768 [physics.ins-det].

[144] G. Heusser, M. Laubenstein, and N. Neder, "Low-level germanium gamma-ray spectrometry at the Bq/kg level and future developments towards higher sensitivity," *Proc. of Intern. Conf. Isotop. Environm* (2004) 25–29.

[145] N. Neder, G. Heusser, and M. Laubenstein, "Low level gamma-ray germanium-spectrometer to measure very low primordial radionuclide concentrations," *Appl. Rad. Isot.* **53** (2000) 191.

[146] K. Lung *et al.*, "Characterization of the Hamamatsu R11410-10 3-Inch Photomultiplier Tube for Liquid Xenon Dark Matter Direct Detection Experiments," *Nucl. Instrum. Meth.* **A696** (2012) 32, arXiv:1202.2628.

[147] L. Baudis, A. Behrens, A. Ferella, A. Kish, T. Marrodán Undagoitia, *et al.*, "Performance of the Hamamatsu R11410 Photomultiplier Tube in cryogenic Xenon Environments," *JINST* **8** (2013) P04026, arXiv:1303.0226.

[148] **PandaX** Collaboration, X. Cao *et al.*, "PandaX: A Liquid Xenon Dark Matter Experiment at CJPL," *Sci. China Phys. Mech. Astron.* **57** (2014) 1476, arXiv:1405.2882.

[149] **NEXT** Collaboration, V. Alvarez *et al.*, "NEXT-100 Technical Design Report (TDR): Executive Summary," *JINST* **7** (2012) T06001, arXiv:1202.0721.

[150] **RED** Collaboration, D. Yu. Akimov *et al.*, "Prospects for observation of neutrino-nuclear neutral current coherent scattering with two-phase Xenon emission detector," *JINST* **8** (2013) P10023, arXiv:1212.1938 [physics.ins-det].

[151] D. Yu. Akimov, A. I. Bolozdynya, Yu. V. Efremenko, V. A. Kaplin, A. G. Kovalenko, Yu. A. Melikyan, V. V. Sosnovtsev, A. V. Shakirov, and A. V. Khromov, "Noise characteristics of low-background Hamamatsu R11410-20 photomultiplier tubes," *Instrum. Exp. Tech.* **58** no. 3, (2015) 406–409.

[152] **DarkSide** Collaboration, P. Agnes *et al.*, "The Electronics and Data Acquisition System of the DarkSide Dark Matter Search," arXiv:1412.2969 [astro-ph.IM].

[153] M. Agostini *et al.*, "LArGe: active background suppression using argon scintillation for the Gerda $0\nu\beta\beta$ -experiment," *Eur. Phys. J.* **C75** no. 10, (2015) 506, arXiv:1501.05762.

[154] S. Li *et al.*, "Performance of Photosensors in the PandaX-I Experiment," *JINST* **11** no. 02, (2016) T02005, arXiv:1511.06223.

[155] C. Bauer *et al.*, "Qualification Tests of 474 Photomultiplier Tubes for the Inner Detector of the Double Chooz Experiment," *JINST* **6** (2011) P06008, arXiv:1104.0758.

[156] D. M. Paras, *Photomultiplier Tubes for the XENON1T Dark Matter Experiment and Studies on the XENON100 Electromagnetic Background.* PhD thesis, University of Zurich, 2016.

[157] L. Baudis, S. D'Amato, G. Kessler, A. Kish, and J. Wulf, "Measurements of the position-dependent photo-detection sensitivity of the Hamamatsu R11410 and R8520 photomultiplier tubes," arXiv:1509.04055.

[158] A. Lyashenko, T. Nguyen, A. Snyder, H. Wang, and K. Arisaka, "Measurement of the absolute Quantum Efficiency of Hamamatsu model R11410-10 photomultiplier tubes at low temperatures down to liquid xenon boiling point," *JINST* **9** no. 11, (2014) P11021, arXiv:1410.3890.

[159] C. H. Faham, V. M. Gehman, A. Currie, A. Dobi, P. Sorensen, and R. J. Gaitskell, "Measurements of wavelength-dependent double photoelectron emission from single photons in VUV-sensitive photomultiplier tubes," *JINST* **10** no. 09, (2015) P09010, arXiv:1506.08748.

[160] E. H. Bellamy, G. Bellettini, F. Gervelli, M. Incagli, D. Lucchesi, C. Pagliarone, F. Zetti, Yu. Budagov, I. Chirikov-Zorin, and S. Tokar, "Absolute calibration and monitoring of a spectrometric channel using a photomultiplier," *Nucl. Instrum. Meth.* **A339** (1994) 468–476.

[161] R. Saldanha, L. Grandi, Y. Guardincerri, and T. Wester, "Model Independent Approach to the Single Photoelectron Calibration of Photomultiplier Tubes," arXiv:1602.03150 [physics.ins-det].

[162] F. Kaether and C. Langbrandtner, "Transit Time and Charge Correlations of Single Photoelectron Events in R7081 PMTs," *JINST* **7** (2012) P09002, arXiv:1207.0378.

[163] Hamamatsu Photonics, *PHOTOMULTIPLIER TUBES: Basics and Applications*.

[164] G. Lehaut, S. Salvador, J. M. Fontbonne, F. R. Lecolley, J. Perronnel, and C. Vandamme, "Scintillation properties of N_2 and CF_4 and performances of a scintillating ionization chamber," *Nucl. Instrum. Meth.* **A797** (2015) 57–63.

[165] D. Yu. Akimov, A. I. Bolozdynya, Yu. V. Efremenko, V. A. Kaplin, A. V. Khromov, Yu. A. Melikyan, and V. V. Sosnovtsev, "Observation of light emission from Hamamatsu R11410-20 photomultiplier tubes," *Nucl. Instrum. Meth.* **A794** (2015) 1, arXiv:1504.07651.

[166] D. Akimov, A. Bolozdynya, Y. Efremenko, V. A. Kaplin, A. Khromov, Y. Melikyan, and V. Sosnovtsev, "Peculiarities of the Hamamatsu R11410-20 photomultiplier tubes," *PoS* **PhotoDet2015** (2016) 025.

[167] E. W. Hoppe *et al.*, "Cleaning and passivation of copper surfaces to remove surface radioactivity and prevent oxide formation," *Nuclear Instruments and Methods in Physics Research. Section A, Accelerators, Spectrometers, Detectors and Associated Equipment* **579** no. 1, (2007) 486–489.

[168] **DARWIN** Collaboration, J. Aalbers *et al.*, "DARWIN: towards the ultimate dark matter detector," *JCAP* **1611** (2016) 017, arXiv:1606.07001.

Acknowledgments

First of all, I would like to thank PD Dr. Teresa Marrodán Undagoitia for her marvelous supervision during the last years and enabling me not only to write my doctoral thesis but supporting me also in all my ideas. In addition, I am grateful for the scientific guidance and support by Prof. Dr. Manfred Lindner. Also I would like to thank Prof. Dr. Tilman Plehn who agreed to correct my thesis.

I appreciated the help of PD Dr. Teresa Marrodán Undagoitia, Steffen Hagstotz, Dr. Guillaume Eurin, Dr. Stefan Schoppmann, Dr. Daniel Mayani and Constanze Hasterok for their helpful comments to this thesis.

I would like to express my gratitude to all members of the XENON MPIK group. In particular, Dr. Hardy Simgen, Dr. Sebastian Lindemann and Dr. Guillaume Eurin for their support and friendly advise. My daily work with its endless ups and downs was humorously shared with Stefan Brünner, Constanze Hasterok, Natascha Rupp, Dominick Cichon and many more.

Also I would like to thank all people in the XENON collaboration, especially Dr. Ranny Budnik, Dr. Hagar Landsman, Dr. Alessandro Manfredini and Nadav Priel for the scientific guidance and unbelievable hospitality. I greatly enjoyed working with Dr. Daniel Mayani with his encouraging character. Finally, I would like to thank Dr. Patrick de Perio for his support, help and calming words during very stressful times.

I thank my family, girlfriend and friends for their endless support during the last years, without them I would have been lost.